APPLIED COMPUTATIONAL ELECTROMAGNETICS SOCIETY JOURNAL

July 2022
Vol. 37 No. 7
ISSN 1054-4887

The ACES Journal is abstracted in INSPEC, in Engineering Index, DTIC, Science Citation Index Expanded, the Research Alert, and to Current Contents/Engineering, Computing & Technology.

The illustrations on the front cover have been obtained from the ARC research group at the Department of Electrical Engineering, Colorado School of Mines

Published, sold and distributed by: River Publishers, Alsbjergvej 10, 9260 Gistrup, Denmark

JULY 2022 REVIEWERS

Ramin Aghajafari
Daniel Aloi
Ravi Kumar Arya
Alireza Baghai-Wadji
T. Annalakshmi Balachandar
Billel Bentouhami
Peng Chen
Thippesha D.
Osama Dardeer
Arkaprovo Das
Asmaa E. Farahat
Zi He
Poom Kumam
Anubhav Kumar
Yingsong Li
Shengyuan Luo
Valentin Mateev
Anveshkumar Nella
Alain Reineix
Kannadhasan S.
Rachid Saadane
Navneet Sharma
Mehmet Tabakcioglu
Hua Tang
Lu Wang
Wei-Chung Weng
Yinfeng Xia
Binbin Yang
Qiwei Zhan

THE APPLIED COMPUTATIONAL ELECTROMAGNETICS SOCIETY JOURNAL

Vol. 37 No. 7 July 2022

TABLE OF CONTENTS

Metamaterial Loaded Compact Multiband Monopole Antenna for Wireless Applications

Shiney Thankachan[1], Binu Paul[1], Anju Pradeep[1], Pezholil Mohanan[2], and Remsha Moolat[2]

[1]Department of Electronics and Communication Engineering, School of Engineering
Cochin University of Science and Technology, Kochi-22, Kerala, India
shineythankachan@gmail.com

[2]Department of Electronics
Cochin University of Science and Technology, Kochi-22, Kerala, India

Abstract – This paper proposes the design of a compact monopole antenna loaded with metamaterial (MTM), for multiband operation for wireless local area network (WLAN) and Worldwide Interoperability for Microwave Access (WiMAX) applications. The monopole antenna is originally designed to operate in 2.8 GHz and 6 GHz The placement of MTM yields one additional band at 3.5 GHz corresponding to WiMAX with a shift in frequency of the original monopole to the WLAN frequencies of 2.4 GHz and 5.5 GHz with improved matching at the higher band. Dependencies of resonant frequencies on various parameters are formulated through regression analysis and a design equation for the proposed antenna is developed. The full-wave simulation and design equation of the three resonances show a negligible difference. A comparative study of the developed monopole with reported antennas shows that the developed structure is compact with an overall dimension of 19 x 31 mm^2. The measured results of the antenna show good impedance bandwidth of 6.25%, 24.57%, and 16.54% for the three bands centered at 2.4, 3.5, and 5.5 GHz The antenna compactness is obtained due to metamaterial loading. All the simulated radiation characteristics of the proposed antenna are validated experimentally. The proposed antenna obtains a compact electrical size of 0.248x0.152 λ_{02} at 2.4 GHz with multi-band operations at frequencies 2.4 GHz, 3.5 GHz, and 5.5 GHz corresponding to WLAN and WiMAX**.**

Index Terms – Double negative material (DNG), metamaterial (MTM), monopole antenna, multiband antenna, WLAN, WiMAX.

I. INTRODUCTION

Multiband operation using a single antenna system is the basic need of modern wireless communication. Multiband antennas operating for wireless local area network (WLAN) and Worldwide Interoperability for Microwave Access (WiMAX) applications are one solution to the above problem. Several methods such as alteration of the ground plane, cutting slots on radiating patches, fractal antenna design, and use of metamaterial (MTM) structures have been suggested and explained for the design and development of multiband antennas [1–25] that could meet the requirements of modern wireless communication systems to a certain extent. System compactness and interference minimization can be achieved by using multiband antennas over ultra wideband antennas (UWB).

The era of multi-band operation developed through defected ground structure [1–2], providing multiple slots on radiator or ground [3–6], by the addition of metal strips [7–8], and also by adding strips and slots [9–12]. A rectangular patch antenna is made electrically small by engineering the patches of square and circular shape cuts [13]. By etching a rectangular slot in the ground plane and adding a fork-shaped strip in a modified rectangular ring, the antenna produced three resonant modes [14]. A recent development in the field is a triple-band modified Hilbert curve fractal antenna [15].

Metamaterials are artificial materials. The growing interest in the study of MTM applications in antenna development is due to the attractive properties such as negative permittivity and permeability possessed by the MTM. These properties of metamaterials help to improve the antenna performance such as miniaturization, gain, and bandwidth. Also, the use of metamaterials in multiband antenna design aids in increasing the number of operating frequencies. In antennas, metamaterials are used in different ways for obtaining multi-band operation. Single-cell MTM loading in monopole antenna results in dual-band operation for WLAN/WiMAX applications [16]. Complementary split ring resonators are loaded on a rectangular monopole antenna for producing multi-band operation [17]. Similarly, MTM cells and slots are loaded on the ground for

Submitted On: March 30, 2021
Accepted On: June 20, 2022

https://doi.org/10.13052/2022.ACES.J.370701

obtaining multiband operation in a dual-band monopole antenna [18]. Another way of using MTM for multi-band operation is etching a meandering split-ring slot on printed antennas [19]. MTM-inspired antennas are yet another method of using MTM for multi-band operation. Triple-band MTM-inspired antenna has been designed and analyzed using FDTD [20]. Compact metamaterial multiband antennas for wireless applications have been reported in [21–22]. Two novel tri-band metamaterial antennas are proposed with TER and CTER [23]. Active devices are used on metamaterials for obtaining wide-band operation [24].

All the above-mentioned antennas exhibit good multi-band performance, but they are somewhat complicated in structure. The design of a simple compact multi-band antenna operating at 2.4 GHz, 3.5 GHz, and 5.5 GHz with good radiation characteristics is the objective of this paper. The designed antenna is experimentally validated. The proposed multiband antenna overcomes the drawbacks of existing antenna designs by the combination of a monopole antenna and a double negative (DNG) metamaterial structure. This simple and compact design will provide desirable radiation characteristics in the required band as mentioned earlier.

II. MULTIBAND ANTENNA DESIGN

The evolution of the proposed antenna on FR4 substrate with a relative permittivity(ε_r) of 4.4, loss tangent of 0.02, and thickness of 1.6 mm with an overall size of 31 x 19 x 1.6 mm^3 (0.407λ_g x 0.25λ_g x 0.021λ_g; λ_g is the wavelength in the substrate at 2.4 GHz) is detailed in the following procedural steps. It is derived from a simple monopole antenna operating in two bands, with the modified ground and a DNG structure as shown in Fig. 1.

1) A simple monopole with length L_3 as $\lambda_g/2$ of the frequency 2.8 GHz is placed on one side of the substrate. The monopole is loaded with an optimized stub of dimensions 2.5 mm x 4.25 mm to improve the impedance matching.
2) A DNG structure with inner radius R_1= 6.5 mm and outer radius 6.85 mm with two stubs of length 6.3 mm is etched on the backside of the monopole. The dimensions can be optimized as explained in section 3 to excite MTM behavior.
3) The ground plane dimensions of the antenna are optimized for good matching on the chosen substrate and are shown in Table 1.

The monopole along with the defective ground is resonating at two frequencies 2.8 GHz and 6 GHz as shown in Fig. 2.

When an MTM cell is introduced into the monopole antenna, resonances are obtained at three frequencies 2.4 GHz, 3.5 GHz, and 5.5 GHz corresponding to WLAN and WiMAX applications. Since relative permittivity (ε_r) and relative permeability (μ_r) are two parameters that influence the wave propagation through a medium, alteration of these parameters changes the resonant frequencies of the antenna. On placing the MTM structure with DNG property on the monopole antenna, the substrate parameters and hence the resonant frequencies of the antenna change. The placement of MTM also produces one additional resonance and improves the S_{11} in the higher band. MTM size and position optimization are done in ANSYS® HFSS. The optimal position for an MTM unit cell is at the center of the overall geometry. When the radius of the MTM structure is

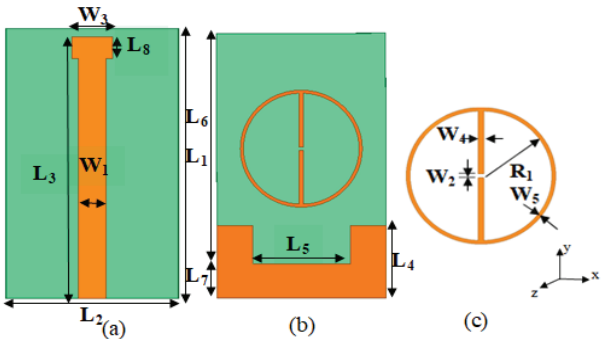

Fig. 1. The proposed Antenna (a) Front View, (b) Back View, and (c) MTM unit cell.

Table 1: Design parameters of the proposed antenna

Parameters	L_1	L_2	L_3	L_4	L_5
Size (mm)	31	19	30	8.5	11
Parameters	L_6	L_7	L_8	W_1	W_2
Size (mm)	27	4	2.5	3	0.4
Parameters	W_3	W_4	W_5	R_1	
Size (mm)	4.25	0.5	0.35	6.5	

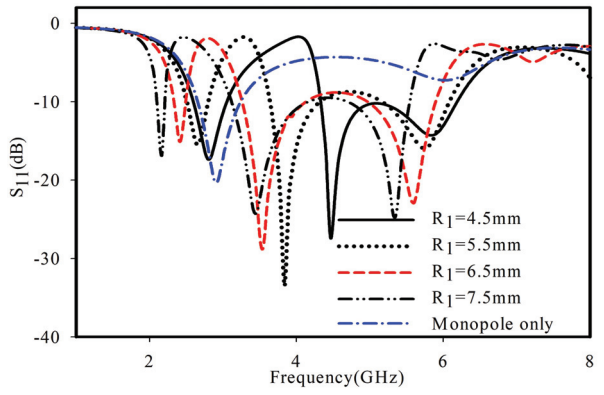

(a)

Fig. 2. *Continued.*

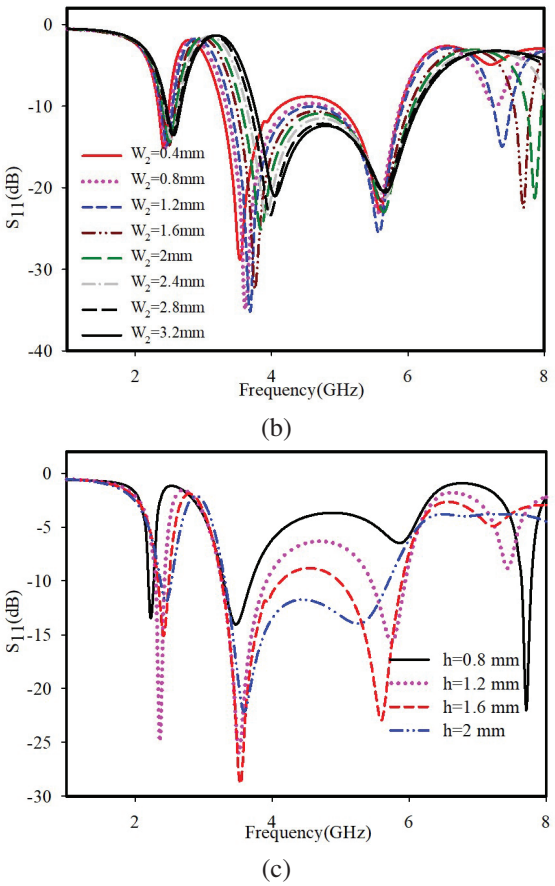

Fig. 2. Simulated S_{11} of the proposed antenna (a) variation of R1, (b) variation of W2, (c) variation of h.

altered, the antenna becomes tunable to different resonant frequencies.

The parametric analysis of the radius variation (R_1), gap (W2), and substrate thickness (h) are shown in Fig. 2. The antenna tuning over a wide range in three bands is possible through radius alterations as shown in Fig. 2 (a). Further fine-tuning of operating frequencies can be achieved by changing the gap between the stubs shown in Fig. 2 (b). Variation in substrate thickness (h) results in improved matching and bandwidth enhancement of three bands (Fig. 2 (c)).

III. MTM DESIGN

It is already stated in [26] that antenna miniaturization can be achieved by changing the relative permittivity and permeability. To lower the operating band of the chosen monopole, it is loaded with an MTM unit cell. The proposed MTM is a planar double negative material in which both permittivity and permeability are negative at 2.4 GHz and 5.5 GHz Fig. 4 shows the retrieved results of the refractive index (n) and impedance (z). The magnitude of n and z are retrieved from S_{11} and S_{21} characteristics of MTM, which are simulated using ANSYS® HFSS, and the parameters are retrieved using the s-parameter retrieval method [27–29].

To extract the S_{11} and S_{21} characteristics of MTM, a two-port waveguide configuration as shown in Fig. 3 can be used. For this boundary conditions are to be applied in such a way that the walls of the waveguide use a pair each, of both perfect magnetic conductor (PMC) and perfect electric conductor (PEC) along the planes x-y and x-z respectively. MTM structure is modeled as PEC on a dielectric slab located at the center of the waveguide.

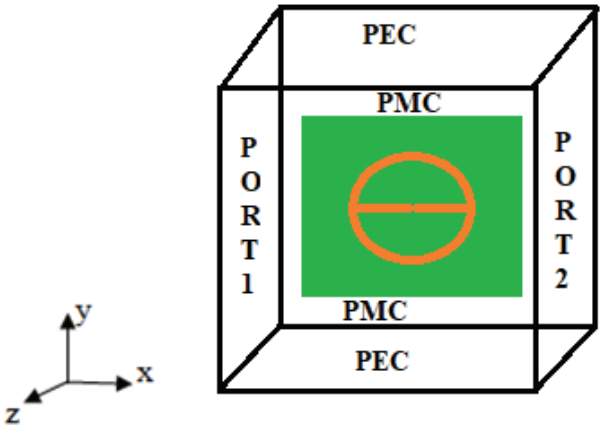

Fig. 3. MTM unit cell simulation model with boundary conditions and excitations.

Two waveguide ports are placed parallel to y-z planes. Then the input wave is launched from port1 and S_{11} and S_{21} are determined. Using these values, refractive index, impedance, permittivity, and permeability can be retrieved by S-parameter retrieval method using the following equations [29]. These equations are implemented in MATLAB™.

$$Z = \pm\sqrt{\frac{(1+S_{11})^2 - S_{21}^2}{(1-S_{11})^2 - S_{21}^2}}, \tag{1}$$

$$e^{ink_0d} = \frac{S_{21}}{1 - S_{11}\frac{Z-1}{Z+1}}, \tag{2}$$

$$n = \frac{1}{k_0 d}\left\{\left[\left[ln\left(e^{ink_0d}\right)\right]'' + 2m\pi\right] - i\left[ln\left(e^{ink_0d}\right)\right]'\right\}. \tag{3}$$

Where k_0 is the wavenumber of the incident wave in free space, m is an integer which represents branch index of refractive index. Relative permittivity ε and relative permeability μ can be calculated using the relations (4) and (5).

$$\varepsilon = n/z, \tag{4}$$

$$\mu = nz. \tag{5}$$

Figure 4 shows the extracted values of relative permittivity ε, relative permeability μ, refractive index n,

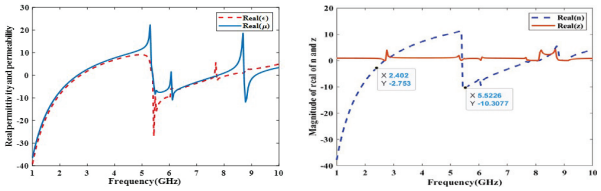

(a) (b)

Fig. 4. (a) Retrieved results for relative permittivity ε, relative permeability μ. (b) Retrieved results for refractive index n and impedance z.

and impedance z. It can be observed in Fig. 4 (a) that, at 2.4 and 5.5 GHz, both permittivity and permeability show negative values. In Fig. 4 (b) the DNG property is exhibited at desired bands of 2.4 GHz and 5.5 GHz where n is negative. A passive material shows DNG behavior when its n shows negative values and z shows positive values. This proves the designed MTM can be used for miniaturisation of antennas in these two bands.

IV. REGRESSION ANALYSIS

The data derived from the full-wave simulation of the proposed structure was subjected to regression analysis. Dependencies of resonant frequencies on various parameters are formulated through the regression analysis and they are explained as follows. The regression equations are computed using the input values for L_3 and R_1 in a millimeter scale and the resulting resonance frequency values are in GHz.

A. First resonance

The first resonance of the proposed antenna is affected by monopole length, substrate permittivity, and size of the MTM structure. Therefore the first resonance (f_{r1}) can be calculated by:

$$f_{r1} = 5.03 - 0.02L_3 - 0.11\varepsilon_r - 0.22R_1. \quad (6)$$

The regression analysis gives the variable dependencies on the first resonance through equation (6) with 98% accuracy. The design method is validated through a comparative study done on the data from full-wave simulation and those calculated using a regression equation for various values of L_3, ε_r and R_1. The resonant frequencies calculated from the design equation agree well with the simulated results. L_3, ε_r and R_1 parameters show equal correlation with the first resonance, in the correlation analysis.

B. Second resonance

The L_3, ε_r, and R_1 parameters also affect the second resonance of the proposed antenna. The second resonance (f_{r2}) can be calculated by:

$$f_{r2} = 7.59 - 0.08L_3 - 0.17\varepsilon_r - 0.13R_1. \quad (7)$$

The regression analysis gives the variable dependencies on the second resonance through equation (7) with 87% accuracy. The comparative study between simulated results and the design equation for the second resonance shows good agreement.

C. Third resonance

The third resonance (f_{r3}) can be calculated by equation (8). Variable dependencies on third resonance through equation (8) are 98% accurate. The comparative study between simulated results and the design equation for the third resonance also shows good agreement.

$$f_{r3} = 11.48 - 0.1L_3 - 0.22\varepsilon_r - 0.29R_1. \quad (8)$$

V. RESULTS AND DISCUSSIONS

As per the values proposed in Table 1, a prototype has been fabricated and tested. The photograph of the fabricated antenna is shown in Fig. 5. A comparative study of the proposed antenna with the existing antennas shows that the proposed metamaterial-loaded compact multi-band monopole antenna is more compact than the other existing schemes used for miniaturization.

The simulated and measured S_{11} are plotted in Fig. 6. The (-10) dB impedance bandwidths at three operating bands 2.4 GHz, 3.5 GHz, and 5.5 GHz are 200

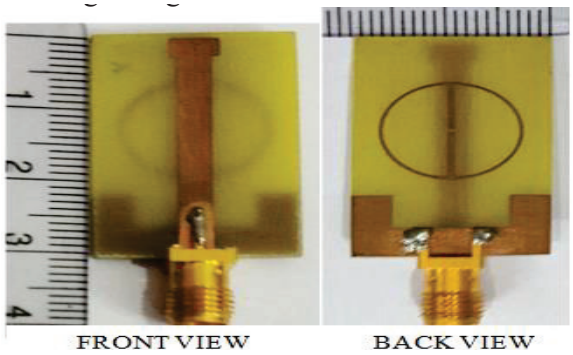

Fig. 5. Photograph of the fabricated antenna.

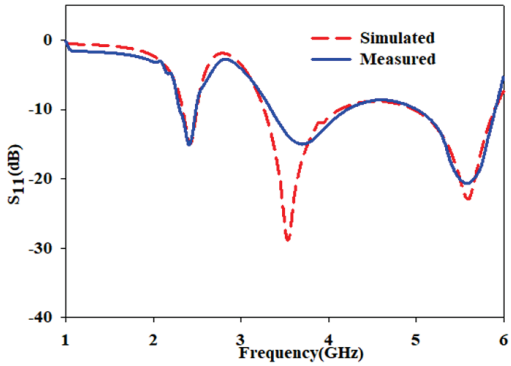

Fig. 6. Simulated and measured S_{11} of the proposed antenna.

MHz, 800 MHz, and 900 MHz respectively, which cover all the bands of WLAN and WiMAX simultaneously. The simulated and measured return loss are in good agreement.

To understand the influence of DNG structure on the monopole antenna, simulated current distribution at 2.4 GHz, 3.5 GHz, and 5.5 GHz frequencies are illustrated in Fig. 7. This illustrates that at 2.4 GHz and 5.5 GHz the monopole along with DNG jointly creates the resonance.

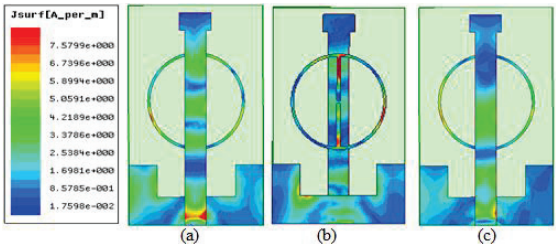

Fig. 7. Surface current distributions at (a) 2.4 GHz, (b) 3.5 GHz, and (c) 5.5 GHz.

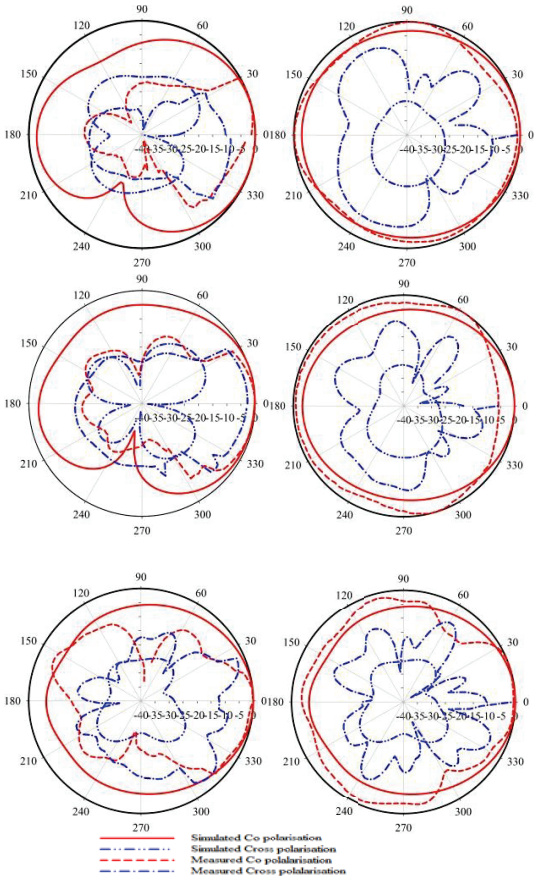

Fig. 8. Measured radiation patterns of the antenna at Y-Z and X-Z planes (a) 2.4 GHz, (b) 3.5 GHz, and (c) 5.5 GHz.

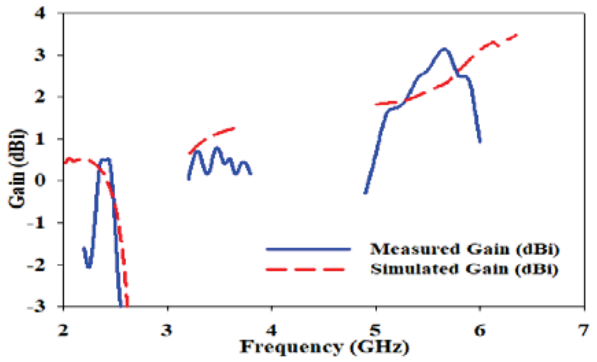

Fig. 9. Measured and simulated gain across operating bands for the proposed antenna.

At 3.5 GHz most of the current is in DNG alone, and it shows that the DNG structure generates the additional resonance.

Figure 8 shows the normalized radiation characteristics in the x-z plane and y-z plane at 2.4 GHz, 3.5 GHz, and 5.5 GHz of the proposed antenna. The proposed antenna is omnidirectional in the x-z plane and directional in the y-z plane in the desired bands; hence it can be used for portable wireless devices.

The measured and simulated gain in three wireless application bands is plotted in Fig. 9. This figure shows that all the bands have positive gain with a maximum of 3 dBi gain at 5.5 GHz A monopole antenna with a DNG structure gives improved gain characteristics than a simple monopole without DNG having comparable dimensions. This happens because the DNG eliminates substrate surface waves and the radiated energy is concentrated.

VI. CONCLUSION

An MTM-loaded compact multi-band monopole antenna for WLAN/WiMAX applications is proposed. The measured results of the antenna show good impedance bandwidth of 6.25%, 24.57%, and 16.54% for the three bands centered at 2.4, 3.5, and 5.5 GHz Measured and simulated radiation characteristics show good agreement. The proposed MTM structure is simple in design with double negative capability. The novelty of the proposed antenna is that a simple DNG structure is used and the monopole antenna loaded with the DNG results in miniaturization and an additional operating band. MTM loading enables the antenna to achieve a compact electrical size of $0.248 \times 0.152 \times 0.013\lambda_0^3$ at 2.4 GHz with improved radiation characteristics. Dependencies of resonant frequencies on various parameters are formulated. The full-wave simulation and design equation of the three resonances show a negligible difference. The proposed multiband antenna has the advantage

of compact size, easiness of fabrication, and finds applications in wireless portable devices.

REFERENCES

[1] W. C. Liu, C. M. Wu, and Y. Dai, "Design of triple frequency microstrip-fed monopole antenna using defected ground structure," *IEEE Transactions on Antennas and Propagation*, vol. 59, no. 7, pp. 2457-2463, 2011.

[2] M. Kumar and V. Nath, "Analysis of low mutual coupling compact multi-band microstrip patch antenna and its array using defected ground structure," *Eng. Sci. Technol*, vol. 19, no. 2, pp. 866-874, 2016.

[3] W. Hu, Y. Z. Yin, P. Fei, and X. Yang, "Compact triband square-slot antenna with symmetrical L-strips for WLAN/WiMAX applications," *IEEE Antennas and Wireless Propagation Letters*, vol. 10, pp. 462-465, 2011.

[4] L. Dang, Z. Y. Lei, Y. J. Xie, G. L. Ning, and J. Fan, "A compact microstrip slot triple-band antenna for WLAN/WiMAX applications," *IEEE Antennas and Wireless Propagation Letters*, vol. 9, pp. 1178-1181, 2010.

[5] A. K. Gautam, L. Kumar, B. K. Kanaujia, and K. Rambabu, "Design of compact F-shaped slot triple-band antenna for WLAN/WiMAX applications," *IEEE Transactions on Antennas and Propagation*, vol. 64, no. 3, 2016.

[6] M. Moosazadeh and S. Kharkovsky, "Compact and small planar monopole antenna with symmetrical L- and U-shaped slots for WLAN/WiMAX applications," *IEEE Antennas and Wireless Propagation Letters*, vol. 13, pp. 388-391, 2014.

[7] C. V. Anil Kumar, B. Paul, and P. Mohanan, "Compact triband dual F-shaped antenna for DCS/WiMAX/WLAN applications," *Progress in Electromagnetics Research Letters*, vol. 78, pp. 97-104, 2018.

[8] V. Deepu, K. R. Raj, M. Joseph, M. N. Suma, and P. Mohanan, Senior Member, IEEE, "Compact asymmetric coplanar strip fed monopole antenna for multiband applications," *IEEE Transactions on Antennas and Propagation*, vol. 55, no. 8, 2007.

[9] P. Surendrakumar and B. Chandra Mohan, "A triple-frequency, vertex-fed antenna for WLAN/WiMAX applications [antenna applications corner]," *IEEE Antennas and Propagation Magazine*, vol. 60, no. 3, pp. 101-106, 2018.

[10] P. Liu, Y. Zou, B. Xie, X. Liu, and B. Sun, "Compact CPW-fed tri-band printed antenna with meandering split-ring slot for wlan/wimax applications," *IEEE Antennas and Wireless Propagation Letters*, vol. 11, pp. 1242-1244, 2012.

[11] Y. Xu, Y. Jiao, and Y. Luan, "Compact CPW-fed printed monopole antenna with triple-band characteristics for WLAN/WiMAX applications," *Electronics Letters*, vol. 48, no. 24, pp. 1519-1520, 2012.

[12] R. Mishra, R. Dandotiya, A. Kapoor, and P. Kumar, "Compact high gain multiband antenna based on split ring resonator and inverted f slots for 5g industry applications," *Applied Computational Electromagnetics (ACES) Journal,* vol. 36, no. 8, 2021.

[13] L. Peng, C. Ruan, and X. Wu, "Design and operation of dual/triple-band asymmetric M-shaped microstrip patch antennas," *IEEE Antennas and Wireless Propagation Letters*, vol. 9, pp. 1069-1072, 2010.

[14] X. Teng, X. Zhang, Y. Li, Z. Yang, D. Liu, and Q. Dai, "A compact triple-band printed monopole antenna for WLAN/WiMAX applications," *ISAPE2012*, Xian, pp. 140-143, 2012.

[15] A. Kumar and A. P. S. Pharwaha, "Triple band fractal antenna for radio navigation and fixed satellite services using dragonfly optimization," *Adv. Electromagnetics*, vol. 8, pp. 43-49, 2019.

[16] H. Huang, Y. Liu, S. Zhang, and S. Gong, "Multiband metamaterial loaded monopole antenna for WLAN/WiMAX applications," *IEEE Antennas and Wireless Propagation Letters*, vol. 14, pp. 662-665, 2015.

[17] R. S. Daniel, R. Pandeeswari, and S. Raghavan, "A compact metamaterial loaded monopole antenna with offset-fed microstrip line for wireless applications," *International Journal of Electronics and Communications,* vol. 83, pp. 88-94, 2017.

[18] T. Ali, M. M. Khaleeq, S. Pathan, and R. C. Biradar, "A multiband antenna loaded with metamaterial and slots for GPS/WLAN/WiMAX applications." *Microwave Optical Technology Letters*, vol. 60, pp. 79-85, 2017.

[19] P. Liu, Y. Zou, B. Xie, X. Liu, and B. Sun, "Compact CPW-fed tri-band printed antenna with meandering split-ring slot for WLAN/WiMAX applications," *IEEE Antennas and Wireless Propagation Letters*, vol. 11, pp. 1242-1245, 2012.

[20] S. K. Sharma, J. D. Mulchandani, D. Gupta, and R. K. Chaudhary, "Triple band metamaterial-inspired antenna using FDTD technique for WLAN/WiMAX applications," *Int J RF Microw Comput Aided Eng.*, vol. 25, pp. 668-695, 2015.

[21] R. Rajkumar and K. A. Usha Kiran, "Compact metamaterial multiband antenna for WLAN/WiMAX/ITU band applications," *International Journal of Electronics and Communications*, vol. 70, no. 5, pp. 599-604, 2016.

[22] A. W. Mohammad and T. A. Ali, "Compact coaxial fed metamaterial antenna for wireless applications," *Journal of Instrumentation*, vol. 14, 2019.

[23] C. Zhu, T. Li, K. Li, Z.-J. Su, X. Wang, H.-Q. Zhai, L. Li, and C.-H. Liang, "Electrically small metamaterial-inspired tri-band antenna with meta-mode," *IEEE Antennas and Wireless Propagation Letters*, vol. 14, pp. 1738-1741, 2015.

[24] R. Salhi, M. Abidi, and F. Choubani, "A wide band microstrip antenna based on active circular SRRs," *ICWITS / ACES,* 2016.

[25] G. Dai, X. Xu, and X. Deng, "Size-reduced equilateral triangular metamaterial patch antenna designed for mobile communications," *Applied Computational Electromagnetics Society (ACES) Journal*, vol. 36, no. 8, pp. 1026-1030, 2021.

[26] C. A. Balanis, *Antenna Theory Analysis and Design*, 3rd ed., John Wiley & Sons, USA, 2005.

[27] X. Chen, T. M. Grzegorczyk, B. Wu, J. Pacheco, Jr., and J. A. Kong, "Robust method to retrieve the constitutive effective parameters of metamaterials," *Physics Review E*, vol. 70, 2004.

[28] A. B. Numan and M. S. Sharawi, "Extraction of material parameters for metamaterials using a full-wave simulator," *IEEE Antennas and Propagation Magazine*, vol. 55, pp. 202-211, 2013.

[29] S. Thankachan, B. Paul, A. Pradeep, and R. Moolat, "Design and characterisation of simple planar metamaterial structure with double negative properties," *TENCON 2019*, pp. 1231-1235, 2019.

Shiney Thankachan was born in Kerala, India in 1979. She received her B-Tech and M-Tech degrees from Cochin University of Science and Technology, Cochin, India in 2001 and 2010 respectively. She is currently a research scholar at the School of Engineering, CUSAT, Cochin. Her interests include Metamaterials, Planar antennas, and computational electromagnetics.

Binu Paul was born in Kerala, India in 1971. She received her M-Tech and Ph.D. degrees from Cochin University of Science and Technology, Cochin, India in 1996 and 2006 respectively. She is currently an Associate Professor at the School of Engineering, CUSAT, Cochin. Her research interests include planar antennas, computational electromagnetics, and compact planar filters. She is a member of IEEE Antennas & Propagation Society and IEEE-WIE.

Anju Pradeep was born in Kerala, India in 1972. She received her M-Tech and Ph.D. degrees from Cochin University of Science and Technology, Cochin, India in 2008 and 2015 respectively. She is currently a Professor at the School of Engineering, CUSAT, Cochin. Her research interests include metamaterials and optimization techniques for electromagnetics. She is a member of IEEE Antennas & Propagation Society and IEEE-WIE.

Pezholil Mohanan was born in India on May 30th, 1956. He received his Ph.D. degree in Microwave antennas from Cochin University of Science & Technology in 1985. From 1980 until 1986, he worked as a Lecturer in Physics at St. Albert's College, Cochin. He spent two years in Bharat Electronics (BEL), Ghaziabad as an Engineer in Antenna R&D Laboratory. Since 1989, he has been working as a faculty of the Department of Electronics, CUSAT, and is presently working as a Professor in the department. His current areas of research activities are microstrip antennas, fdtd analysis, dielectric resonator antennas, superconducting microwave antennas, leaky wave antennas, reduction of radar cross section, and microwave instrumentation, among others. He is a member of IEEE Antennas & Propagation Society and IEEE Microwave & Theory and Techniques Society.

Remsha M received an M.Sc degree in Electronics Science from Cochin University of Science and Technology, Cochin, India, in 2013 and is currently working toward a Ph.D. degree in Microwave Engineering at Cochin University of Science and Technology. Her main research interests include microwave sensors for material characterization, microwave measurement techniques, Stepped Impedance resonators, Antennas, and Substrate integrated waveguides.

Super Ultra-Wideband Planar Antenna with Parasitic Notch and Frequency Selective Surface for Gain Enhancement

Pankaj Jha[1], Anubhav Kumar[1], Asok De[2], and Rakesh Kumar Jain[1]

[1]Department of Electronics and Communication Engineering
Shobhit Institute of Engineering and Technology (Deemed to be University), Meerut 250110, India

[2]Department of Electronics and Communication Engineering
Delhi Technological University (DTU), New Delhi 110042, India
pankaj.maahi@gmail.com; asok.de@gmail.com

***Abstract* –** A compact Super ultra-wideband (SUW) antenna is discussed in this work. A rectangular radiator is modified into a tree-shaped structure with the defected partial ground to enhance the operating bandwidth. The novel rectangular parasitic with the circular slot is used as a notch in the ground plane which prevents the WLAN frequency. The proposed SUW antenna is achieving the 10 dB impedance bandwidth (IBW) from 3.5 GHz to 66.5 GHz frequency with a notched band varying from 5.0 GHz to 5.4 GHz. The bandwidth ratio (BDR) of the proposed SUW antenna is 1773.4 whereas the obtained bandwidth percentage (BW %) is 180. A modified SRR frequency selective surface (FSS) is designed for UWB application to improve the gain of the antenna. The compact unit cell of FSS is having electrical dimensions of $0.16\lambda_0 \times 0.16\lambda_0$. The antenna achieves the maximum realized gain 9.46 dB when FSS is loaded as a superstrate and up to 5.2 dB gain enhancement is observed in the UWB frequency.

***Index Terms* –** SUW, BDR, FSS, gain enhancement, notch band.

I. INTRODUCTION

The present scenario of wireless communication demands a compact antenna design with improved data rate, large capacity and secure communication. The standard bandwidth of UWB communication is varying from 3.1 GHz to 10.6 GHz, it is preferred in short range applications [1]. To enhance the functionality of the communication system, the SUW antenna can be a better design option for long-range, short-range and many wireless applications. Further due to the large bandwidth (at least 10:1 bandwidth ratio [2]) of antenna it provides high channel capacity with higher data rate which can be advantageous for ISM band, GPS, GSM, and WLAN, defense, satellite communication, aeronautical navigation and radio astronomy [3]. Researchers proposed different structures and technologies for SUW antenna and they focused upon compactness, bandwidth % and BDR of the antenna. In [2], a monopole SUW antenna having 10 dB IBW from 2.59 – 31.14 GHz was designed in which a rectangular stub is accomplished for the improvement of impedance matching. In [3], three elliptical structures are used to design a tree-shaped radiator to obtained SUW characteristics from 0.65 – 35.61 GHz frequency. Sierpinski-shaped [4], the octagonal fractal antenna [5] with defects in the ground is used to design a SUW antenna with 1414.5 and 3015 BDR value respectively. In [6], an elliptical monopole SUW antenna is designed where a tapered feed is used for bandwidth improvement. In [7], CPW fed, Propeller-shaped radiator is designed to obtain the SUW characteristics from 3.15–32 GHz frequency. In [8], a transparent antenna is designed for SUW application obtaining BW % of 191. In [9], a gap is created between the ground plane and radiator to achieve SUW characteristics from 2.5–110 GHz frequency.

The gain of the antenna is an essential requirement in wireless communication and the EM signals can be transmitted as well as received effectively with a high gain antenna therefore to fulfil this many gain enhancement technologies are presented in the literature in which AMC [10–12], Metamaterial [13–15] and FSS [16–21] are the major techniques introduced by researchers. The Metamaterial techniques depends upon the characteristics of permittivity and permeability for the gain enhancement whereas the AMC and FSS control the grating lobes introduced by the antenna, reflect the radiations in a specific direction and increase the overall gain of the antenna. In [10], AMC technology is used in multi-band antenna where gain enhancement depends upon the reflection phase angle. In [11], rectangular loop fractal AMC is positioned parallel to the ground plane in a wideband antenna for gain enhancement. In [12], modified circular loop AMC loaded on the CPW antenna

Submitted On: January 28, 2022
Accepted On: July 13, 2022

https://doi.org/10.13052/2022.ACES.J.370702

where it is working as a reflector. In [13], the dielectric superstrate is used the gain improvement and the radius of slots in the superstrate altered the effective permittivity. In [14], a metamaterial unit cell in the ground plane placed diagonally enhances the gain of a dual-band antenna. In [15], two hexagonal metamaterial cells are placed behind the antenna having double Negative metamaterial (DNG) property increases the antenna gain. In [16], a single layer FSS with the modification in loop structure is designed for the antenna operating in sub-6 GHz frequency. In [17], an FSS is designed using four asymmetric rectangular conducting elements with circular slots in one unit cell for the UWB antenna. In [18], a dual-layer FSS is designed for ISM band gain enhancement. In [19], two-layer FSS is developed accomplished with an air gap between the arrays for umbrella-shaped antenna where the UWB antenna achieved up to 4 dB gain enhancement with the FSS arrangement. In [20], FSS is accomplished with four interconnected square loop metallic paths demonstrating the stopband characteristics in the entire operating band. In [21], two layers of thin FSS are designed accomplished with cross-shape and circular-shape design in the top and bottom layer.

According to the literature analysis, the SUW antenna and FSS are designed in the proposed work with the following technical contributions and novelties.

(i) The proposed antenna is designed with a simple structure and compact electric length of $0.29\lambda_0 \times 0.35\lambda_0$ where λ_0 is a wavelength of the lowest operating frequency. A very high value of BDR (1773.4) validates the compactness of discussed antenna.
(ii) A parasitic rectangular stub with a circular slot demonstrates stopband characteristics and a novel WLAN notch is achieved due to formation of parallel LC circuit.
(iii) A modified SRR structure is used to design the compact FSS unit cell with the electric dimension of $0.16\lambda_0 \times 0.16\lambda_0$ and the stopband characteristics associated in FSS superstrate are diminished from the antenna notch band.
(iv) FSS superstrate significantly enhances the realized gain up of antenna up to 5.22 dB in the UWB frequency range.

II. ANTENNA DESIGN AND EVOLUTION

The SUW antenna and FSS is designed with FR4 substrate having dielectric constant (ε_r) 4.4 and 1.6 mm substrate thickness. The proposed SUW antenna design is depicted in Figs. 1 (a) and (b), and hardware is illustrated in Fig. 1 (c). The antenna acquires a physical space of 25 (U1) × 30 (U2) mm2. The SUW antenna is ensuring the dimensions details as follows, P1 = 9.5 mm, U3 = 8.5 mm, G1 = 7.1 mm, P2 = 9 mm, G2 = 11 mm, U4 = 3 mm, P3 = 5.5 mm, G3 = 11 mm, U5 = 5.5 mm, G5 = 3 mm, P4 = 5.5 mm, U6 = 5.5 mm, G6 = 2 mm, P5 = 9 mm, G4 = 4 mm, G7 = 4 mm, G8 = 3.1 mm, R = 2.75 mm and U7 = 7.5 mm.

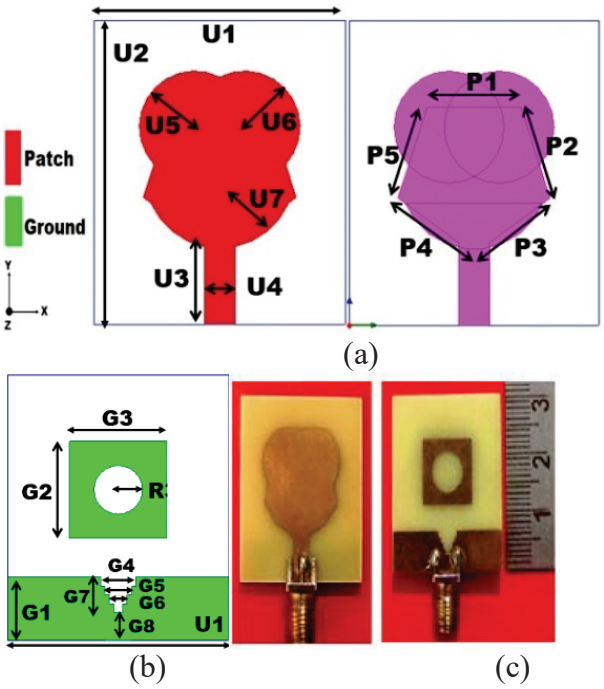

Fig. 1. (a) Dimensions of top plane. (b) Dimensions of bottom plane. (c) Prototype hardware of SUW antenna.

The proposed SUW antenna with parasitic stub is developed in five successive steps as depicted in Fig. 2. In step 1, a rectangular radiating patch is designed using eqn (1) [22] given below.

$$W_P = \frac{c}{2f}\sqrt{\frac{2}{\varepsilon_r+1}}, \quad (1)$$

where W_P is the patch width of the antenna, c represents light velocity and f is the minimum operating frequency. Using above equation the obtained width of patch is 25 mm for 3.5 GHz frequency validating the antenna dimensions.

To obtain and validate 50 Ω impedance matching of proposed work eqn (2) [22] is utilized as given below.

$$Z_0 = \frac{120\pi}{\sqrt{\varepsilon_{re}}\left[\frac{W_p}{h}+1.393+0.667\ln\left(\frac{W_p}{h}+1.444\right)\right]}, \quad (2)$$

where W_P and h is the dimension of proposed antenna and ε_{re} is effective permittivity.

Further the micro-strip feed is designed with a 3 mm width and 7.5 mm length where partial groundconductor height is 7 mm. The feed is also matched with 50 Ω impedance matching. The rectangular-shaped radiator's

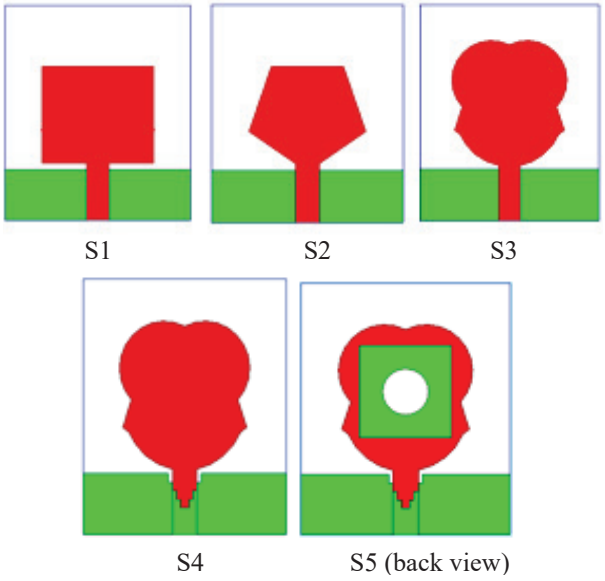

Fig. 2. Development steps of SUW antenna.

$|S_{11}|$ varies from 4.3 GHz to 22.7 GHz. The radiator is modified into a polygon shape in step 2, to enhance the 10 dB IBW and improved impedance matching where $|S_{11}|$ varies from 3.7-23.6 GHz. Three circular stubs are consummated with the polygon-shape radiator in step 3, to convert into a tree-shape structure which increases the electric length and smoothen the current movement in the radiator and 10 dB IBW is obtained from 3.6 - 15.5 GHz and 18.1 - 24.1 GHz. Figure 3 (a) depicts the variations in $|S_{11}|$ of step 1 to step 3. To advance the impedance matching the stair-shaped defects are created in the bottom plane in step 4 to obtain the characteristics of SUW and 10 dB IBW is obtained from 3.5 - 66.5 GHz. In step 5, a parasitic stub with a circular slot is embedded in the ground that acts as a stopband and creates a notch from 5.0 GHz to 5.4 GHz. Figure 3 (b) depicts the variations in $|S_{11}|$ of step 4 & 5 and Fig. 3 (c) shows the final 10 dB IBW of SUW antenna. The presence of a circular defect in the parasitic stubs creates perturbation of current distribution and the electric current flowing on the ground has to face a longer path. This perturbation of the path creates a change in inductance (L). Similarly, the second effect of aperture in the ground plane is due to the gap located below the strip conductor. The thin gap determines an accumulation of charge and consequently can be investigated as series capacitance (C). The combination of these two singularities creates an equivalent parallel LC circuit which results in a notch band from 5.0 GHz to 5.4 GHz frequency which can prevent the WLAN frequencies in UWB applications. Figure 3 (d) is demonstrating the current circulation in the antenna with the parasitic stub.

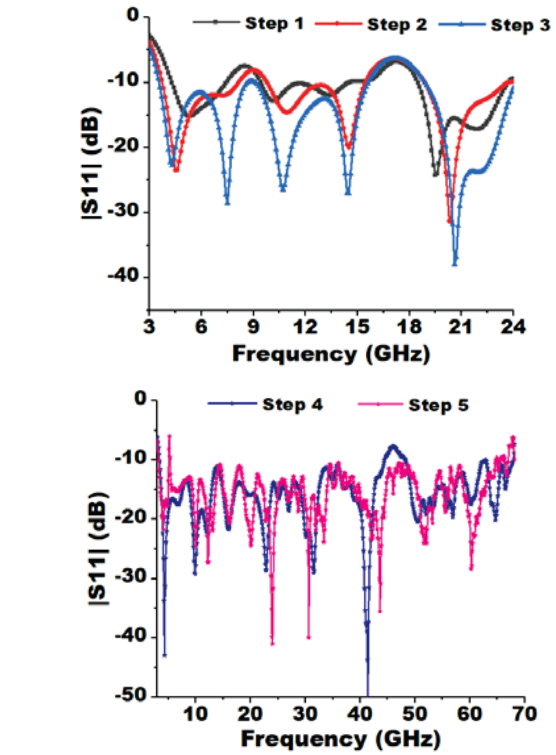

(a) and (b)

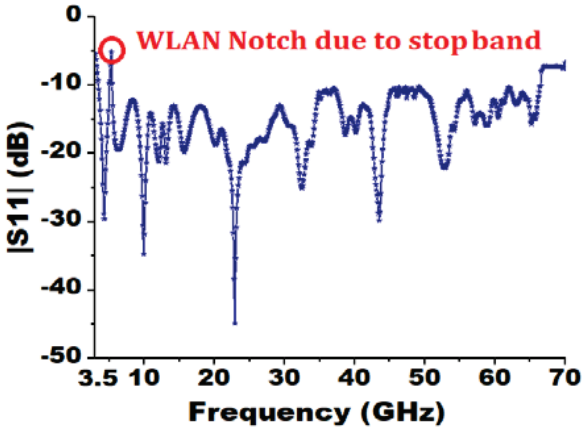

(c)

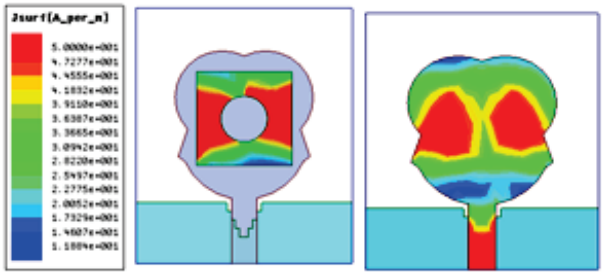

(d)

Fig. 3. (a) and (b) Variation in $|S_{11}|$ for Step 1 to Step 5. (c) Obtained $|S_{11}|$ of proposed SUW antenna with notch. (d) Surface current distribution in the presence of parasitic stub and a circular slot at 5.1 GHz frequency.

Table 1: Comparative study of proposed SUW antenna with the recent works

Ref.	Size $(\lambda_0)^2$	10 dB IBW (GHz)	BW %	BDR
2	0.345 × 0.345	2.59-31.14	169	1419.86
3	0.325 × 0.368	0.65-35.61	193	1613.7
4	0.347 × 0.358	1.68-26	175.72	1414.5
5	0.32 × 0.34	3.8-68	179	3015
6	0.37 × 0.42	1.02-24.1	183	1167
7	0.55 × 0.38	3.0-35.0	168	805
8	0.31 × 0.46	3.15-32	164	1102.9
9	0.33 × 0.416	2.5-110	191	1391
Proposed work	0.29 × 0.35	3.5-66.5	180	1773.4

III. SUW ANTENNA PARAMETERS

SUW antenna should have a BDR of 10:1, and with this BDR antenna can be designed without the restriction of predefined bandwidth. SUW antenna is used in long and short-range of communication, the parameters like BW % and BDR determines the performance of the antenna with realized gain, radiation efficiency and far-field analysis. BDR reflects the compactness as well as measures fractional usable bandwidth in SUW antenna. A higher value of BDR assures the wideband characteristics and the compactness of the antenna. It can be calculated with given eqn (3) [1].

$$\mathrm{BDR} = \frac{\mathrm{BW}\ \%}{\lambda_L \times \lambda_W}, \tag{3}$$

where λ_L represents the electrical length and λ_W represents the electrical width of the antenna and BW% can be estimated with the given eqn (4) [1].

$$\mathrm{BW}\% = \frac{f_H - f_L}{f_C} \times 100, \tag{4}$$

where f_H and f_L are the lower and higher frequency in operating bandwidth and center frequency f_C is calculated by arithmetical mean. The calculated value of BW% and BDR are 180 and 1773.4 respectively.

IV. FSS EVOLUTION AND ANALYSIS

The proposed FSS is designed for UWB frequency application where the FSS superstrate is positioned below the antenna. The gain enhancement in the antenna is obtained maximum when the reflection of EM waves from the FSS superstrate and radiation of the antenna is in the same direction. The FSS unit cell is designed for frequency 3.5 to 10 GHz with a modified SRR structure. The FSS evolution and FSS analysis as discussed below.

A. FSS evolution

To determine the dimensions of the FSS superstrate eqn (5) [16] is used as given below.

$$\mathrm{Pr} < \frac{\lambda p}{(1 + Sin\theta)}, \tag{5}$$

where Pr is the periodicity of the unit cell, wavelength λ_p is obtained from the maximum frequency in the operating band and incident wave angle is θ. At $\theta = 0^\circ$ and for frequency 10 GHz, the obtained λ_p is 30 mm, therefore the dimensions of the unit cell is considered only 14 mm x 14 mm with the electric length of $0.16\lambda_0 \times 0.16\lambda_0$. The FSS unit cell is developed in four stages as depicted in Fig. 4 (a). The FSS unit cell dimensions are as follows, W2 = 4 mm, L4 = 6 mm, W1 = 14 mm, L3 = 7 mm, W4 = 2 mm, L2 = 6 mm, W3 = 10 mm and L1 = 14 mm as illustrated in Fig. 4 (b). The fabricated FSS and the s-parameters of evolution steps of the FSS superstrate are shown in Figs. 4 (c) and (d). A square shape FSS is designed in step(S)-1, to obtain stopband characteristics in UBW frequency. The $|S_{12}|$ is varying from 3 GHz to 10 GHz, demonstrating weak stopband characteristics. In step 2, SRR is introduced with 1 mm uniform width (Fw) in the FSS unit cell to improve the stopband charac-

(a)

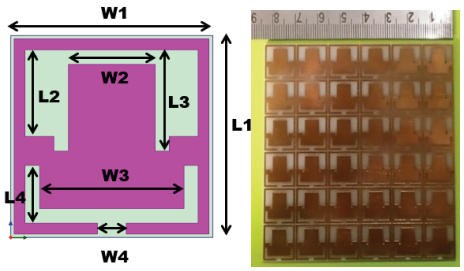

(b) (c)

Fig. 4. *Continued.*

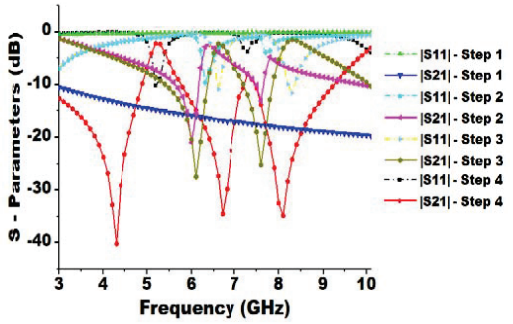

(d)

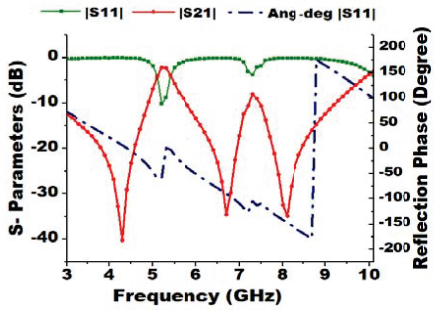

(e)

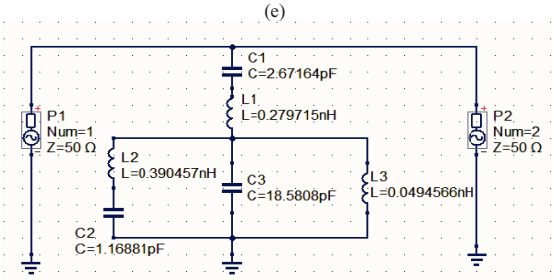

(f)

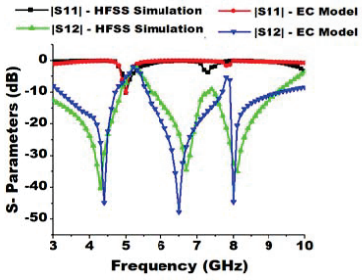

(g)

Fig. 4. (a) FSS evolution steps. (b) FSS unit cell dimensions. (c) Hardware prototype of FSS. (d) S-parameters associated with evolution steps. (e) Extracted EC model of unit cell. (f) FSS s-parameters with variation in reflection phase angle. (g) S-parameters of the proposed unit cell using HFSS simulation and EC model.

teristics where $|S_{12}|$ is varying from 5.6 GHz to 7.2 GHz. In step 3, the structure of SRR is modified and improved $|S_{12}|$ bands are obtained which are varying from 5.6 GHz 7.8 GHz but still, the stopband characteristics are not obtained in the lower operating band. Finally in step-4, the FSS unit cell is further modified which increase the electric length and improves the stopband characteristics but keeping in the mind the notch characteristics of the antenna, the stopband characteristics mitigate from the unit cell. The final $|S_{12}|$ is varying from 3.0 GHz to 10 GHz except notch band where it reveals that stopband characteristics are diminished from the results where the antenna demonstrates the notch band. The phase angle of $|S_{11}|$ varies linearly in entier frequency range and decreases when the frequency is increasing except the notch band as shown in Fig. 4 (e).

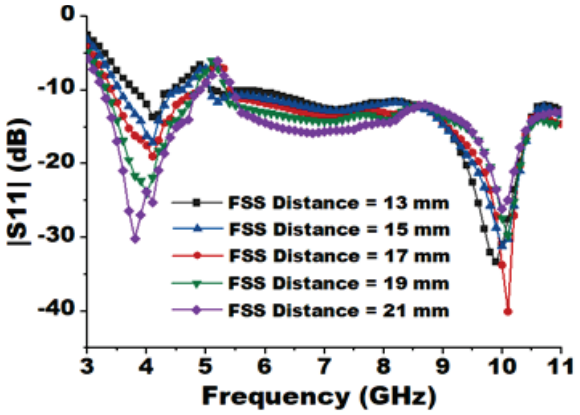

(a)

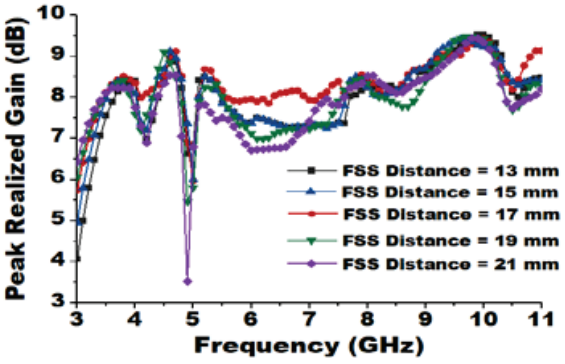

(b)

Fig. 5. (a) $|S_{11}|$. (b) Realized gain at different distance between FSS and proposed antenna.

The equivalent circuit (EC) model of the FSS unit cell is designed using QUCS software with lumped components as depicted in Fig. 4 (f). The lumped elements of the circuit are determined from the eqn (6) and (7) [16] where three capacitive elements C1, C2 and C3 have values of 2.67 pF, 1.16 pF and 18.58 pF along with three inductive elements L1, L2 and L3 with values of 0.276 nH, 0.39 nH and 0.049 nH.

Table 2: Comparative analysis of proposed gain enhancement technology with the other recent works

Ref.	Antenna Size (mm^2)	Technology used	Operating Band (GHz)	Gain Enhancement (dB)
11	64 × 64	AMC	3.36, 5.96, 9.09	3.58
12	70 × 70	AMC	1.9–6.95	3.06
14	38 × 38	Metamaterial	2.4–5.82	3.69
16	35 × 25	Metamaterial	5.6–10.3	3.2
17	30 × 30	Single layer FSS	3.6–6.1	4.0
18	20 × 27	Single layer FSS	4.7–14.9	4.5
19	63.65 × 51.16	Single/dual layer FSS	2.4	4.4
20	35 × 30	Single layer FSS	3.0–13.4	4
21	40 × 30	Dual-layer FSS	8.1–13.2	3.3
Proposed work	25 × 30	Single layer FSS	3.5–11.0	5.2

$$\frac{X_L}{Z_0} = \omega L = \frac{w_1}{L_1}\,\mathrm{Cos}\theta\; F(L_1, 2F_w, \theta, \lambda). \quad (6)$$

$$\frac{B_C}{Y_0} = \omega C = 4\varepsilon_r \frac{w_1}{L_1}\,\mathrm{Sec}\theta\; F(L_1, h, \theta, \lambda), \quad (7)$$

where w_1, L_1, the FSS width, length, h is the and θ is the incidence angle. The extracted s-parameters from EC model are compared with the simulated values using HFSS-13 simulator as depicted in Fig. 3 (g) where both are having similar variations. The advance simulation techniques as a prospective are used to extract the solution for nonconformal meshes of EM wave [24], To solve anisotropic Maxwell's equations [25] and Phase Synthesis of Beam-Scanning in Deep Learning Technique [26].

B. FSS analysis

The separation of FSS superstrate from the antenna is the vital parameter for gain enhancement and it can be calculated with eqn (8) [16] as given below.

$$\varphi_{FSS} - 2KF_d = 2N\pi. \quad (8)$$

In the equation, F_d is the distance of the antenna from FSS and K is constant which is equal to $2\pi/\lambda$. The value of N can be chosen for any integer value and λ is the wavelength at which the reflection phase is zero. The reflection phase is 0° at 4.4 GHz frequency as depicted in Fig. 4 (e) and at this frequency, the value of $\lambda/4$ is 17.02 mm. Keeping this in mind that the position of FSS is varied from 13 mm to 21mm and the variation in

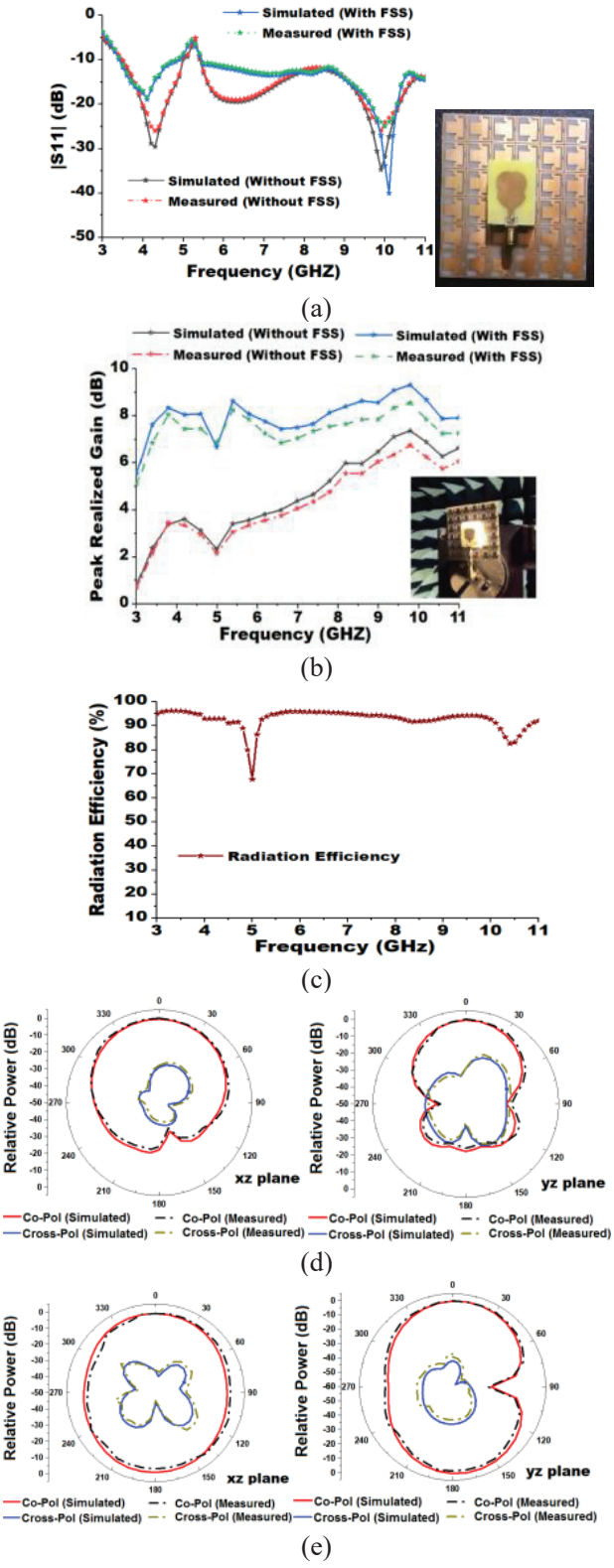

Fig. 6. (a) Measured $|S_{11}|$ with simulated values. (b) Measured peak gain. (c) Radiation efficiency. (d) and (e) Radiation patterns at frequency 4.1 GHz and 7.50 GHz in x-z and y-z coordinates with FSS superstrate.

|S11| and peak gain are observed. The |S11| of antenna is having minor variations after the notch band irrespective of the FSS superstrate position but the lower operating bandwidth reduces when FSS distance behind the antenna decreases as depicted in Fig. 5 (a). The peak gain with the FSS superstrate at different placement is illustrated in Fig. 5 (b) where at the 17 mm distance, the minimum variations are observed and maximum gain enhancement is achieved 5.2 dB. Therefore 17 mm optimum distance is finalized between FSS superstrate and antenna where the 10 dB IBW is varying from 3.5 GHz to 11 GHz and the peak gain is having a maximum value of 9.46 dB.

V. RESULT AND DISCUSSION

HFSS-13 software is used to simulate the proposed antenna and FSS design whereas experimental results of $|S_{11}|$ are obtained by Anritsu-MS2038C VNA and the far-field analysis is done in the anechoic chamber. The simulated $|S_{11}|$ of the antenna is varying from 3.5 GHz to 66.5 GHz with a WLAN notch band from 5 GHz to 5.4 GHz. As per VNA availability the $|S_{11}|$ measurement is carried out up to 11 GHz with and without FSS and the measured results have similarities with the simulated values as shown in Fig. 6 (a). The measured gain of the discussed antenna is shown in Fig. 6 (b) where the measured gain is having minor deviations which are less than 0.5 dB in the presence of FSS also. The gain enhancement is achieved up to 5.2 dB using a single layer FSS. The simulation radiation efficiency is found more than 85 % except for the notch band as illustrated in Fig. 6 (c). The measured and simulated radiation pattern with FSS are illustrated in Figures 5 (e) and 6 (d), at two centre frequencies in the x-z and y-z coordinate system which are demonstrating the omnidirectional radiation pattern. The comparative analysis with related work of SUW antenna is given in Table 1, which authorizes that the presented tree-shaped antenna is compact having an electrical length of $0.29\lambda_0 \times 0.35\lambda_0$. The BW % of the SUW antenna is 180 with a high value of BDR which is 1773.4. The gain enhancement with a single layer and single-sided FSS superstrate is compared with gain improvement existing technology in Table 2; it reveals that the proposed FSS enhances the gain effectively in the entire operating band up to 5.2 dB.

VI. CONCLUSION

The tree-shaped SUW antenna is designed with a novel parasitic stub in the ground demonstrating notch characteristics. The tree-shaped radiator is improving the operating bandwidth whereas defected ground enhances the impedance matching in the antenna. The parasitic stub with a circular slot in the bottom plane creates a WLAN notch in the antenna. The high value of BDR confirms the compactness of the proposed SUW antenna. The modified SRR based single-layer FSS superstrate is placed below the antenna which reflects the grating lobes and enhances the antenna gain up to 5.2 dB.

REFERENCES

[1] W. Balani, M. Sarvagya, T. Ali, M. M., Manohara Pai, J. Anguera, A. Andujar, and S. Das, "Design techniques of super-wideband antenna–existing and future prospective," *IEEE Access*, vol. 7, 2019.

[2] T. Okan, "A compact octagonal ring monopole antenna for super wideband applications," *Microw. Opt. Technol. Lett.*, vol. 62, no. 3, pp. 1237-1244, 2020.

[3] S. Singhal and A. K. Singh, "Elliptical monopole based super wideband fractal antenna," *Microw. Opt. Technol. Lett.*, vol. 62, no. 3, pp. 1324-1328, 2020.

[4] C. Á. Figueroa Torres, J. L. Medina Monroy, H. Lobato Morales, R. A. Chávez Pérez, and A. Calvillo Téllez, "A novel fractal antenna based on the Sierpinski structure for super wide band applications," *Microw. Opt. Technol. Lett.*, vol. 59, no. 5, pp. 1148-1153, 2017.

[5] S. Singhal and A. K. Singh, "CPW-fed hexagonal Sierpinski super wideband fractal antenna," *IET Microw. Antennas Propag.*, vol. 10, no. 15, pp. 1701-1707, 2016.

[6] J. Liu, S. Zhong, and K. P. Esselle, "A printed elliptical monopole antenna with modified feeding structure for bandwidth enhancement," *IEEE Trans. Antennas Propag.*, vol. 59, no. 2, pp. 667-670, 2010.

[7] A. Gorai, A. Karmakar, M. Pal, and R. Ghatak, "A CPW-fed propeller shaped monopole antenna with super wideband characteristics," *Progress Electromagn. Res. C*, vol. 45, pp. 125-135, 2013.

[8] S. Hakimi, S. K. A. Rahim, M. Abedian, S. M. Noghabaei, and M. Khalily, "CPW-fed transparent antenna for extended ultrawideband applications," *IEEE Antennas Wireless Propag. Lett.*, vol. 13, pp. 1251-1254, 2014.

[9] A. Seyfollahi and J. Bornemann, "Printed-circuit monopole antenna for super-wideband applications," pp. 654-655, 2018.

[10] A. Ghosh, "Gain enhancement of triple-band patch antenna by using triple-band artificial magnetic conductor," *IET Microwaves, Antennas Propag.*, vol. 12, no. 8, Art. no. 1400, 2018.

[11] B. Zhang, P. Yao, and J. Duan. "Gain-enhanced antenna backed with the fractal artificial magnetic conductor," *IET Microw. Antennas Propag.*, vol. 12, no. 9, Art. no. 1457, 2018.

[12] K. N. Paracha, "A dual band stub-loaded AMC design for the gain enhancement of a planar monopole antenna," *Microw. Opt. Technol. Lett.*, vol. 60, no. 9, 2018.

[13] J. H. Kim, C.-H. Ahn, and J.-K. Bang, "Antenna gain enhancement using a holey superstrate," *IEEE Trans. Antennas Propag.*, vol. 64, no. 3, Art. no. 1164, 2016.

[14] S. Roy and U. Chakraborty, "Gain enhancement of a dual-band WLAN microstrip antenna loaded with diagonal pattern metamaterials," *IET Commun*., vol. 12, no. 12, Art. no. 1448, 2018.

[15] N. Rajak, N. Chattoraj, and R. Mark, "Metamaterial cell inspired high gain multiband antenna for wireless applications," *AEU-Int. J. Electron. Commun*., vol. 109, pp. 23, 2019.

[16] A. Kumar, A. De, and R. K. Jain, "Gain enhancement using modified circular loop FSS loaded with slot antenna for sub-6 GHz 5G application," *Progress Electromagn. Res. Lett*., vol. 98, pp. 41-48, 2021.

[17] P. Das and K. Mandal, "Modelling of ultra-wide stop-band frequency-selective surface to enhance the gain of a UWB antenna," *IET Microw. Antennas Propag.*, vol. 13, no. 3, pp. 269-277, 2019.

[18] M. A. Belen, "Performance enhancement of a microstrip patch antenna using dual-layer frequency-selective surface for ISM band applications," *Microw. Opt. Technol. Lett*., vol. 60, no. 11, pp. 2730-2734, 2018.

[19] S. Kundu, A. Chatterjee, S. K. Jana, and S. K. Parui, "A compact umbrella-shaped UWB antenna with gain augmentation using frequency selective surface," *Radio Eng*., vol. 27, no. 2, pp. 448-454, 2018.

[20] G. S. Paul, K. Mandal, and A. Lalbakhsh, "Single-layer ultra-wide stop-band frequency selective surface using interconnected square rings," *AEU-Int. J. Electron. Commun.*, vol. 132, 2021.

[21] A. Bhattacharya, B. Dasgupta, and R. Jyoti, "Design and analysis of ultrathin X-band frequency selective surface structure for gain enhancement of hybrid antenna," *Int. J. RF Microw. Comput.-Aided Eng.*, 2020.

[22] A. F. Alsager, *Design and Analysis of Microstrip Patch Antenna Arrays*, 2011.

[23] Q. Y. F. Zhan, M. Zhuang, M. Yuan, and Q. H. Liu, "Stabilized DG-PSTD method with nonconformal meshes for electromagnetic waves," *IEEE Trans. Antennas Propag*., vol. 68, no. 6, pp. 4714-4726, 2020.

[24] Q. Zhan, Y. Wang, Y. Fang, Q. Ren, S. Yang, W.-Y. Yin, and Q. H. Liu, "An adaptive high-order transient algorithm to solve large-scale anisotropic Maxwell's equations," *IEEE Trans. Antennas Propag.*, vol. 70, no. 3, pp. 2082-2092, 2022.

[25] T. Shan, M. Li, S. Xu, and F. Yang, "Phase synthesis of beam-scanning reflectarray antenna based on deep learning technique," *Progress Electromagn. Res.*, vol. 172, pp. 41-49, 2021.

Pankaj Jha received B. Tech and M. Tech degree from Uttar Pradesh Technical University (Now AKTU), Lucknow, UP, India, He is currently pursuing Ph.D from Shobhit Institute of Engineering and Technology, (Deemed to be University) Meerut, UP, India. His research area includes micro strip antenna, Metamaterial inspired antenna, MIMO, FSS and wearable antenna.

Anubhav Kumar received B. Tech and M.Tech from Uttar Pradesh Technical University (Now AKTU), Lucknow, UP, India. He is currently pursuing Ph.D from Shobhit Institute of Engineering and Technology, (Deemed to be University) Meerut, UP, India. He has published many SCIE/ESCI and Scopus indexed research papers. His research interests include microstrip antenna, metamaterial, FSS, MIMO, Wearable antenna, EBG and Image processing.

Asok De did his Ph.D from Indian Institute of Technology, Kharagpur. He served as faculty at University of Delhi, University of Kolkata from 1984 to 1997. He was the founder Principal of Ambedkar Institute of Advanced Communication Technology and Research (2005-2012). He served National Institute of Technology Patna and Durgapur as a Director from 2012 to 2017. Professor De has published more than 200 research papers in International Journals and International conferences. He supervised 16 Ph.D scholars till now.

Spiral Resonator Arrays for Misalignment Compensation in Wireless Power Transfer Systems

Nunzia Fontana[1], Sami Barmada[1], Marco Raugi[1], Danilo Brizi[2], and Agostino Monorchio[2]

[1]Department of Energy, Systems, Territory and Construction Engineering
University of Pisa, 56122, Pisa, Italy
sami.barmada@unipi.it, nunzia.fontana@unipi.it, marco.raugi@unipi.it

[2]Department of Information Engineering
University of Pisa, 56122, Pisa, Italy
danilo.brizi@unipi.it, agostino.monorchio@unipi.it

Abstract – In this contribution, the authors focus on the use of a metasurface (physically implemented as a 2D array of spiral resonators) as an additional component of a two-coil Wireless Power Transfer (WPT) system, with the aim of increasing the robustness to misalignment between the transmitter and the receiver coils. Resonator arrays have been proven to have a positive effect on WPT systems' performance since they produce a focusing effect on the magnetic field; at the same time, they contribute to the reduction of the electric near field. In addition, we herein demonstrate how proper control over the metasurface's unit cells can contribute to making a WPT system more tolerant to misalignment. In particular, the comparison between metasurfaces of different sizes (keeping the same transmitting and receiving coils) and their optimization performed to improve misalignment robustness is proved by numerical simulations.

Index Terms – Metamaterials, metasurfaces, misalignment compensation, wireless power transfer.

I. INTRODUCTION

Wireless Power Transfer (WPT) apparatuses based on resonant multi-coil systems are becoming popular devices. Especially for low-power applications, WPT can be already considered a consumer-ready product, regulated by specific international standards such as Qi. At the same time, power levels up to hundreds of kilowatts can be delivered with the same concept (but with different and more complex systems) for applications such as e-mobility. In this latter case, more aspects should be taken into account in the design phase of the WPT system, such as electromagnetic shielding and cooling issues ([1–7]).

Electromagnetic shielding is a particularly important aspect when WPT apparatuses are used to power biomedical devices or implants due to the proximity of human tissue being at its maximum. Several solutions for the reduction of magnetic field leakage are available in the literature, employing shields and passive or active coil arrangements [8–13].

More recently, some research shows that metamaterials (most commonly implemented as 2D metasurfaces) can be useful to increase power transfer efficiency by focusing the magnetic field and not being excessively prone to eddy currents [14–15]. In addition, in [16]the authors demonstrated that the use of a metasurface can also improve the system's performance from the EMC point of view by reducing the electric near field produced by the transmitting side of a WPT system.

Nevertheless, all of the above-mentioned applications critically suffer from misalignment between the transmitter and the receiver; indeed, not perfectly aligned coils share a drastically reduced inductive mutual coupling, leading to a degradation of the global WPT performance (efficiency, amount of delivered power, flux leakage). In some commercial products, misalignment is solved by forcing the position between transmitter and receiver (i.e., in the wireless rechargeable toothbrushes). Unfortunately, this is not always a viable option, for obvious reasons. The authors demonstrated that the insertion of a metasurface between driving and receiving coils also mitigates the efficiency drop problem that arises from misalignment in a common inductive WPT system [17]. Other research groups proposed a tunable active version of the resonator's matrix, with the same purposes [18–19].

In this contribution, a study on a metasurface, in which each resonator is passive, is performed, with the goal of addressing the misalignment recovering purpose.

The analysis is conducted both by employing full wave electromagnetic software (for the system

Submitted On: July 30, 2022
Accepted On: August 28, 2022

https://doi.org/10.13052/2022.ACES.J.370703

characterization) together with a circuit simulator. Different optimization procedures are followed to find the best values of the capacitors that are connected to each single resonator of the metasurface

The practical implementation of the proposed compensation is case-dependent. If the geometrical structure of the system allows misalignment only along one direction, a direct solution without active devices, taking into account the results shown below, is feasible. In case the misalignment is completely not predictable, then the use of varicaps is needed.

The results obtained (and shown in this paper) demonstrate that the use of passive metasurfaces for misalignment compensation is possible, and constitutes a basis for the designers, evidencing how the size of the metasurface affects the performance of the system.

II. WORKING PRINCIPLE

The WPT configuration object of this study is a commonly used magnetic resonance-based system, in which a compensation network is present both at the transmitter and receiver sides; the compensation network makes the system resonant at a specific working frequency.

Instead of adopting additional repeater coils (typically one or two), a metasurface is specifically designed. Typically, all the metasurface elements are tuned at the same operating frequency of the two main coils (transmitter and receiver); moreover, the metasurface is usually positioned in between the two principal coils, at a specific distance from one of them, depending on the specific purpose it is designed for.

The authors in [16] demonstrated that an optimally designed metasurface, located in close proximity to the transmitter, reduces the electric field that could reach values above the limits recommended by the ICNIRP guidelines. In the same study, the authors performed an analysis of the geometrical characteristics of the metasurface, identifying, for this particular case, the optimal number of elements. This optimum allowed us to achieve the desired shielding level while maintaining an acceptable decrease in the performance due to increased losses in the metasurface itself.

By starting from this study, Fig. 1 shows the complete system after the design process, leading to an optimal configuration of the metasurface, i.e., a 5×5 matrix of resonators. The system has been designed and prototyped, showing that a real shielding effect can be achieved [16].

Figure 1, on the contrary, shows the same configuration but with the presence of a misalignment (indicated by *Dy*) between the transmitting and receiving coils. As anticipated, a misalignment between transmitter and receiver in resonant WPT systems reduces the coupling

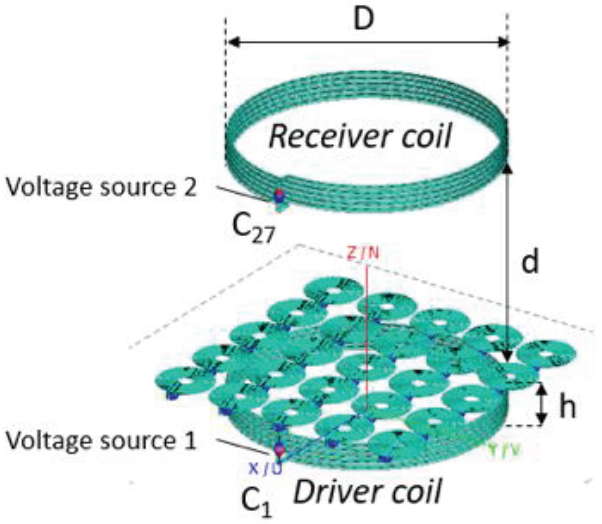

Fig. 1. Geometry of the proposed WPT system: (a) coaxial; (b) with a Dy misalignment along y axis.

coefficient, hence both the transmitted power and the efficiency. There are various techniques to reduce the misalignment effect on the performance, ranging from mechanical constraints to a closed loop communication between transmitter and receiver (implemented by the measurement of sensitive quantities such as currents, for instance), that gives feedback to the operator relative to the misalignment quantity.

In this contribution, the authors focus on the use of a passive metasurface as the means to recover the misalignment between transmitter and receiver. The advantage of this choice relies on the fact that no complex communication link should be created; in addition, a passive metasurface, if compared to an active device, avoids

the presence of complex networks for changing loading capacitors values. In [17], only a metasurface of specific dimensions was considered (coincident with the one shown in Fig. 1); in this case, the side of the square metasurface is coincident with the diameter of the transmitter and receiver coils. As demonstrated in [16], this solution reduces joule losses (that are introduced in the case of larger metasurfaces, i.e., with a higher number of resonators), but once one of the two coils is moved, there is a significant part of its surface that is projected outside the metasurface. This led the authors to investigate the possibility of employing larger metasurfaces that, despite being characterized by higher power losses, can reduce performance degradation in case of misalignment.

For this reason, the performances of metasurfaces of different dimensions are compared, and a procedure for the optimization of the loading capacitors' value is performed.

III. NUMERICAL METHODS

The CAD model of the system, as shown in Fig. 1, has been created with commercial electromagnetic software (Feko suite, Altair, Troy, MI, USA) based on the Method of Moments. In the full wave model, each coil of the WPT system (including the unit cells of the meta surface) terminates in a lumped port. The ports of the metasurface elements are, in turn, closed on a lumped capacitor; the port of the driver coil (transmitter) is terminated with a series connection between the generator and the proper resonant capacitor, while the port of the receiver is terminated with the resonant capacitor and resistive load.

A single full-wave simulation (for a given operation frequency) allows the characterization of the system as an N-port entity, represented by using the S or Z parameters matrix. In this particular case, $N-2$ ports are relative to the lumped loading capacitances of the metasurface unit cells (used to impose resonance of each resonator at the selected frequency) while the 2 remaining ports (labeled as Port 1 and Port 2) are relative to the transmitter and receiver, represented in Fig. 2 as a generator and a resistive load, respectively.

The rationale behind the choice of finding an equivalent circuit stands in the fact that we are not interested in the field distribution, but only in the performances of the system in terms of currents and voltages. Indeed, the efficiency of the system is calculated as:

$$\eta = \frac{P_{out}}{P_{in}} = \frac{\left|\dot{I}_2\right|^2 R_L}{R\left\{\dot{E}\dot{I}_1^*\right\}}. \tag{1}$$

Equation (1) applies to the N-port circuit represented in Fig. 2. A more synthetic representation would be the usual 2-port circuit, easily obtainable by the same full-wave model and not considering the capacitors as external ports, as in the following expression.

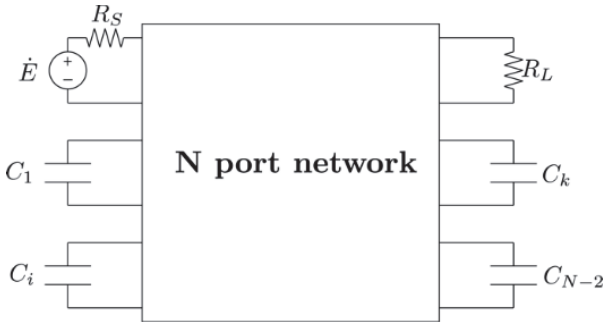

Fig. 2. N-port circuit representation of the proposed WPT system: N-2 ports are dedicated to the capacitive loads of the metasurface unit cells, while the first two are relative to the transmitting and receiving coils.

$$\eta = \frac{R_L|\underline{Z}_{21}|^2 R\{\underline{Z}_{in}\}}{|\underline{Z}_{22}+R_L|^2|\underline{Z}_{in}|^2}, \tag{2}$$

where:

$$\underline{Z}_{in} = R_s + \underline{Z}_{11} - \frac{\underline{Z}_{12}\underline{Z}_{21}}{R_L+\underline{Z}_{22}}. \tag{3}$$

While this synthetic representation would anyway allow the evaluation of the efficiency as in equations (1) and (2) and give more insight due to the explicit presence of the impedance parameters, it will not allow for an optimization of the capacitances to achieve misalignment compensation.

The calculations on the N-port circuit have been carried out by using the Keysight Advanced Design System (ADS) software, according to the following steps:

a. evaluation of the performance in case of perfect alignment between transmitter and receiver, with the capacitance value optimized to a specific single nominal value;
b. evaluation of the performances in case of misalignment, with the capacitances set to the nominal value (as in the previous simulation);
c. optimization the capacitances, with the goal of maximizing the efficiency level of the system in presence of misalignment.

The optimization procedure used in this paper is directly implemented in the software ADS; the number of parameters to be optimized is relatively high (the capacitance of each lumped element present in the metasurface, ranging from 25 to 81 in the following results), and the fitness function in equation (2) is relatively flat with a high number of local minima. However, the obtained results are sound and small differences in the value of the capacitances (obtained in different optimization runs) do not significantly affect the results. The authors also performed a set of Montecarlo analysis

(not shown here for the sake of conciseness) to verify how the system is robust towards capacitances variation due to tolerance, and the outcome confirm the validity of the results shown below.

IV. RESULTS

The numerical cases reported in this section have been obtained by employing the commercial tools mentioned before; in addition, the system named "test case #1" has been also implemented in a lab experiment, as described below. On the contrary, the test cases with metasurfaces of larger dimensions have been implemented only numerically. All the simulations results are characterized by a voltage source of amplitude $\dot{E} = 1V$, since the goal of the analysis is to validate the working principle of the proposal. Both the generator and the load resistances (R_s and R_L respectively) have been chosen equal to 50Ω.

A. Test case #1: metasurface and coils characterized by the same dimension

The first results are relative to the experimental setup proposed in [16], in which the metasurface is a square slab with the side coincident with the diameter of the transmitting and receiving coils, fabricated with a 3D printing process. The slab was engraved with spiral grooves following the unit cells profile thanks to a commercial 3D printer. Table 1 shows the main geometrical quantities, while Fig. 3 shows the system during the experiments performed and described in [16].

In this nominal case, the optimal value of the capacitances that leads to the higher efficiency level is $C_{nom} = 585pF$. A full-wave simulation with all the unit cells tuned with C_{nom} has been carried out to obtain the efficiency (as defined in equations (1) - (3)) and the power delivered to the load, respectively $\eta = 0.57$, $P_L = 0.37mW$.

Later, the same simulation has been performed in the case of a misalignment of the receiver, where $D_y = 6cm$ (see Fig. 4).

Table 1: Geometrical quantities of the system

Quantity	Value
Tx diameter	$D = 18cm$
Rx diameter	$D = 18cm$
Operating frequency	$f_0 = 6\ MHz$
Slab thickness	$l = 5mm$
Unit cell conductor diameter	$d_{copper} = 1.4mm$
Unit cell average diameter	$d_{cell} = 40mm$
Slab distance from the transmitter	$1.4cm$
Number of resonators	5×5

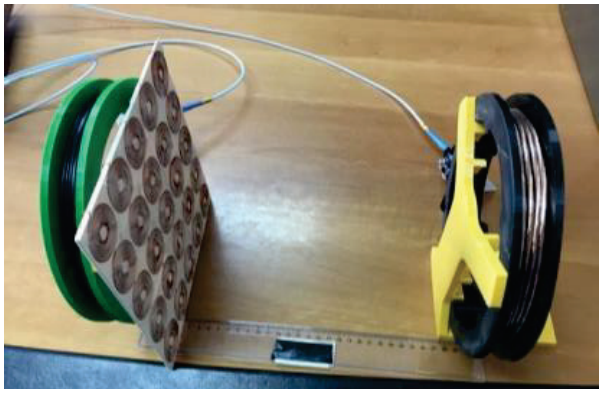

Fig. 3. Experimental setup. The metasurface is placed few millimeters above the driving coil.

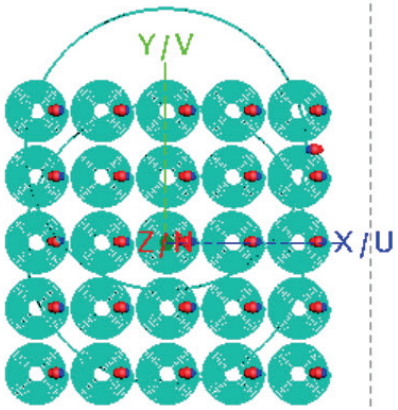

Fig. 4. Representation of the WPT system with the misaligned receiver.

In the misaligned configuration, the performances are summarized by efficiency and power as $\eta = 0.49$, $P_L = 0.27mW$, which is lower with respect to the previous nominal case.

To improve the performances in case of misalignment, different values of the tuning capacitors are considered; the optimization procedure has now been set to optimize every single capacitance. This result in new values of efficiency and power to the load, respectively $\eta = 0.52$, $P_L = 0.36mW$.

As it is evident from the previous values, the new capacitances allow a partial recovery both of the efficiency and the power delivery levels.

Figure 5 shows a 5×5 colormap matrix in which the values of the capacitances are associated with their position in the metasurface. At a first glance, it can be easily noted that in areas of the metasurface not covered by the misaligned receiver, the capacitance assumes a higher value, i.e., the single resonator is characterized by a higher inductive behavior.

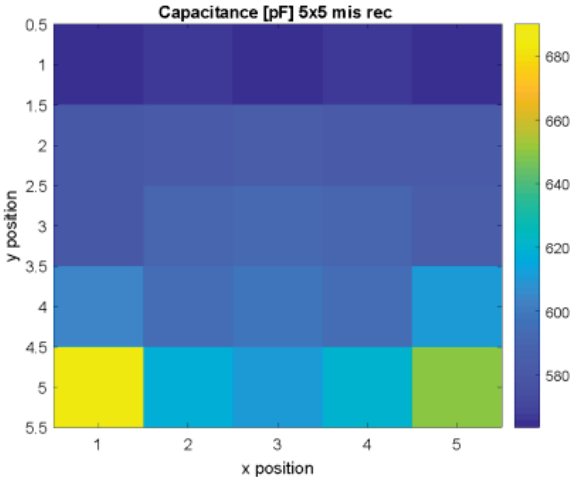

Fig. 5. Values of the tuning capacitors in the metasurface with 5×5 elements.

B. Test case #2: metasurface side larger than coils diameters (7×7 elements)

In this second case, the authors simulated the presence of a slab of wider dimension, i.e., whose side is larger than the transmitting and receiving coil diameters. The metasurface is now composed of a 7×7 matrix of the same identical spiral resonators, with the aim of investigating the possibility of an increased capability misalignment compensation. The new test case is shown in Fig. 6, both in the aligned and in the misaligned configuration.

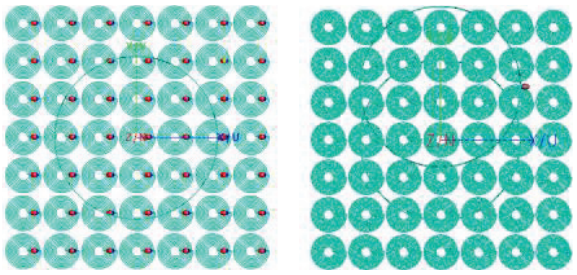

Fig. 6. WPT system with 7×7 metasurface, with the receiver in aligned position (left) and misaligned position (right).

In the nominal case, the optimal value of the capacitances that leads to the higher efficiency is $C_{nom} = 598pF$; with all the unit cells tuned with C_{nom}, the efficiency and the power delivered to the load, respectively, are $\eta = 0.57$, $P_L = 0.77mW$.

The simulation has been replicated in presence of the same misalignment $D_y = 6cm$ (see Fig. 6). It is worth noticing that, in this case, the slab 7×7 (characterized by increased size) covers both the transmitter and the receiver also in the misaligned configuration, leading to a potentially higher capability of misalignment recovery.

In this case, the performances are summarized by efficiency and power as $\eta = 0.52$, $P_L = 0.61mW$, that are lower with respect to the previous nominal case. At the same time, a newsworthy result is derived: the performance decrease is lower if compared to the previous case.

The same optimization procedure has been performed in this case, resulting in new values of the selected performance parameters, respectively $\eta = 0.56$, $P_L = 0.59mW$.

As it is evident from the previous values, the new capacitances allow an almost complete recovery of the efficiency also in the misaligned configuration.

Figure 7 shows a 7×7 colormap matrix in which the values of the capacitances are associated with their position in the metasurface. Again, it is easy to verify that in the section of the metasurface not covered by the misaligned receiver, the capacitance assumes a higher value.

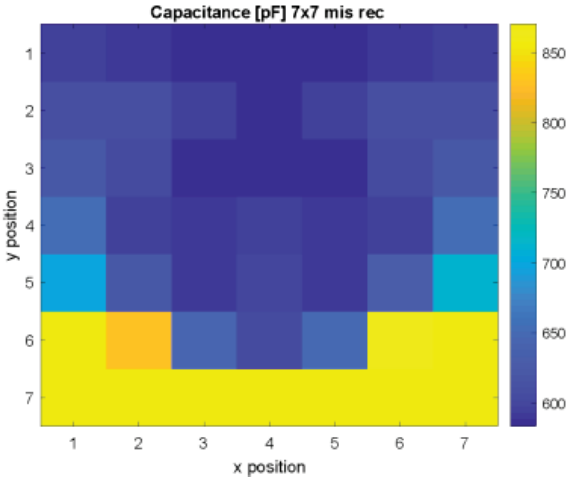

Fig. 7. Values of the tuning capacitors in the metasurface with 7×7 elements.

C. Test case #3: metasurface side larger than coils diameters (9×9 elements)

In the final case shown in this paper, the authors simulated the presence of a slab of an even wider dimension, i.e., a matrix of 9×9 resonators. The new test case is shown in Fig. 8, both in the aligned and in the misaligned configuration.

In the nominal case, the optimal value of the capacitances that leads to the higher efficiency is $C_{nom} = 607pF$; with all resonators tuned with C_{nom} the efficiency and the power delivered to the load, respectively are $\eta = 0.52$, $P_L = 1.3mW$.

The same simulations have been performed in presence of the same misalignment $D_y = 6cm$ (see Fig. 8). In this case, the performances are summarized by efficiency and power as $\eta = 0.48$, $P_L = 1.13mW$, which are lower with respect to the previous nominal case. In the present

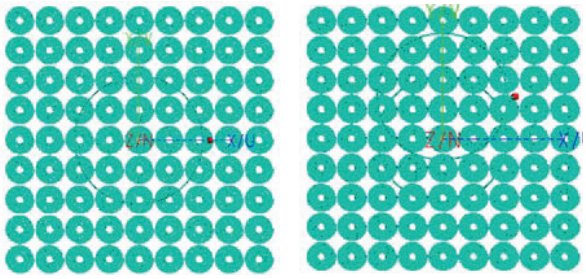

Fig. 8. WPT system with 9×9 metasurface, with the receiver in aligned position (left) and misaligned position (right).

case, an already observed and interesting trend is confirmed: the performance decrease is lower if compared to the previous cases.

The same optimization procedure has been performed in this case, resulting in new values of the selected performance parameters, respectively $\eta = 0.51$, $P_L = 0.59mW$.

In this case, the recovery in terms of efficiency is practically total, even though it is performed at the cost of a lower power delivered to the load.

Figure 9 shows a 9×9 colormap matrix in which the values of the capacitances are associated with their position in the metasurface. Again, it is easy to verify that in the section of the metasurface not covered by the misaligned receiver, the capacitance assumes a higher value, suggesting a systematic behavior that the metasurface needs to present with the aim of compensating for the misalignment introduction in a specific direction, thus confirming what already guess by the authors in [17].

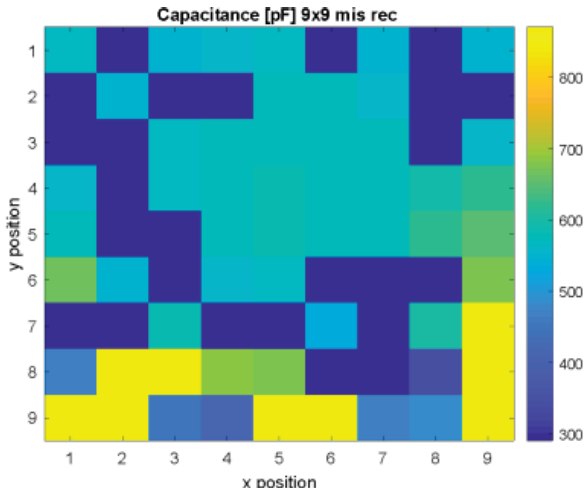

Fig. 9. Values of the tuning capacitors in the metasurface with 9×9 elements.

D. General comments

The following overall trend can be evidenced:

- The nominal capacitance capable of making the whole system resonate at $f_0 = 6\ MHz$ slowly increases with the dimension of the metasurface. This is due to the known frequency shifting phenomenon caused by the mutual coupling between all the metasurface elements. The larger the metasurface, the higher the mutual coupling contribution coming from the surrounding cells.
- An increase of the dimension of the metasurface above a certain limit, causes a reduction of the efficiency, because of the joule losses in the high-number resonators. Moreover, the unit cells far from the center of the Tx or Rx coils have practically no effect on the field focusing.
- An increase in the dimension of the metasurface allows a lower performance degradation in case of misalignment.
- An increase in the dimension of the metasurface allows a stronger efficiency recovery when the values of the capacitances are properly selected.
- The inductive behavior of the single resonators appearing in case of misalignment (of the areas of the metasurface not covered by the misaligned receiver) can be explained by the need of reducing the current in these particular resonators to redistribute the magnetic field spatial configuration, that is achieved with an increase of the equivalent inductance.

Considering all the previous points, from the economical point of view, the inclusion of a passive metasurface in a WPT system does not significantly affect its overall cost. In case the metasurface is implemented with the use of varicaps, the main cost increase would be relative to the varicaps control circuit, but in the authors' opinion, it will not anyway be comparable with the cost of the high-frequency AC power supply.

V. CONCLUSION

In this paper the authors investigated the use of passive metasurfaces as a tool for the compensation of misalignment in wireless power transfer systems. Starting from a system implemented in the lab, the authors have simulated metasurfaces of different dimensions and verified that, when they are properly designed, they can contribute to the reduction and compensation of performance degradation, in case a perfect placement of the transmitter and receiver coil cannot be guaranteed.

REFERENCES

[1] A. P. Sample, D. A. Meyer, and J. R. Smith, "Analysis experimental results, and range adaptation of

magnetically coupled resonators for wireless power transfer," *IEEE Trans. Ind. Electron.*, vol. 58, no. 2, pp. 544-554, Feb. 2011.

[2] G. Wang, W. Liu, M. Sivaprakasam, and G. A. Kendir, "Design and analysis of an adaptive transcutaneous power telemetry for biomedical implants," *IEEE Trans. Circuits Syst. I, Reg. Papers*, vol. 52, no. 10, pp. 2109-2117, Oct. 2005.

[3] A. K. RamRakhyani, S. Mirabbasi, and M. Chiao, "Design and optimization of resonance-based efficient wireless power delivery systems for biomedical implants," *IEEE Trans. Biomed. Circuits Syst.*, vol. 5, no. 1, pp. 48-63, Feb. 2011.

[4] C.-S. Wang, O. H. Stielau, and G. A. Covic, "Design considerations for a contactless electric vehicle battery charger," *IEEE Trans. Ind. Electron.*, vol. 52, no. 5, pp. 1308-1314, Oct. 2005.

[5] M. Bertoluzzo, P. Di Barba, M. Forzan, M. E. Mognaschi, and E. Sieni, "Multiobjective optimization of compensation networks for wireless power transfer systems," *COMPEL - The International Journal for Computation and Mathematics in Electrical and Electronic Engineering*, vol. 41, no. 2, pp. 674-689, 2022.

[6] M. Song, P. Belov, and P. Kapitanova, "Wireless power transfer inspired by the modern trends in electromagnetics," *Appl. Phys. Rev.*, vol. 4, no. 2, Art. no. 021102, Jun. 2017.

[7] J. Shin, S. Shin, Y. Kim, S. Ahn, S. Lee, G. Jung, S.-J. Jeon, and D. H. Cho, "Design and implementation of shaped magnetic-resonance- based wireless power transfer system for roadway-powered moving electric vehicles," *IEEE Trans. Ind. Electron.*, vol. 61, no. 3, pp. 1179-1192, Mar. 2014.

[8] I. Lee, N. Kim, I. Cho, and I. Hong, "Design of a patterned soft magnetic structure to reduce magnetic flux leakage of magnetic induction wireless power transfer systems," *IEEE Trans. Electromagn. Compat.*, vol. 59, no. 6, pp. 1856-1863, Dec. 2017.

[9] M. Mohammad, E. T. Wodajo, S. Choi, and M. E. Elbuluk, "Modeling and design of passive shield to limit EMF emission and to minimize shield loss in unipolar wireless charging system for EV," *IEEE Trans. Power Electron.*, vol. 34, no. 12, pp. 12235-12245, Dec. 2019.

[10] S. Lee, D.-H. Kim, Y. Cho, H. Kim, C. Song, S. Jeong, J. Song, G. Park, S. Hong, J. Park, K. Cho, H. Lee, C. Seo, S. Ahn, and J. Kim, "Low leakage electromagnetic field level and high efficiency using a novel hybrid loop-array design for wireless high power transfer system," *IEEE Trans. Ind. Electron*, vol. 66, no. 6, pp. 4356-4367, Jun. 2019.

[11] Q. Zhu, Y. Zhang, Y. Guo, C. Liao, L. Wang, and L. Wang, "Null-coupled electromagnetic field canceling coil for wireless power transfer system," *IEEE Trans. Transport. Electrific.*, vol. 3, no. 2, pp. 464-473, Jun. 2017.

[12] M. Bertoluzzo, P. Di Barba, M. Forzan, M. E. Mognaschi, and E. Sieni, "Field models for the electromagnetic compatibility of wireless power transfer systems for electric vehicles," *Engineering Computations*, vol. 39, no. 7, pp. 2802-2819, 2022.

[13] T. Campi, S. Cruciani, F. Maradei, and M. Feliziani, "Magnetic field mitigation by multicoil active shielding in electric vehicles equipped with wireless power charging system," in *IEEE Transactions on Electromagnetic Compatibility*, vol. 62, no. 4, pp. 1398-1405, Aug. 2020. doi: 10.1109/TEMC.2020.2988463.

[14] Y. Cho, S. Lee, D.-H. Kim, H. Kim, C. Song, S. Kong, and J. Park, "Thin hybrid metamaterial slab with negative and zero permeability for high efficiency and low electromagnetic field in wireless power transfer systems," *IEEE Trans. Electromagn. Compat.*, vol. 60, no. 4, pp. 1001-1009, Aug. 2018.

[15] Y. Cho, J. J. Kim, D.-H. Kim; S. Lee, H. Kim, and C. Song, "Thin PCB-type metamaterials for improved efficiency and reduced EMF leakage in wireless power transfer systems," *IEEE Trans. Microw. Theory Techn.*, vol. 64, no. 2, pp. 353-364, Feb. 2016.

[16] D. Brizi, N. Fontana, M. Tucci, S. Barmada, and A. Monorchio, "A spiral resonators passive array for inductive wireless power transfer applications with low exposure to near electric field," in *IEEE Transactions on Electromagnetic Compatibility*, vol. 62, no. 4, pp. 1312-1322, Aug. 2020. doi: 10.1109/TEMC.2020.2991123.

[17] N. Fontana, D. Brizi, S. Barmada, M. Raugi, and A. Monorchio, "Optimization and robustness analysis of a spiral resonators array for misalignment recovering purposes in WPT systems," *2021 XXXIVth General Assembly and Scientific Symposium of the International Union of Radio Science (URSI GASS)*, pp. 1-3, 2021.

[18] A. L. A. K. Ranaweera, C. A. Moscoso, and J.-W. Lee, "Anisotropic metamaterial for efficiency enhancement of mid-range wireless power transfer under coil misalignment," *J. Phys. D: Appl. Phys.*, vol. 48, pp. 8, 2015. doi: 10.1088/0022-3727/48/45/455104.

[19] H. N. Bui, T. S. Pham, J.-S. Kim, and J.-W. Lee, "Field-focused reconfigurable magnetic metamaterial for wireless power transfer and propulsion of an untethered microrobot," *Journal of Magnetism and Magnetic Materials*, vol. 494, pp. 165778, ISSN 0304-8853, 2020. https://doi.org/10.1016/j.jmmm.2019.165778.

Nunzia Fontana received an M. Sc. (summa cum laude) in telecommunications engineering and a Ph.D. in remote sensing from the University of Pisa, Italy, in 2008 and in 2012, respectively. She is an Associate Professor of Electrical Engineering with the Department of Energy, Systems, Territory and Construction Engineering, University of Pisa. Her research interests include wireless power transfer; antennas, impedance matching networks design, prototyping, and RF testing, radio frequency coils design for magnetic resonance and RF testing, and bio-electromagnetics. Her research activities have been published in several international scientific journals and in a number of international conference proceedings. She is IEEE Senior Member and Applied Computational Electromagnetics Society (ACES) Member. Prof. Fontana serves as an Associate Editor for ACES Journal.

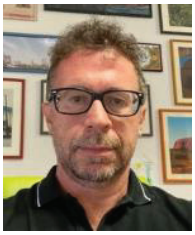

Sami Barmada received M.S. and Ph.D. degrees in electrical engineering from the University of Pisa, Italy, in 1995 and 2001, respectively. He is currently a Full Professor with the Department of Energy and System Engineering, University of Pisa. He is an author and co-author of more than 180 papers in international journals and indexed conferences. His research interests include applied electromagnetics, electromagnetic fields calculation, power line communications, wireless power transfer devices, and nondestructive testing. Prof. Barmada is an Applied Computational Electromagnetics Society (ACES) Fellow and he served as ACES President from 2015 to 2017. He is a member of the International Steering Committee of the CEFC Conference and he has been the General Chairman and Technical Program Chairman of numerous international conferences.

Marco Raugi is a Professor of Electrical Engineering at the Department of Energy, Systems, Territory, and Construction Engineering. He graduated in Electronic Engineering from the University of Pisa in 1985 and received his Ph.D. in Electrical Engineering from the university in 1990. Main Research Topics are Computational Electromagnetics, Nondestructive testing magnetostrictive sensors, and Sustainable Energy Communities. The research activity of Professor Marco Raugi has produced more than 250 publications in international journals and conferences. The achievements of his studies have been acknowledged by several invitations to international conferences as session chairman or chairman of the editorial board and as the author of invited speeches and tutorials. He is currently the Vice-Rector for Applied Research and Technology Transfer of the University of Pisa, Head of the Interdepartmental Center for Research on Energy for Sustainable Development (CIRESS), and Chair Holder of the UNESCO/UNITWIN Chair "Sustainable Energy Communities".

Danilo Brizi was born in Viterbo, Italy, in 1992. He received an M.S. Laurea degree in biomedical engineering and a Ph.D. degree in information engineering (both summa cum laude) from the University of Pisa in 2016 and 2020, respectively. He is currently an Assistant Professor at the same university. His research interests include electromagnetic metasurfaces, MRI filter design, and wireless power transfer applications.

Agostino Monorchio is a Full Professor with the University of Pisa, Pisa, Italy. He received a Laurea degree in electronics engineering and the Ph.D. degree in methods and technologies for environmental monitoring from the University of Pisa, Pisa, Italy, in 1991 and 1994, respectively. He spent several research periods at the Electromagnetic Communication Laboratory, Pennsylvania State University, State College, PA, USA, both as a recipient of a scholarship (Fellowship Award) of the Summa Foundation, Albuquerque, NM, USA, and in the framework of CNR-NATO Senior Fellowship program. He has carried out considerable research activity and technical consultancy to national, EU, and U.S. industries, coordinating, as Principal Scientific Investigator, a large number of national and European research projects.

He is active in a number of areas including computational electromagnetics, microwave metamaterials, radio propagation for wireless systems, the design and miniaturization of antennas and electromagnetic compatibility, and biomedical applications. The activity is mainly carried out at the Microwave and Radiation

Laboratory (www.mrlab.it), Department of Information Engineering, University of Pisa, together with a large group of Ph.D. students, Postdocs, and Research Associates. His research results have been published in more than 130 journal papers and book chapters, and more than 200 communications at international and national conferences. He is a co-author of four patents.

Prof. Monorchio is a member of the RaSS National Laboratory, Consorzio Nazionale Interuniversitario per le Telecomunicazioni, Parma, Italy, and since 2010 he has been with the Pisa Section of INFN, the National Institute of Nuclear Physics. He was elevated to a Fellow by the IEEE for his contributions to computational electromagnetics and for the application of frequency selective surfaces in metamaterials in 2012.

Preparation and Electrical Testing of Double Top Gate Graphene Field-Effect Transistor

Jinbao Huang[1], Yun Wu[2], Bo Su[3], and Jingping Liu[4]

[1]School of Electronic and Optical Engineering
Nanjing University of Science and Technology
Nanjing 210094, China
huangjinbao@njust.edu.cn

[2]Science and Technology on Monolithic Integrated Circuits and Modules
Laboratory, Nanjing Electronic Device Institute, Nanjing 210016, China
wuyun012@126.com

[3]School of Electronic and Optical Engineering Nanjing
University of Science and Technology Nanjing, 210094, China
subo@njust.edu.cn

[4]School of Electronic and Optical Engineering
Nanjing University of Science and Technology
Nanjing, 210094, China
liujingping@njust.edu.cn

Abstract – In this paper, we prepare and test a graphene field-effect transistor with two top gates. The Fermi energy level of graphene can be adjusted by applying positive and negative voltages to the two top gates, and N-type and P-type graphene are formed in the channel region, thus inducing a graphene p-n junction. The current model is established using the gradual channel approximation (GCA) method, and the current and p-n junction characteristics of the device were obtained by formula simulations. Based on the principle of p-n junction luminescence, this device with graphene p-n junction is expected to achieve terahertz wave radiation with an appropriate optical resonant cavity.

Index Terms – current characteristics, GCA, graphene, p-n junction, terahertz.

I. INTRODUCTION

Graphene is a two-dimensional material with a hexagonal honeycomb-like planar lattice structure. As an emerging material, graphene is now used in a wide range of applications. For example, it can be used in electromagnetic devices such as various absorbers [1–3], due to its ability to change impedance by adjusting the bias voltage; It can be used in transistors [4–6] and antennas [7, 8] due to its excellent electrical and thermal properties; And most importantly, graphene materials are inextricably linked to terahertz science due to their unique band structure and linear dispersion relations. With carrier densities in the range of 10^9-10^{12} cm^{-2}, the plasma oscillation frequency of graphene materials lies in the terahertz band; Zero band gap graphene facilitates the generation of terahertz waves because the Fermi energy level in the p-n junction of graphene can be controlled by changing the gate to produce a smaller effective band gap encompassing the terahertz band. Terahertz has a lower wave frequency compared to the infrared and visible bands, and the terahertz conductance of graphene is stable when the frequency is changed, approximating the DC conductance over a wide range [9]; The bipolar electric field effect of graphene can be changed by applying an electric field to the Fermi energy level [10], and adjusting the Fermi energy level can also be achieved using light, magnetic fields, and chemical doping. Graphene has the above terahertz properties and is uniquely suited for research in the modulation, testing, and generation of terahertz waves.

Graphene FETs can be structurally classified into bottom-gate [11], top-gate [11–13], and double-gate type [14]. In conventional top-gate + back-gate p-n junction devices, the back gate is far from the graphene layer, challenging to regulate its Fermi energy level adequately. We designed a graphene field-effect transistor with 2 separated top gates in 2014 which was the first implementation at the time [15]. No one had made a device at the time, although others had proposed the double top gate

Submitted On: April 3, 2022
Accepted On: August 1, 2022

https://doi.org/10.13052/2022.ACES.J.370704

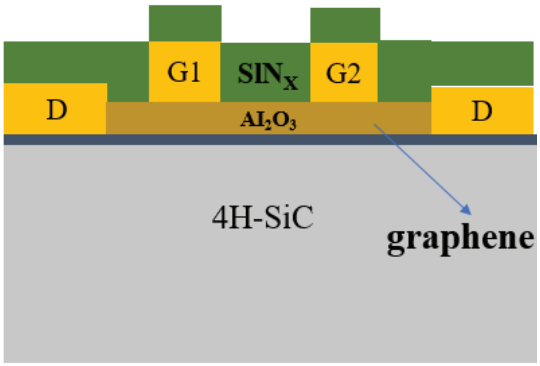

Fig. 1. Front view of DBR-DG-GFET.

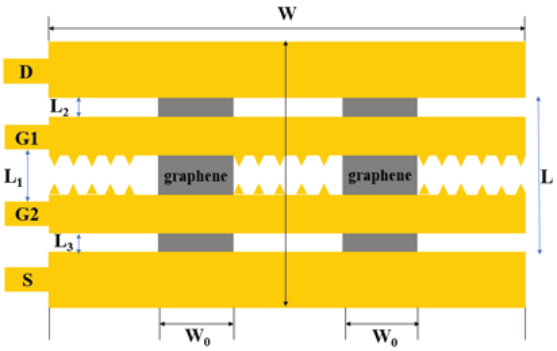

Fig. 2. Top view of DBR-DG-GFET.

structure. Its process does not require excessive energy injection while safeguarding the channel layer and improving stability. The current-voltage characteristics of the device are tested, and the results show that the gate voltage effectively induces the formation of a p-n junction in graphene, which is consistent with the theoretical analysis. Therefore, we will generate terahertz waves based on this gate-controlled p-n junction device in the future.

II. DESIGN AND WORKING PRINCIPLE

The front view of the device is shown in Fig. 1, graphene active region is between the dielectric layer AI_2O_3 and the substrate. The graphene substrate is 4H-SiC with a thickness of 500 μm, the source-drain, and two top-gate metal electrode uses Ti/Au (5/95 nm) alloy, the dielectric layer Al_2O_3 the waveguide SiNx (120 nm).

The top view of the device is shown in Fig. 2, graphene dimensions and the effect of graphene dimensions are as follows:

(1) Since only the zero-gap graphene can stably radiate terahertz photons, the graphene thickness must be 0.34 nm for a single layer.

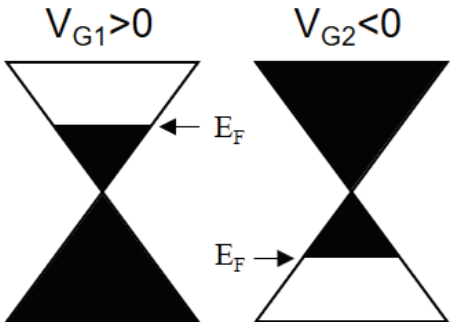

Fig. 3. Modulation of the Fermi energy level of graphene by a gate pressure.

(2) The total graphene length L is 260 μm, the distance between electrodes L_1= L_2 = 15 μm. The real impact on the output power is the length of the resonant cavity active region L_1. The smaller the gate gap L_0 the better but we set it to 30 μm due to the limitation of O_2 plasma etching.

(3) Graphene width W_0 is set as 100 μm. This value is influenced by the integration and fabrication process and is mainly determined by the design of the resonant cavity target

Figure 3 illustrates the Fermi energy level of graphene changes due to the gate voltage. With the positive gate voltage attracting electrons, the Fermi energy level moves upwards; The negative gate voltage attracts holes, so the Fermi energy level moves downwards, forming a p-n junction.

III. THEORETICAL CURRENT MODEL OF DG-GFET

Modeling the empirical channel current of the GFET helps us to analyze its electrical characteristic [16, 17]. Theoretical calculations are performed using GCA [17, 18] to clarify the operating mechanism of the DG-GFET under electrical injection.

With the source grounded, V_{G1} and V_{G2} are the gate voltages, and the forward bias voltage V_D is applied to the drain. Figure 4 shows a simplified device area containing only the insulating layer, metal gates, and channel, and the curve is the voltage drop along the channel. Both electrons and holes in DG-GFETs have the potential to become carriers due to the bipolar electric field effect of graphene, which is different from silicon-based transistors.

Where x is the length of a position in the channel area at x, the conductivity $\sigma(x,z) = n,p(x,z) \cdot e$. $n,p(x,z)$ is the number of electrons or holes per unit area. $Q = n,p \cdot e$ is the charge per unit area, L and W are the length and width of the channel, respectively. The carrier mobility defaults to a fixed value $\mu_{n,p}$, the conductance

at a point in the channel

$$g = \frac{\sigma(x,z)S(x,z)}{L} = \frac{W}{L}\int_0^{z_i}\sigma(z)\,dz$$
$$= \frac{W\mu_{n,p}}{L}\int_0^{z_i} e\cdot n,p(x,z)\,dz \quad (1)$$
$$= \frac{W\mu_{n,p}}{L}|Q(x)|,$$

where $Q(x) = -C_{ox}[V_G - V(x)]$ is the amount of charge stored per unit area at x, C_{ox} is the capacitance per unit area at the channel with $C_{ox} = \varepsilon\cdot\varepsilon_0/d$, ε and ε_0 is the insulation dielectric constant and vacuum dielectric constant, respectively. d is the insulation thickness, where V(x) is the bias voltage between x and the source. When dV the voltage varies on each dx, the microscopic expression for the drain current in the channel is

$$I_D = \mathrm{gL}\frac{dV}{dx} = \frac{W\mu_{n,p}|Q(x)|dV}{dx}$$
$$= \frac{W\mu_{n,p}}{L}C_{\mathrm{ox}}\frac{|V_G - V(X)|dV}{dx}, \quad (2)$$

then integrate from the source (x=0, V(x)=0) to the drain (x=L, V(x)=V_D) [19]

$$I_D = \frac{W\mu_{n,p}}{L}C_{\mathrm{ox}}\int_0^{V_D}|V_G - V(x)|\,dV. \quad (3)$$

As shown in Fig. 5 (a), if 0 < V_{G1}< V_D, V_{G2} = 0, the conducting carriers consist of two parts, the side near the source is electron accumulation, and from the source to the drain, the electron concentration gradually decreases to zero, and gradually turns to hole accumulation. Therefore, the drain current is superimposed by the drift of electrons (represented by black spheres) and holes (represented by white spheres) under the action of the drain voltage. Equation (4) is integrated by removing the absolute value and dividing it into two definition

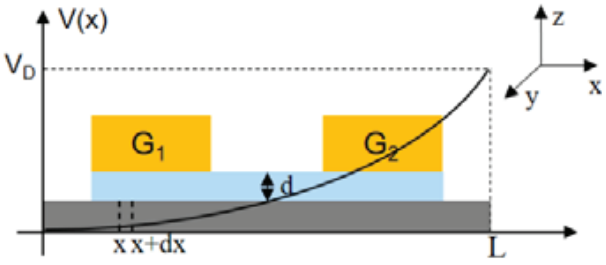

Fig. 4. Voltage distribution in the channel.

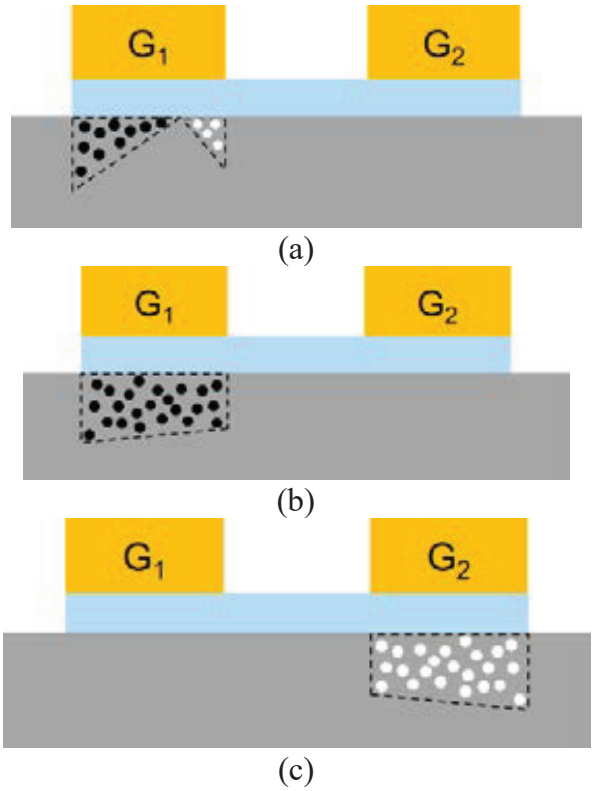

Fig. 5. Three carrier distributions for single gate applied pressure (a) 0<V_{G1}<V_D, V_{G2}=0 (b) V_{G1}>V_D, V_{G2}=0 (c) V_{G2}<0, V_{G1}=0.

domains:

$$I_D = \frac{W\mu_{n,p}}{L}C_{ox}\int_0^{V_D}|V_G - V(x)|\,dV$$
$$= \frac{WC_{ox}}{L}\left(\mu_n\int_0^{V_G}[V_G - V(x)]\,dV\right.$$
$$\left.+\mu_p\int_{V_G}^{V_D}[V(x) - V_G]\,dV\right) \quad (4)$$
$$= \frac{W}{2L}C_{ox}\left[\mu_n V_G^2 + \mu_p(V_G - V_D)^2\right].$$

In Fig. 5 (b), if the conditions $V_{G1} > V_D$ and V_{G2} = 0 are satisfied, the conducting carriers in the channel are mainly electrons, and the operating mechanism is primarily electron conduction when the voltage is applied at the drain. In Fig. 5 (c), if V_{G2}< 0, V_{G1} = 0, the conducting carriers in the channel are mainly holes, and the operating mechanism is primarily hole conduction:

$$I_D = \begin{cases} \frac{W}{2L}C_{ox}\left[\mu_n V_G^2 + \mu_p(V_G - V_D)^2\right] & 0 < V_{G1} < V_D, V_{G2} = 0 \\ \frac{W\mu_n}{L}C_{ox}\left(V_G V_D - \frac{V_D^2}{2}\right) & V_{G1} > V_D, V_{G2} = 0 \\ \frac{W\mu_p}{L}C_{ox}\left(\frac{V_D^2}{2} - V_G V_D\right) & V_{G2} < 0,\ V_{G1} = 0 \end{cases}. \quad (5)$$

As shown in Fig. 6 (a), when positive and negative voltages of the same magnitude are applied to the two

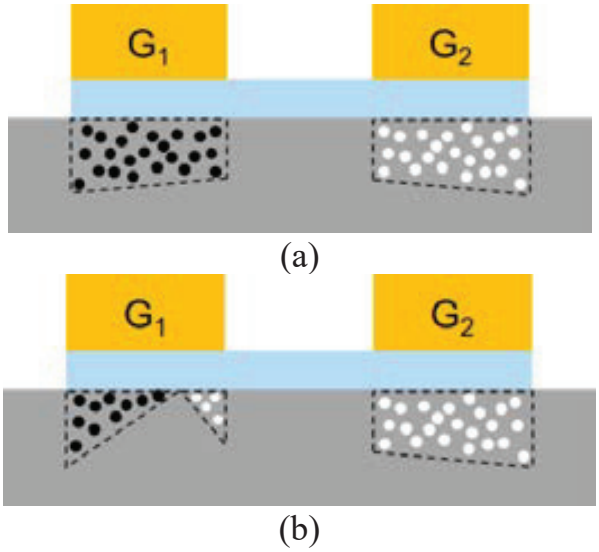

Fig. 6. Two carrier distributions for double gate applied pressure. (a) $V_G|>V_D$. (b) $0<|V_G|<V_D$.

top gates, and the absolute value of the gate voltage is greater than the drain voltage, electrons accumulate in the positive gate voltage region and holes accumulate in the negative gate voltage region. As shown in Fig. 6 (b), when positive and negative voltages of the same magnitude are applied to the two top gates, and the absolute value of the gate voltage is smaller than the drain voltage, electrons accumulate under the positive gate voltage region near the source. In contrast, holes accumulate under the positive gate voltage region near the drain and the negative gate voltage region. Referring to equation (4), the case is divided into two definition domains, and the integration is obtained as follows.

The channel resistance of each segment dR is

$$dR = \frac{dx}{gL} = \left(\frac{1}{W\mu_n |Q_n(x)|} + \frac{1}{W\mu_p |Q_p(x)|} \right) dx. \quad (6)$$

The formula for I_D is

$$I_D = \frac{gLdV}{dx} = \frac{W}{L} \int_0^{V_D} \left| \frac{\mu_n \mu_p |Q_n(x)| |Q_p(x)|}{\mu_p |Q_p(x)| + \mu_n |Q_n(x)|} \right| dV. \quad (7)$$

We get:

$$I_D = \begin{cases} t\frac{k}{1-k}\left(V_G V_D - \frac{V_D^2}{2}\right) & , \quad |V_G| > V_D \\ \frac{t}{2} \cdot \frac{k}{1-k}\left[V_G^2 + (V_G - V_D)^2\right], & 0 < |V_G| < V_D, \end{cases} \quad (8)$$

where $t = W\mu_n C_{0x}/L$, k $=\mu_p/\mu_n$.

The device parameters are set as follows: ε=9(the dielectric layer material is Al_2O_3), W=400 μm, L=60 μm, μ_n=10000 $cm^2/V \cdot s$, μ_p=4000 $cm^2/V \cdot s$, ε_0=8.85*10^{-14}F/cm, d=40 nm

$$t = \frac{W}{L}\mu_n \frac{\varepsilon_0 \varepsilon}{d} \approx 13.3 mA/V^2, k = \frac{\mu_p}{\mu_n} = 0.4. \quad (9)$$

By bringing t and k into equations (5) and (8), the operating current can be calculated for different gate voltage and bias voltage conditions, and the current characteristics of the device are plotted by Matlab.

Calculations explain the working mechanism of the device. Figure 7 (a) shows the output characteristic curve of the device under the single gate applied voltage. Positive gate voltage induces graphene to form an n-type semiconductor, and electrons accumulate in the channel area. When the drain-source bias voltage is small, electrons move toward the channel anode direction, creating a drift current, corresponding to the first linear region in the figure. As V_D gradually increases to a critical value, the drift of holes in the channel cannot be neglected. It moves in the opposite direction of electrons, preventing the increase of current, corresponding to the saturation

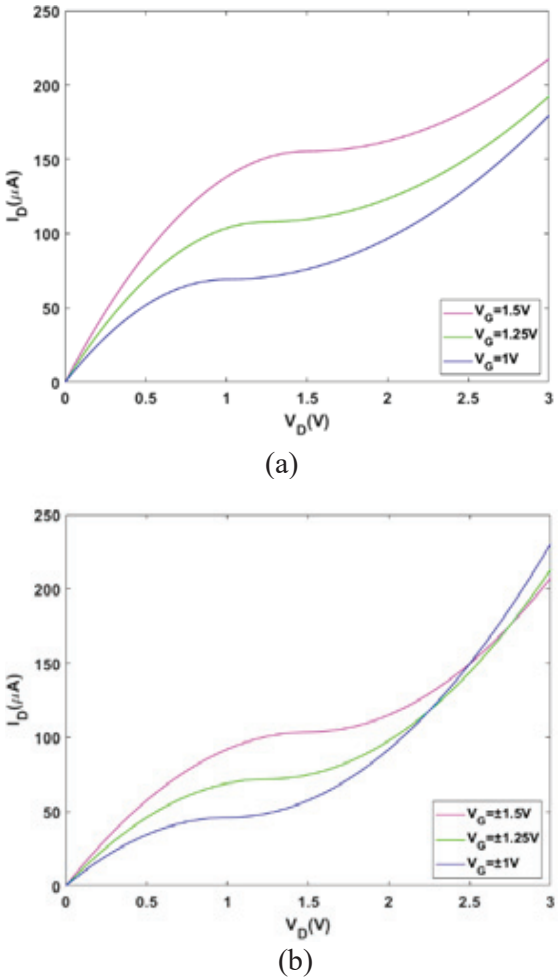

Fig. 7. I_D-V_D Output characteristic curve. (a) Single-gate applied voltage. (b) Double-gate applied voltage.

region in the figure. When V_D exceeds the critical value, the hole conductivity in the channel prevails, and the conductivity type of the channel changes from n-type to p-type, corresponding to the second linear region in the figure. Figure 7 (b) shows the output characteristic curve of the device under the double gate applied voltage, the positive gate pressure induces the accumulation of electrons in the graphene channel region, and the negative gate pressure induces the proliferation of holes in the graphene channel region, and the graphene p-n junction is formed in the channel region. When V_D is small, electrons move toward the positive pole, and holes move toward the negative. Because the electron mobility is much larger than the hole mobility, the channel still shows electron conduction. Still, the magnitude of the current is reduced compared to the single gate voltage, which reflects the weakening effect of the electric field built into the p-n junction on the drift current. Observe that a transient saturation region arises when the V_D gradually increases, and the conduction effects of electrons and holes are equivalent at this time; It is worth noting that when V_D increases to a certain level, a negative transconductance phenomenon occurs, indicating that the gate loses control of the current, which may be because a large gate voltage establishes a higher p-n junction barrier and suppresses the increase in output current.

According to equation (8), the parameters L and $k=\mu_p/\mu_n$ were also simulated to provide a reference for future improvements to the DG-GFET. Figure 8 (a) tells us that the channel length L should be reduced as much as the process can achieve. Figure 8 (b) illustrates that when considering graphene doping, increasing the k value helps to improve the performance of the device

IV. DEVICE FABRICATION AND TESTING OF DEVICE

The device is observed under a 30 times microscope, as shown in, as shown in Fig. 9, and four gold wires are connected to the device's drain, source, and gate pins. The overall fabrication flow of the device is shown in Fig. 10, here are the details [20, 21]:

(1) Obtain monolayer graphene by thermal decomposition of 4H-SiC under low pressure and high-temperature environment using the epitaxial growth method.
(2) Cutting off the excess part of graphene, leaving only the graphene layer in the target region.
(3) Fabrication of leaky and source metal electrodes with Ti/Au material, mainly with process steps of gluing, exposure, development, metal deposition, and exfoliation.

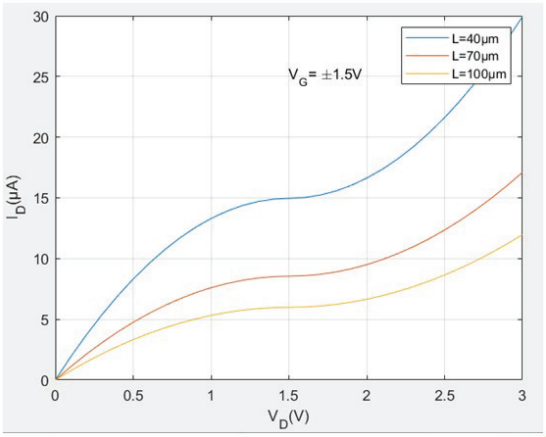

(a)

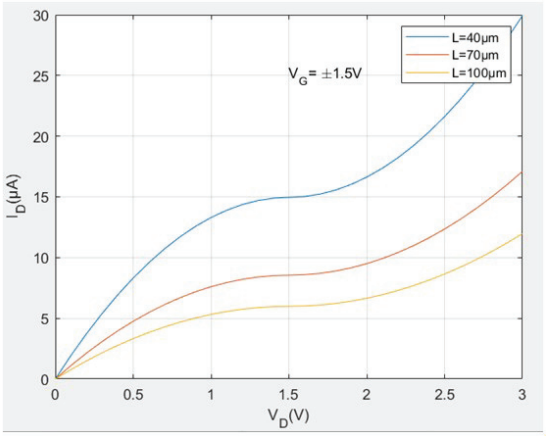

(b)

Fig. 8. I_D-V_D Double gate output characteristic curve under, (a) different channel lengths L, and (b) different k.

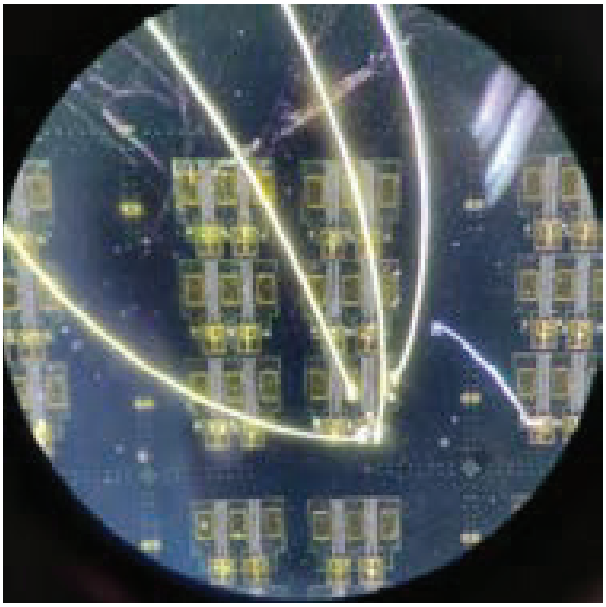

Fig. 9. Physical view of the device under a 30× microscope.

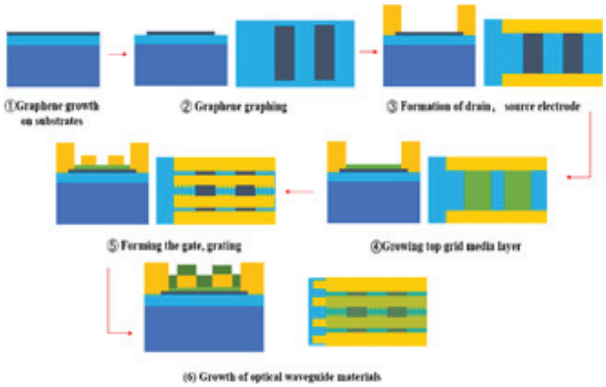

Fig. 10. DBR-DG-GFET fabrication steps.

(4) Deposition of Al_2O_3 media on graphene by atomic layer deposition (ALD), the ALD process allows precise control of the deposition thickness and high quality with fewer impurities.

(5) Growing two top gates with the same Ti/Au material, same steps as (3), it should be noted that the grating is attached to the gate and the size is small, requiring high precision, so a high level of the fabrication process is required.

(6) Deposition of waveguide material SiNx using plasma-enhanced chemical vapor deposition (PECVD) as the cavity material of the resonant cavity and coating on the device output port to improve the device output efficiency.

The potential difference between the gate and graphene determines the density of the two carriers in the device channel and whether the conducting type is electrons or holes. A sizeable forward gate voltage leads to the accumulation of electrons in graphene to produce an n-type channel. A sizeable reverse gate voltage leads to the accumulation of holes in graphene to build a p-type channel. This feature forms two branches separated by a Dirac point. After fabrication, electrical tests were performed on the double-top gate GFET. To obtain its transfer characteristic curve, the gate voltage V_{G1}= -3V-3 V, V_{G2}=0 V, and the drain-source V_D were 0.1 V and 0.2 V, respectively, to get its transfer characteristic curve, as shown in Fig. 11. The Dirac point of the intrinsic graphene is located at 0 V, and a bipolar curve shifted to the right is obtained because the substrate is heavily doped silicon, and the Dirac point is situated near 1.8 V, indicating that the graphene channel is P-type doped.

To eliminate the effect of graphene P-type doping, the value of the applied positive gate voltage needs to be greater than the Dirac point so that N-type graphene can be induced below this gate, thus forming a p-n junction. The output characteristics are tested by applying an appropriate forward drain voltage. Let V_{G2} be 1 V and V_{G1} be 3 V, 4 V, 5 V, and 6 V, and try the output characteristic curve of the device at the drain-source voltage V_D from 0 to 5 V Results are shown in Fig. 12.

Based on the results, when no gate voltage is applied, i.e., V_{G1}=V_{G2}=0 V, the graphene in the channel region is a good conductor, and the V-I curve is linear, as shown by the dashed line in Fig. 12. If there is no drain voltage, i.e., V_D=0, the p-n junction is in equilibrium, the current is zero, and the balance is broken after the drain bias is applied; When V_D gradually increases to the critical point of the p-n junction barrier, the growth trend of current turns; When V_D exceeds the breakdown point of the p-n junction barrier, the current increases significantly and enters into another linear growth region. It is worth mentioning that when V_D increases to a certain degree a negative transconductance phenomenon appears, which is due to the large gate voltage establishing a higher p-n junction barrier, resulting in a lag in the growth turning point of output current. Overall, the experimental results demonstrate that applying an external bias voltage to the double-top gate device effectively induces graphene to form a p-n junction.

V. RESULTS AND DISCUSSION

This paper designs and fabricates a graphene p-n junction device with a double-top gate structure. Comparing experimental test data versus simulation results, the default channel in simulation is pure graphene. The Dirac point is located at 0 V The gate voltage injection is positive and negative with equivalent absolute values. The actual device has a Dirac point shift in the graphene leading to a difference in the gate voltage setting. The measured data are consistent with the simu-

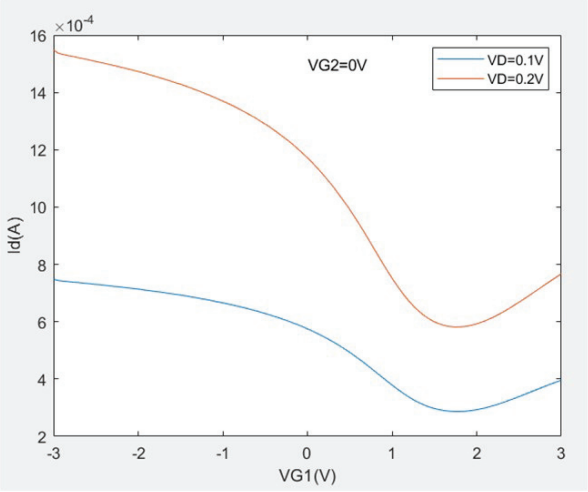

Fig. 11. Transfer characteristic test curve.

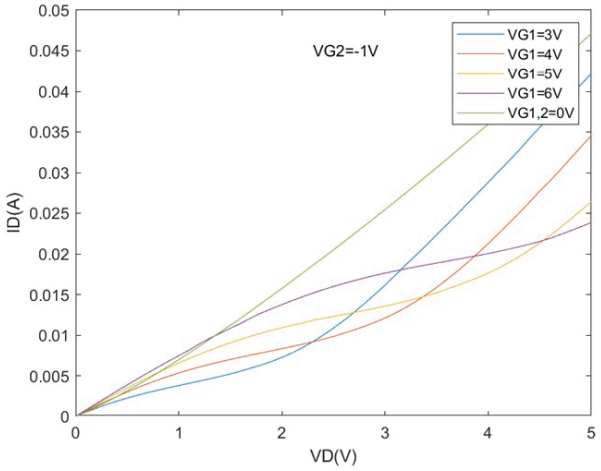

Fig. 12. Output characteristics test curve.

lation results. When the injected bias voltage is small, larger the gate voltage causes the graphene channel to accumulate more non-equilibrium carriers, at which time the current operating increases linearly with the rise of the gate voltage; when the bias voltage is raised to the critical point of breaking through the p-n junction barrier, the trend of current growth turns; When the bias voltage reaches the p-n junction barrier-breaking point, the current starts to increase significantly and enters into the faster linear growth region. A large gate voltage will increase the barrier height of the p-n junction to a certain extent, and the negative transconductance phenomenon appears, which suppresses the continuous increase of the current. Since simulation parameters are less accurate than in perfect theoretical conditions, there are some numerical errors, but overall the model is quite reliable.

ACKNOWLEDGMENT

This work is supported by National Natural Science Fund (61871442), Ministries Fund (6142601200504, 2020-JCJQ-JJ-3 97) funding.

REFERENCES

[1] S. Masuminia, C. Ghobadi, J. Nourinia, M. Karamirad, and B. Mohammadi, "A novel tunable graphene based terahertz absorber with polarization insensitive," *Applied Computational Electromagnetics Society (ACES) Journal*, vol. 31, no. 12, pp. 1439-1444, 2021.

[2] B. Beiranvand and A. S. Sobolev, "A proposal for a multi-functional tunable dual-band plasmonic absorber consisting of a periodic array of elliptical grooves," *J. Opt*., vol. 22, Art. no. 105005, 2020.

[3] B. Beiranvand, A. S. Sobolev, and A. Sheikhaleh, "A proposal for a dual-band tunable plasmonic absorber using concentric-rings resonators and monolayer graphene," *Optik*, vol. 223, Art. no. 165587, 2020.

[4] V. Kumar, "24 GHz graphene patch antenna array," *Applied Computational Electromagnetics Society (ACES) Journal*, vol. 34, no. 5, pp. 676-683, 2019.

[5] S.-l. Wang, J.-S. Hong, Y. D., and Z.-j. Chen, "A frequency reconfigurable antenna based on few layer graphene," *Applied Computational Electromagnetics Society (ACES) Journal*, vol. 36, no. 5, pp. 542-547, 2021.

[6] R. Bala, R. Singh, A. Marwaha, and S. Marwaha, "Wearable graphene based curved patch antenna for medical telemetry applications," *Applied Computational Electromagnetics Society (ACES) Journal*, vol. 31, no. 5, pp. 543-550, 2021.

[7] R. Sordan, F. Traversi, and V. Russo, "Logic gates with a single graphene transistor," *Appl. Phys. Lett*., vol. 94, Art. no. 073305, 2009. Available: https://doi.org/10.1063/ 1.3079663.

[8] A. Das, S. Pisana, B. Chakraborty, S. Piscanec, S. K. Saha, U. V. Waghmare, K. S. Novoselov, H. R. Krishnamurthy, A. K. Geim, A. C. Ferrari, and A. K. Sood, "Monitoring dopants by Raman scattering in an electrochemically top-gated graphene transistor," *Nat. Nanotech*, vol. 3, pp. 210-215, 2008.

[9] P. Weis, J. L. Garcia-Pomar, M. Höh, B. Reinhard, A. Brodyanski, and M. Rahm, "Spectrally wideband terahertz wave modulator based on optically tuned graphene," *ACS Nano*, vol. 6, no. 10, pp. 9118-9124, 2012.

[10] I. Maeng, S. Lim, S. J. Chae, Y. H. Lee, H. Choi, and J.-H. Son, "Gate-controlled nonlinear conductivity of Dirac Fermion in graphene field-effect transistors measured by terahertz time-domain spectroscopy," *Nano Lett.*, vol. 12, no. 2, pp. 551-555, 2012.

[11] L. Valentini, J. M. Kenny, F. Alimenti, and L. Roselli, "Planar MOSFET devices on paper substrate using graphene oxide film as gate dielectric," in *Proc. 2013 European Microwave Conference*, pp. 5-8, 2013. doi: 10.23919/EuMC.2013.6686576.

[12] J. S. Moon, D. Curtis, S. Bui, T. Marshall, D. Wheeler, I. Valles, S. Kim, E. Wang, X. Weng, and M. Fanton, "Top-gated graphene field-effect transistors using graphene on Si (111) wafers [J]," *IEEE Electron. Device Lett.*, vol. 31, no. 11, pp. 1193-1195, 2010.

[13] J. S. Moon, D. Curtis, M. Hu, D. Wong, C. Mcguire, P. Campbell, G. Jernigan, J. Tedesco, B. VanMil, R. Myers, Jr. Eddy, and D. K. Gaskill, "Epitaxial-graphene RF field-effect transistors on

Si-face 6H-SiC substrates," *IEEE Electron. Device Lett.*, vol. 30, no. 6, pp. 650-652, 2009.

[14] K. Tamersit, "An ultra-sensitive gas nanosensor based on asymmetric dual-gate graphene nanoribbon field-effect transistor: Proposal and investigation," *J. Comput. Electron.*, vol. 18, no. 3, pp. 846-855, 2019.

[15] J. P. Liu, S. Safavi-Naeini, and D. Ban, "Fabrication and measurement of graphene p–n junction with two top gates," *Electron. Lett.*, vol. 50, no. 23, pp. 1724-1726, 2014.

[16] J. Sarker and A. Shifat, "An analytical approach for modeling of a top gated graphene based MOSFET[C]," in *Proc. Int. Conf. Comput. Inform. Technol.*, IEEE, 2017.

[17] S. Bardhan, M. Sahoo, and H. Rahaman, "Empirical drain current model of graphene field-effect transistor for application as a circuit simulation tool," *IETE J. Res.*, no. 3, pp. 1-13, 2019.

[18] M. Weis, "Gradual channel approximation models for organic field-effect transistors: The spacecharge field effect," *J. App. Phys.*, vol. 111, Art. no. 054506, 2012.

[19] B. Su, J. Huang, and J. Liu, "Current characteristics of double-top-gated graphene field effect transistor," in *Proc. 2021 IEEE 4th Int. Conf. Autom. Electron. Electr. Eng. (AUTEEE)*, Shenyang, China, Nov. 19-21, pp. 264-267, 2021.

[20] A. Greene, S. Madisetti, P. Nagaiah, V. Tokranov, M. Yakimov, R. Moore, and S. Oktyabrsky, "InGaSb MOSFET channel on metamorphic buffer: Materials, interfaces and process options," in *Proc. 223th ECS Meeting*, 2013.

[21] P. D. Ye, A. T. Neal, T. Shen, J. J. Gu, M. L. Bolen, and M. A. Capano, "Atomic-layer-deposited high-k dielectric integration on epitaxial graphene," *ECS Trans.,* vol. 33, no. 3, pp. 459-466, 2010.

Jinbao Huang born in 1999, a native of Luan, Anhui Province, China.

He is a master's student at the School of Electronic and Optical Engineering, Nanjing University of Science and Technology. His main research interests are terahertz devices.

Yun Wu works in Science and Technology on Monolithic Integrated Circuits and Modules Laboratory, Nanjing Electronic Device Institute. His main research interests are terahertz devices.

Bo Su born in 1997, a native of Xi'an, China.

He got his master's degree in Optical Engineering from Nanjing University of Science and Technology. His main research interests are terahertz devices.

Jingping Liu School of Electronic and Optical Engineering, Nanjing University of Science and Technology, Nanjing, People's Republic of China

Her main research areas are antenna design, signal reception, processing, electronic countermeasure technology, and terahertz devices.

Multiple Frequencies Five-Port Reflectometer (FPR) for Pure and Adulterated Honeys

E. M. Cheng[1,2*], A. B. Shahriman[1,3], K. Y. Lee[4], S. F. Khor[5], N. F. Mohd Nasir[1,6], S. A. Baharuddin[7], C. W. S. Robiah Mohamad[1], and E. Z. Mohd Tarmizi[8]

[1]Faculty of Electronic Engineering & Technology
Universiti Malaysia Perlis, Arau, 02600, Perlis, Malaysia
emcheng@unimap.edu.my, shahriman@unimap.edu.my, nashrul@unimap.edu.my,
robiah@unimap.edu.my

[2]Centre of Excellence for Advanced Communication Engineering (ACE)
Universiti Malaysia Perlis, Arau, 02600, Perlis, Malaysia

[3]Centre of Excellence for Automotive & Motorsport Technology (MOTECH)
Universiti Malaysia Perlis, Arau, 02600, Perlis, Malaysia

[4]Lee Kong Chian Faculty of Engineering & Science, Tunku Abdul Rahman University
Sungai Long Campus, Jalan Sungai Long, Sungai Long City, Cheras, 43000 Kajang, Selangor, Malaysia
kylee@utar.edu.my

[5]Faculty of Electrical Engineering & Technology
Universiti Malaysia Perlis (UniMAP), Perlis, Malaysia
sfkhor@unimap.edu.my

[6]Centre of Excellence for Sport Engineering (SERC)
Universiti Malaysia Perlis, Arau, 02600, Perlis, Malaysia

[7]Department of Process and Food Engineering, Faculty of Engineering
Universiti Putra Malaysia UPM, 43400, Serdang, Selangor, Malaysia
sitiaishah1108@gmail.com

[8]Centre of Foundation Studies for Agricultural Science
Universiti Putra Malaysia UPM, 43400, Serdang, Selangor, Malaysia
emma@upm.edu.my

Abstract – Honey adulteration is one of the major health concerns among honey consumers, it is essential to inspect the quality of honey. One of the methods is to characterize the honey by using the microwave reflection technique. A Five-Port Reflectometer (FPR) is proposed in this work. The microstrip Five-Port ring junction circuit was designed for multiple frequencies of 0.60 GHz, 2.28 GHz, and 3.47 GHz. The fabricated circuit works with an analogue-digital converter, open-ended coaxial sensor, diode detectors and computer to form a complete FPR measurement system. The reflection measurements were conducted on Honey Gold and Trigona Honey for multiple frequencies. The performance of the FPR in s-parameter measurement was verified by Vector Network Analyzer (VNA). This study shown that the performance of FPR in term of reflection measurement has promising accuracy which is comparable with VNA. The FPR can be used as an alternative instrumentation system for characterizing pure and adulterated honey.

Index Terms – Dielectric, honey, reflectometer, reflection, sensor.

I. INTRODUCTION

Honey is sweet, viscous and nutrient-rich that produced by bees from nectar of plants or honeydew [1]. It can be used for the treatment of burn wounds and ulcers [2]. However, honey is overprice due to its health giving properties and market demand. At the same time, honey adulteration is a major issue in the honey's industry.

Submitted On: March 9, 2022
Accepted On: July 16, 2022

https://doi.org/10.13052/2022.ACES.J.370705

This is because only pure honey able to provide anti-inflammatory and antifungal properties that leads to precious medicinal values [3].

Conventionally, honey quality is measured by human sensory method via color, viscosity, smell, and flavor [4]. However, the human sensory method is not scientific as it is dependent on subjective judgement that based on experience of an individual. On the other hand, chemical analyses, e.g. chromatography [5], high performance liquid chromatography [6] and mass spectrometry [7] were used to characterize the honey. The chemical analyses require high performance of instruments, time-consuming and high skilled procedures that limit the measurement in laboratory.

In recent years, microwave technique is widely uses in characterizing material such as food and agricultural products. The technique is a non-destructive, simple and fast processing method that based on the reflection measurement. On the other hand, the measurement technique can be easily adapted by an enhanced measurement setup that improve the effectiveness of material characterization measurement [8]. Food properties can be considered as a major contributing factor to describe the reflection between microwaves and food products [9] which depict the storage and dissipation of electromagnetic energy [10]. There are plants, foods and agricultural products have been investigated in past works that are associated with electrical characterization, e.g. sea cucumber [11], corn flour [12], peanut kernels [13], oil palm fruit [14, 15], vegetation [16], agri-food [17] and etc. Based on the studies, electrical properties of food are dependent on the moisture, frequency, temperature, density and the physical state of a food [18]. The dielectric characterization had achieved a great success in the food technology and agricultural industry which can be associated with the behaviour of food material. Hence, honey characterization by using the microwave reflection measurement has a great development potential for instrumentation system.

II. MATERIALS AND METHODS

A. Development of five-port reflectometer (FPR)

The principle of Five Port Reflectometer (FPR) was introduced by Riblet and Hansson [20] in 1983 based on the origin of Six-Port which proposed by Engen in 1977 [19]. The FPR is a low cost and portable alternative to VNA. It simplifies the circuitry by eliminating one of the ports in Six-Port which used to detect the power of input signal. The FPR is feasible when the connected signal source performs stable [21]. In the FPR, three detection ports are connected to diode detectors, while another two ports are connected to power source and sensing port, respectively. In a five-port algorithm [20], it requires reflection coefficients (in magnitude) agree with $|S11| = |S22| = |S33| = |S44| = |S55| \approx 0$. In addition, the transmission coefficients (in magnitude) need to agree with $|S21| = |S32| = |S43| = |S54| = |S15| = |S12| = |S23| = |S34| = |S45| = |S51| = |S31| = |S42| = |S53| = |S14| = |S25| = |S13| = |S24| = |S35| = |S11| = |S52| \approx 0.5$. All these requirements must be complied for optimum performance of FPR. Apart from that, the phase difference between each port must be approximately 120° or -120° ($+240^\circ$).

The FPR's circuit consists of five ports which can be designed by using a symmetrical Five-Port ring junction circuit. The computational electromagnetics techniques play an indispensable role in the realms of electronics design and optimisation [22]. Some numerical simulation technologies are required as well to guarantee its features especially in solving large-scale Maxwell's equations [23]. In this work, a multiple frequencies Five-Port ring junction circuit was designed and simulated using AWR Microwave Office (MWO) in accordance the Riblet and Hansson theory. The compliance of the circuit performance was verified by reducing the mismatch error between the component parts through the simulation in MWO. The optimum length, radius corner and width for the components of ring junction were determined for a compactness of size.

The simulated circuit consists of the components of single microstrip transmission line, T-junction, bending and radius corner microstrip line. The dimensions of the circuit are tabulated in Table 1 where the length1 (L1), length2 (L2), length (L3), radius 1 (R1), radius 2 (R2) and width (W) are in the unit of μm. The layout is as illustrated in Fig. 1 (a) with a special bending designed to minimise the size of the five-port circuit. The dielectric substrate used in this design is Rogers RO3003 high frequency laminates (dielectric constant, εr = 3; thickness of substrate = 1.52 mm; thickness of copper cladding = 35 μm). It is a ceramic-filled PTFE composites for use in printed circuit boards in commercial microwave and RF applications. The schematic diagram of ring junction circuit in MWO is shown in Fig. 1 (b). This circuit layout is able to meet the requirements of Riblet and Hansson Theory for frequency up to 3.5 GHz with multiple frequency features. Operating frequencies

Table 1: Dimension of circuit

Parameters	Specification (μm)
Length 1, L1	8700
Length 2, L2	2070
Length 3, L3	1280
Radius 1, R1	7600
Radius 2, R2	7000
Width, W	4500

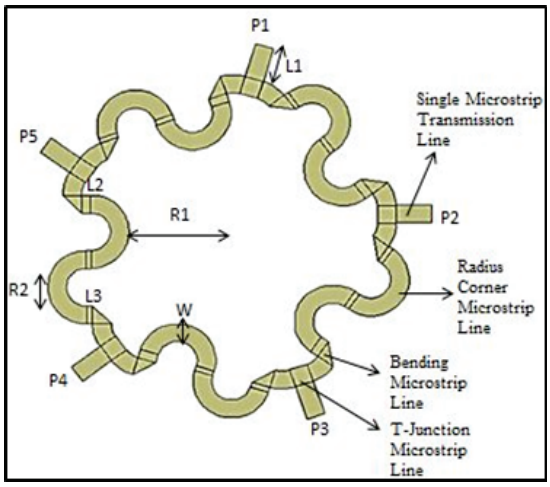

(a)

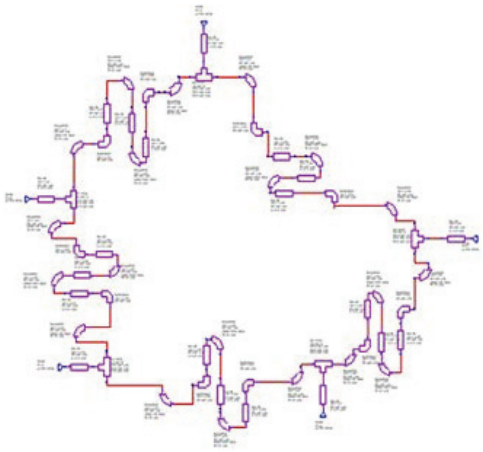

(b)

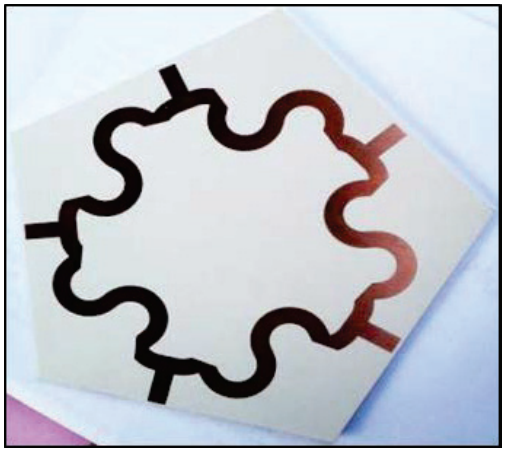

(c)

Fig. 1. Design and simulation of five-port ring junction circuit. (a) Circuit layout, (b) schematic diagram, and (c) fabricated circuit.

for the designed circuit are 0.60 GHz, 2.28 GHz, and 3.47 GHz. These three frequencies have been selected based on the minimum error observed in the simulated result. Other frequency band can be designed by adjusting the dimensions of the components in the circuit. Five-Port ring junction circuit was fabricated as illustrated in the Fig. 1 (c). The performance of fabricated circuit was validated using VNA to ensure it has good agreement with the requirements that stipulated in Riblet and Hansson theory.

The reflection coefficient, Γ and the signal detected at each detection port, qi can be expressed in complex form as $\Gamma = u + jv$ and $q_i = x_i + jy_i$ respectively. Meanwhile, $w_i = \sqrt{P_i/k_i}$(i = 1, 2, 3) is in the real forms where ki is calibration constant and pi is emerging power detected at specific port (i = 1, 2, 3). The reflection coefficient can be determined by solving the eqn (1) using the power detected from each port, i.e. P1, P2, and P3. Meanwhile, k1,k2,k3,x1,x2,x3,y1,y2,y3 are the values which determined through the calibration procedure.

$$\begin{pmatrix} \frac{P_1}{k_1} - \frac{P_2}{k_2} - x_1^2 + x_2^2 - y_1^2 + y_2^2 \\ \frac{P_2}{k_2} - \frac{P_3}{k_3} - x_2^2 + x_3^2 - y_2^2 + y_3^2 \end{pmatrix} = \begin{pmatrix} u \\ v \end{pmatrix}^T \begin{pmatrix} (-2x_1 + 2x_2) + (-2y_1 + 2y_2) \\ (-2x_2 + 2x_3) + (-2y_2 + 2y_3) \end{pmatrix}. \quad (1)$$

A Graphical User Interface (GUI) program is developed by using the Agilent VEE Pro 6.0. The GUI program has three modules, i.e., save calibration (save cal), calibration and measurement. Figure 2 shows the panel view of the GUI program. The save calibration section was used to save the measured data of the selected calibration standards in calibration section. The calibration procedures are completed when the GUI programming is performed the correction of the measurement setup via measured calibration standards data. This includes the compute of unknown constants of Five-Port calibration equations. The computed constants are to be used for the computation of complex reflection coefficient in the measurement. Calibration needs to be conducted prior to reflection measurement which it is needed to remove the systematic error.

The module of measurement can be used after the calibration is completely conducted. The measurement to determine the complex reflection coefficient, Γ of material under test (honeys) in magnitude and phase as well as in real and imaginary form can be conducted and controlled by using the ON/OFF Button on the panel of the GUI program.

Generally, the measurement setup of the FPR consists of a computer (with a GUI program), microstrip Five-Port ring junction, three Keysight diode detectors, Mini Circuit microwave signal generator, open-ended coaxial sensor and PICO analogue-digital converter

(ADC). The input port of microstrip Five-Port ring junction is supplied with the microwave signal source. The test port is connecting to an open-ended coaxial sensor. Meanwhile, the other three ports are connected with diode detectors to detect and convert the reflected field strength to be in an electrical voltage form. The detected analog voltages are then be further transform into a digital signal by PICO ADC. The developed GUI program is used to acquire data, conduct computation of Five-Port algorithm and calculation of reflection coefficient. Figure 3 illustrates the complete measurement setup of FPR. The emerging wave due to interaction of incident and reflected waves are distributed in each of power detecting ports in five-port circuit. Variation in reflection coefficient, Γ at test port which connects with open-ended coaxial sensor attributed to different reflected wave at power detectingport due to electrical discontinuity occur during reflection measurement.

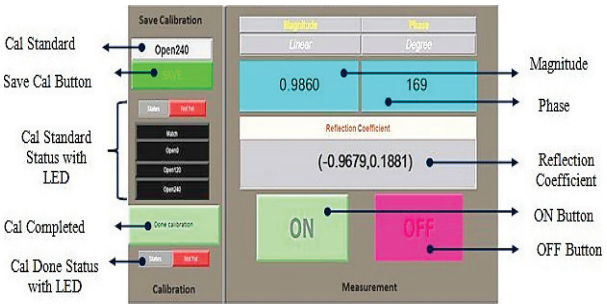

Fig. 2. Panel view of Graphical User Interface.

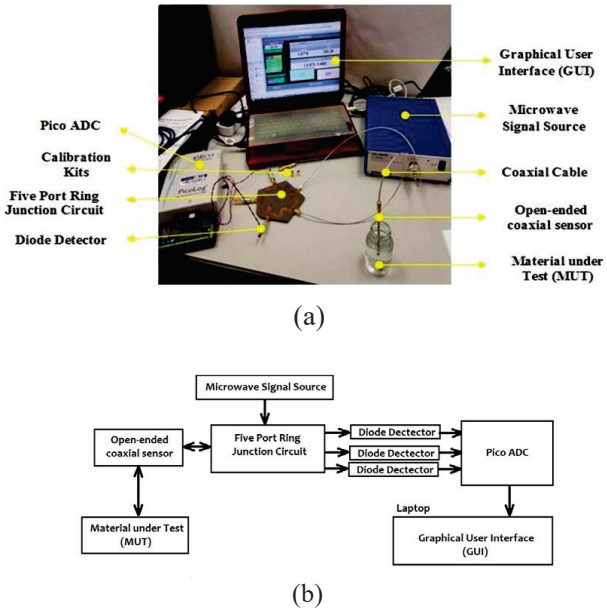

Fig. 3. The Five-Port Reflectometer (FPR) (a) Measurement Setup, (b) Measurement diagram.

B. Sample preparation

Two types of pure honey are used, i.e., pure Honey Gold ('Lebah Asli') and pure Trigona Honey('Kelulut') as shown in Fig. 4. Both honeys are obtained commercially from the Harmony Bee Farm, which is located in Perlis state, Malaysia. The selected honey samples are based on the market demand and issue of adulteration in the honey's industry. In this work, these honeys act as representatives in general to study the behaviour and characterization of adulterated honey sample. The initial water content for both honeys, i.e., pure Honey and pure Trigona Honey is 18% and 35%, respectively. The water content was measured through standard oven drying method [24]. In this method, sample of honey is poured evenly on a petri dish and the weight were measured using a precision balance. It was heated in the oven at 40°C for 1 hour. Afterward, the weight of sample was measured again. The process is repeatedly until the difference between successive heated sample is insignificant in term of weight. The initial water content of honey is then calculated using wet basic formula as follows:

$$\text{Water content in honey} = \frac{(\text{Weight before dry} - \text{weight after dry})}{\text{Weight before dry}} \text{ x } 100. \quad (2)$$

In this work, water adulterated and sucrose adulterated honey were prepared as sample under test. The major composition in Honey Gold and Trigona Honey is sucrose, fructose and glucose. However, the fructose and glucose have higher nutrition value than sucrose.

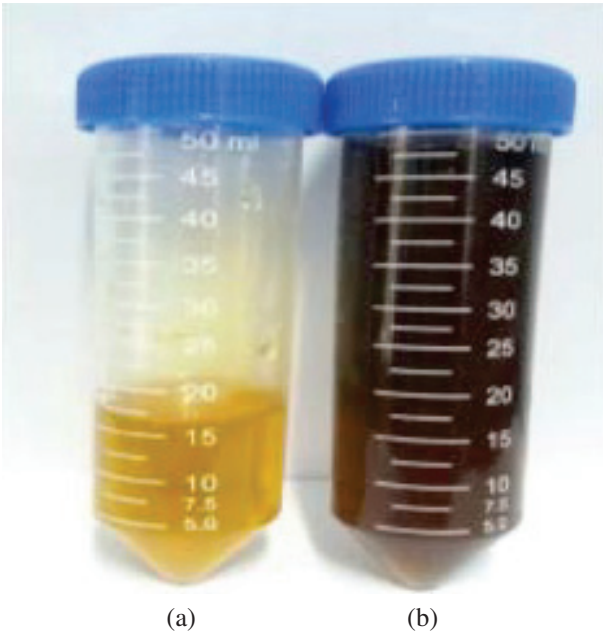

Fig. 4. Pure honey samples: (a) Honey Gold and (b) Trigona Honey.

In addition, sucrose is cheap in cost. As a result, sucrose is being used frequently in honey adulteration. It is very common in food industry. Sucrose can cause severe hazard to diabetic patient. Sucrose is out of the range of acceptable Glycemic Index (GI) where GI is a measure of impact of blood glucose on an individual [30].

For preparation of water adulteration sample, a 5 ml of Honey Gold or Trigona Honey was kept in centrifugal tube with a constant amount. The water was added for a variation of sample based in the determination of water content on the weight ratio percentage (% wt/wt). It is expressed as [25].

$$\text{Water content}(\%) = \frac{\mathrm{M_a} \times (\mathrm{Wi}) + \mathrm{M_b}}{\mathrm{M_a} + \mathrm{M_b}} \times 100, \qquad (3)$$

where

M_a = Mass of 5ml of honey which equivalent to 7g

M_b = Mass of distilled (deionized) water (1ml of distilled water =1g)

Wi = Initial water content (%) of both pure honey samples

In this work, distilled water with known amount is mixed with each honey sample. The weight of distilled water and honeys were measured. The water adulterated honey samples were prepared at room temperature.

On the other hand, the sucrose adulteration sample is prepared and studied. Each centrifugal tube is filled in with a 5ml for different honey samples by using the syringe (5ml). The sucrose syrup was prepared with various ratio, i.e., at ratio of 1:1 (20g of sucrose powder: 20g of distilled water) [26]. The sample with 100% indicates the pure sucrose syrup which acts as a control reference. The ratio of sucrose syrup were prepared by using the weight ratio percentage concentration by weight. The determination is expressed as

$$\text{Weight ratio percentage}\,(\mathrm{wt/wt}) = \frac{\text{Mass of solute(g)}}{\text{Mass of solvent(g)}} \times 100, \qquad (4)$$

where mass of solute is sucrose powder while the mass of solvent is deionized distilled water. The ratio of sucrose syrup is within 10% to 100% and to be mixed with pure honey samples (0%). To achieved homogeneity and dilution of the honey-sucrose mixture samples prior to measurements, the samples were soaked in a water bath at 35°C for at least 20 minutes All the measurement and samples were measured at room temperature.

III. RESULTS and DISCUSSIONS

A. Validation of five-port ring junction circuit

The simulated and measured S-Parameters for Five-Port ring junction are validated and tabulated in Table 2. The five ports ring junction circuit has three operating frequencies, i.e., 0.60 GHz, 2.28 GHz and 3.47 GHz. The simulated S-parameters at all three frequencies have a good agreement with theoretical result of less than less than 0.01 and 1.00° in magnitude and phase, respectively. At the same time, all three frequencies exhibit good agreement as indicated in Table 2. The performance of S-parameters of fabricated circuits was verified using a commercial Network Analyzer, Agilent E8362B PNA. It compares with simulated S-parameters through AWR Microwave Office. Absolute error of magnitude and phase of S-parameters through this comparison is less than 0.1 and 7°, respectively.

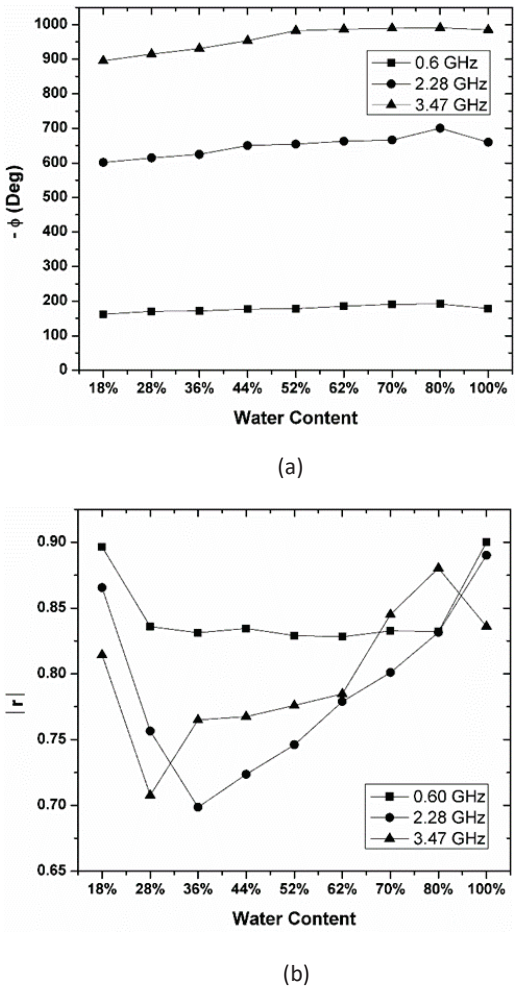

Fig. 5. The variation of (a) magnitude ($|\Gamma|$), and (b) negative phase ($-\varphi$) of reflection coefficient over water content with various frequencies for Honey Gold.

Table 2: Comparison between measured and simulated S-parameter (S) in (a) magnitude, $|\Gamma|$ and (b) phase, φ with various frequency (f)

(a)

f (GHz)	S (Mag)	Measure	Simulate	Absolute Error
0.60	$\|S_{11}\|$	0.1007	0.0092	0.0915
	$\|S_{21}\|$	0.4443	0.4933	0.0503
	$\|S_{31}\|$	0.5358	0.5066	0.0292
	$\|S_{41}\|$	0.5339	0.5066	0.0273
	$\|S_{51}\|$	0.4428	0.4933	0.0505
2.28	$\|S_{11}\|$	0.0546	0.0122	0.0668
	$\|S_{21}\|$	0.4771	0.5074	0.0303
	$\|S_{31}\|$	0.4744	0.4924	0.0161
	$\|S_{41}\|$	0.4763	0.4924	0.0274
	$\|S_{51}\|$	0.4805	0.5074	0.0269
3.47	$\|S_{11}\|$	0.0146	0.0031	0.0115
	$\|S_{21}\|$	0.4504	0.5008	0.0504
	$\|S_{31}\|$	0.4409	0.4992	0.0583
	$\|S_{41}\|$	0.5061	0.4992	0.0069
	$\|S_{51}\|$	0.4876	0.5008	0.0132

(b)

f (GHz)	S (Phase)	Measure (°)	|Phase Difference| (Measured) (°)	Simulate (°)	Phase Difference (Simulated) (°)	Absolute Error of Phase Difference (°)
0.60	S_{21}	284	113	284	120	7.00
	S_{31}	171		164		
	S_{41}	170	113	284	120	7.00
	S_{51}	284		164		
2.28	S_{21}	357	242	353	239	3.00
	S_{31}	115		114		
	S_{41}	114	239	114	239	0.00
	S_{51}	353		353		
3.47	S_{21}	186	113	191	120	7.00
	S_{31}	73		71		
	S_{41}	77	117	71	120	3.00
	S_{51}	194		191		

B. Adulterated honey reflection coefficient measurement

From the observation of water adulterated honey measurements as illustrated in Figures 4 and 5, in average, the measured reflection coefficient magnitude, $|\Gamma|$ of the water adulterated honey sample is lower when the frequency is higher. This can be described by the complex reflection coefficient, Γ as express in the eqn (5),

$$\Gamma = \frac{Z_L - Z_0}{Z_L + Z_0}. \quad (5)$$

The Z_0 is the impedance of the coaxial line and open-ended coaxial sensor, while the load impedance, Z_L can be defined as mismatch impedance of the honey sample.

The variation of the water content in adulterated honey causes the mismatch impedance.

Prior to the measurement, the comparison of $|\Gamma|$ and φ through measurement of known loads indicate that absolute error of $|\Gamma|$ and φ is less than 0.07 and 9°, respectively for all the frequencies of interest [27]. Figure 4 (a) shows that the pure Honey Gold has 18% of water content and exhibit highest $|\Gamma|$ for frequency of 0.6 GHz and 2.28 GHz. The pure Honey Gold has lowest water content (18%) however leads to significant reflection. It is different from finding in Fig. 5 (a) where of water adulterated Trigona Honey exhibit the higher $|\Gamma|$ when the water content is increasing. It indicates that level of mismatch impedance is different for both water adulterated honeys at variation of water content

at different frequency band. It can be surmised that at 0.6 GHz, the reflection coefficient is decreases with the increasing of water content for both the pure Honey Gold and Trigona Honey. On the other hand, at 2.28 GHz and 3.47 GHz, the increases of water content leads to a drop of reflection coefficient and followed by a bounce back when the water content is increasing. This can be explained by the pure honey's molecule forming and interaction of sample mixture to the microwave signal. The additional of water molecule in honey might lead to the dispersion of fructose, sucrose and glucose molecule, as water is important to reduce viscosity of solution. The water breaks the behaviour of pure honey and lead to a higher reflection coefficient when the percentage of water in increasing. Both honeys has slightly difference behaviour were due to the properties of mineral in the honey, e.g., the pure Trigona Honey contenting a very high percentage of Calcium, Potassium, Sodium, Magnesium, Zinc and etc. [28]. These minerals decline the magnetic effect of a sample when more water content is added to diamagnetic substance [29].

Figures 4 (b) and 5 (b) show the variation of negative phase, $-\varphi$ over frequency for Honey Gold and Trigona Honey, respectively. The $-\varphi$ increase as water content increases for all frequency band. The increase of $-\varphi$ were contributed by the addition of water that has high complex permittivity. The increases of $-\varphi$ indicated that the significant delayed time of incident field and reflected field occurred. It also suggests that time delay is lengthened during polarization when frequency increases. This delay is due to process of polarization and friction. The dissipated field energy increases with frequency. Subsequently, time delay increases since the dissipation of energy involves mechanism of collision and friction. Increment of time delay increase lagging phase shift is shown by the $-\varphi$ in this work.

Apart from water, sucrose is another additive in honey adulteration. The sucrose adulterated honeys measurements are as illustrated in Figs. 6 and 7. The Figs. 6 (a) and 7 (a) shown that when the frequency increases, the $|\Gamma|$ decreases for both the Honey Gold and Trigona Honey samples. On the other hand, $|\Gamma|$ decreases when sucrose content increases. It can be noticed that pure honey exhibits slightly lower $|\Gamma|$ than sucrose adulterated samples. It implies that the discrepancy of capacitive impedance of pure honey from characteristic impedance of coaxial line is due to high inertia of bound fructose (180 grams/mol), water (18 grams/mol) and sucrose (342 grams/mol) molecules. It increases difficulty of bound molecules in polarization. Subsequently, it reduces the energy dissipation rate. When 10% sucrose content was used to adulterate honey, additional sucrose molecules is sufficient enough to present as free molecules and they can be

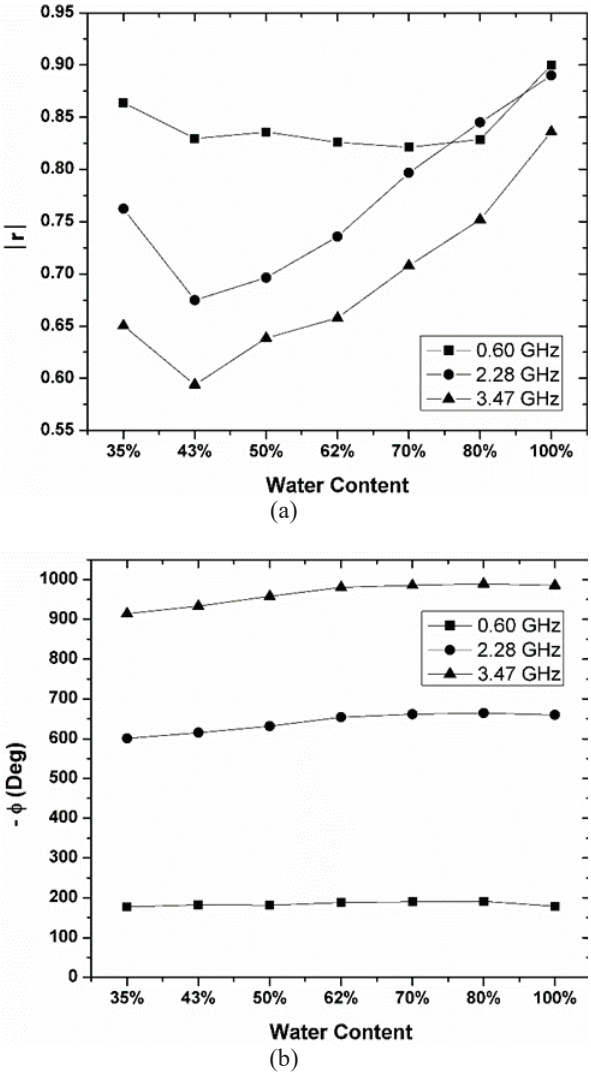

Fig. 6. The variation of (a) magnitude ($|\Gamma|$), and (b) negative phase ($-\varphi$) of reflection coefficient over water content with various frequencies for Trigona Honey.

polarized easily. As a result, $|\Gamma|$ of adulterated honey is higher than pure honey for sucrose content more than 10% for adulteration. Worth to mention that the $|\Gamma|$ of sucrose adulterated Trigona Honey with only 10% sucrose addition in adulteration could increase drastically to a higher level due to the mineral contents as explained previously. In addition, sucrose is a diamagnetic substance [31] which is similar to the water. It decreases magnetic effect of minerals in a sample under test.

Overall, the negative phase, $-\varphi$ of sucrose adulterated Honey Gold in Fig. 6 (b) and Trigona Honey in Fig. 7 (b) varies insignificantly when sucrose content increases. The sucrose is heavier than glucose, water and

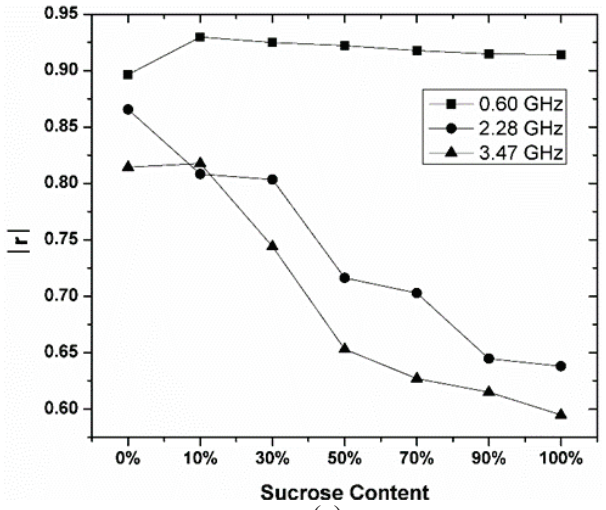

(a)

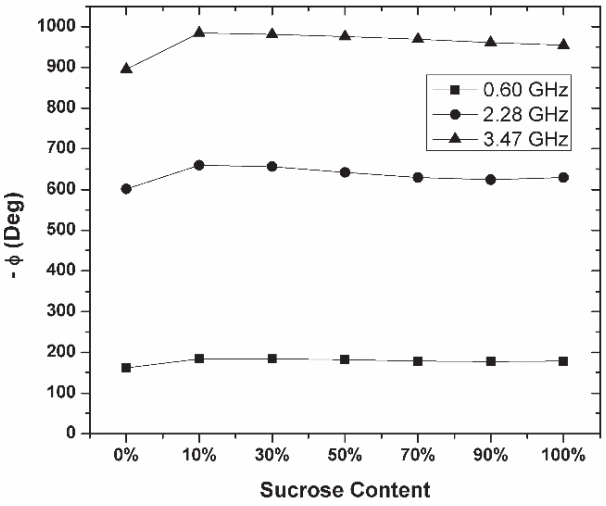

(b)

Fig. 7. The variation of (a) magnitude ($|\Gamma|$), and (b) negative phase ($-\varphi$) of reflection coefficient over sucrose content with various frequencies for Honey Gold.

Table 3: Mathematical expression for magnitude and phase in predicting water content (wc) for (a) Honey Gold and (b) Trigona Honey

(a)		
f (GHz)	$\|\Gamma\|$	
	Equation	$\mathbf{R^2}$
0.60	$\|\Gamma\| = -1.384wc^3 + 2.400wc^2 - 1.322\ wc + 1.060$	0.919
2.28	$\|\Gamma\| = -3.849wc^3 + 6.898wc^2 - 3.677wc + 1.325$	0.972
3.47	$\|\Gamma\| = -1.605wc^3 + 3.156wc^2 - 1.657wc + 1.004$	0.814
f (GHz)	$-\varphi$ **(Deg)**	
	Equation	$\mathbf{R^2}$
0.60	$-\varphi = 48.56wc + 154.3$	0.975
2.28	$-\varphi = 146.1wc + 575.3$	0.953
3.47	$-\varphi = 168.8wc + 873.2$	0.899
(b)		
f (GHz)	$\|\Gamma\|$	
	Equation	$\mathbf{R^2}$
0.60	$\|\Gamma\| = -1.068wc^3 + 2.238wc^2 - 1.536wc + 1.170$	0.853
2.28	$\|\Gamma\| = -7.603wc^3 + 14.88wc^2 - 9.004wc + 2.412$	0.977
3.47	$\|\Gamma\| = -4.159wc^3 + 8.260wc^2 - 4.928wc + 1.536$	0.939
f (GHz)	$-\varphi$ **(Deg)**	
	Equation	$\mathbf{R^2}$
0.60	$-\varphi = 32.01wc + 166.4$	0.931
2.28	$-\varphi = 148.9wc + 553.1$	0.946
3.47	$-\varphi = 172.4wc + 862.2$	0.910

fructose, it has high inertia. This causes great reluctance in polarization, friction and collision. As a result the variation of $-\varphi$ is smaller if compared to Figures 4 (b) and 5 (b) for water adulterated samples. Microwave signal has lower sensitivity towards sucrose content than water content due to the heaviest molecular weight of sucrose. It justified that sucrose content bring insignificant effect to phase measurement.

C. Relationship between reflection coefficient, water content, and sucrose content

In Table 3, the correlation of water content and reflection coefficient for each frequency exhibit considerable high for both honeys as indicated by the fitting coefficient R^2. The R^2 is a statistical measure that represents the proportion of the variance for a dependent variable that's explained by an independent variable or variables in a regression model. The $|\Gamma|$ are fitted with cubic polynomial model while the $-\varphi$ are expressed in linear model. The cubic polynomial model was used in the $|\Gamma|$ fitting due to multiple reflections that attributed to inhomogeneity in sample under test. The multiple reflections may cause distortion on reflected fields due to constructive and destructive superposition. However, it affects linearly towards the $-\varphi$. It is due to the extremely high of dipole moment of water molecule that becomes dominant in determining the $-\varphi$ measurement,

Table 4: Mathematical expression for magnitude and phase in predicting sucrose content (*sc*) for (a) Honey Gold and (b) Trigona Honey

(a)		
f (GHz)	$\lvert\Gamma\rvert$	
	Equation	$\mathbf{R^2}$
0.60	$\lvert\Gamma\rvert = 0.652sc^3 - 1.152sc^2 + 0.573sc + 0.848$	0.772
2.28	$\lvert\Gamma\rvert = 0.209sc^3 - 0.404sc^2 + 0.097sc + 0.777$	0.767
3.47	$\lvert\Gamma\rvert = 1.727sc^3 - 2.973sc^2 + 1.282sc + 0.612$	0.871
f (GHz)	$-\varphi$ **(Deg)**	
	Equation	$\mathbf{R^2}$
0.60	$-\varphi = 227.9sc^3$ - $407.6sc^2 + 205.2sc + 155.5$	0.809
2.28	$-\varphi = 690.4sc^3 - 1203sc^2 + 564.9sc + 584.0$	0.815
3.47	$-\varphi = 843.6sc^3 - 1514sc^2 + 772.7sc + 873.7$	0.778
(b)		
f (GHz)	$\lvert\Gamma\rvert$	
	Equation	$\mathbf{R^2}$
0.60	$\lvert\Gamma\rvert = 0.652sc^3 - 1.152sc^2 + 0.573sc + 0.848$	0.772
2.28	$\lvert\Gamma\rvert = 0.209sc^3 - 0.404sc^2 + 0.097sc + 0.777$	0.767
3.47	$\lvert\Gamma\rvert = 1.727sc^3 - 2.973sc^2 + 1.282sc + 0.612$	0.871
f (GHz)	$-\varphi$ **(Deg)**	
	Equation	$\mathbf{R^2}$
0.60	$-\varphi = 76.60sc^3 - 137.1sc^2 + 66.74sc + 175.1$	0.621
2.28	$-\varphi = 491.3sc^3 - 905.7sc^2 + 464.2sc + 588.8$	0.738
3.47	$-\varphi = 683.2sc^3 - 1217sc^2 + 616.0sc + 897.4$	0.770

instead of the effect from multiple reflection. As a result, polarization of water molecule in water adulterated honey cause linear relationship between $-\varphi$ and water content.

In Table 4, the $|\Gamma|$ is similar as in Table 3 where it expressed cubically over sucrose content. However, the $-\varphi$ fitting of the sucrose content for both honeys is not linearly expressed in Table 4. It is different when compare with water adulterated honeys. The sucrose adulterated honey shows cubic mathematical expression to express the $-\varphi$ using sucrose content with considerable good of R^2(= 0.7). It was due to heavier molecular weight and smaller dipole moment of sucrose molecule than water molecule. The extreme dielectric behaviour of water molecule might divert attention from sucrose content during the $-\varphi$ measurement over adulteration of sucrose in both honeys as shown in Table 4. The $-\varphi$ seem more sensitive than $|\Gamma|$. It can be justified by the high gradient of each mathematical model of $-\varphi$ in function of water and sucrose content.

The $-\varphi$ of sucrose adulterated honeys is more sensitive in responding to variation of sucrose content than water adulterated honeys in responding to the variation of water content. In general, sucrose molecule has heavier molecular weight than water molecule, but similar dipole moment with water molecule. Subsequently, it leads to high impedance mismatch. The molecular weight of water and sucrose molecule is 18 g/mol and 342 g/mol, respectively. This phenomenon causes high sensitivity of $-\varphi$ towards variation of sucrose during adulteration. Meanwhile, the $|\Gamma|$ is mostly exhibit higher sensitivity for water adulterated honeys than sucrose adulterated honeys.

The relationships of actual water content (*awc*) and predicted water content (*pwc*) as tabulated in Table 5. The prediction of water content of both honeys can be acquired through simple mathematical approach. However, the $|\Gamma|$ is not able to provide unique solution. It can be solved by implementing the developed cubic polynomial model as listed in Table 3 via inverse matrix method. Hence, it can be noticed that the relationship between *awc* and *pwc* is solely presented by one equa-

Table 5: Mathematical models of actual water content (*awc*) and predicted water content (*psc*) for (a) Honey Gold and (b) Trigona Honey

(a)		
f (GHz)	$\lvert\Gamma\rvert$	
	Equation	$\mathbf{R^2}$
0.60 2.28 3.47	$awc = pwc$	1.000
f (GHz)	$-\varphi$ **(Deg)**	
	Equation	$\mathbf{R^2}$
0.60	$awc = 1.020pwc + 0.006$	0.999
2.28	$awc = 0.960pwc + 0.018$	0.954
3.47	$awc = 0.901pwc + 0.046$	0.900
(b)		
f (GHz)	$\lvert\Gamma\rvert$	
	Equation	$\mathbf{R^2}$
0.60 2.28 3.47	$awc = 0.990pwc + 0.002$	0.997
f (GHz)	$-\varphi$ **(Deg)**	
	Equation	$\mathbf{R^2}$
0.60	$awc = 0.929pwc + 0.038$	0.926
2.28	$awc = 0.950pwc + 0.028$	0.944
3.47	$awc = 0.907pwc + 0.052$	0.920

Table 6: Mathematical models of actual sucrose content (*asc*) and predicted sucrose content (*psc*) for (a) Honey Gold and (b) Trigona Honey

(a)		
f(GHz)	$\|\Gamma\|$	
	Equation	$\mathbf{R^2}$
0.60	*asc* = *psc*	1.000
2.28		
3.47		
f(GHz)	$-\varphi$ **(Deg)**	
	Equation	$\mathbf{R^2}$
0.60	*asc* = 0.997*psc* + 0.004	0.999
2.28		
3.47		
(b)		
f(GHz)	$\|\Gamma\|$	
	Equation	$\mathbf{R^2}$
0.60	*asc* = *psc*	1.000
2.28		
3.47		
f(GHz)	$-\varphi$ **(Deg)**	
	Equation	$\mathbf{R^2}$
0.60	*asc* = *psc*	1.000
2.28		
3.47		

tion for three frequencies. The developed FPR exhibit R^2= 0.9 for both honeys in the $|\Gamma|$ for predicted real water content (*pwc*). Similarly, the $|\Gamma|$ of sucrose adulteration between real and predicted sucrose content achieve R^2= 0.9 for both honeys. Meanwhile, mathematical relationships for the $-\varphi$ are well presented in linear model with R^2= 0.8. All linear models provide unity gradient and null y-intercept. It implies that the predicted water content (*pwc*) has good agreement with actual water content (*awc*). Likewise, linear models to relate between actual sucrose content (*asc*) and predicted sucrose content (*psc*) as listed in Table 6 provide R^2= 0.8 with approximate unity gradient and null y intercept.

To validate the data and ensure the reliability, the measurements of FPR were compared with the commercial Network Analyzer, Agilent E8362B PNA (vector network analyzer). The frequency response of measured $|\Gamma|$ and φ for FPR and PNA are consistent. Absolute error $|\Gamma|$ and $-\varphi$ is less than 0.15 and 17°, respectively in measurement of water content in honeys. Meanwhile. the absolute error of $|\Gamma|$ and $-\varphi$ is less than 0.13 and 14°, respectively in measurement of sucrose content in honeys.

In additional to the data used to fit, an additional experiment has been conducted to verify the correctness of the fitting functions in Tables 3–6. The measurement setup in this work provides an accurate prediction in terms of water content and sucrose content. $|\Gamma|$ and $-\varphi$ are accurate in predicting water content in both honeys with the absolute error < 0.1 and $< 25°$. However, $|\Gamma|$ has the best agreement where it provides unity gradient and zero y intercept. Withal, $|\Gamma|$ and $-\varphi$ can also predict sucrose content accurately for both honeys with the mean absolute error of 0.04 ± 0.03 and $7.6° \pm 6.4°$, respectively. $|\Gamma|$ and $-\varphi$ exhibit unity gradient and zero y-intercept. However, $-\varphi$ present the highest sensitivity towards the variation of sucrose content in honeys [27]. Suffice to say, FPR with developed five ports ring junction circuit can provide accurate water and sucrose content prediction for multiple frequencies. The FPR can be used as an alternative instrumentation system to characterize pure and adulterated honey.

IV. CONCLUSION

The developed ring junction circuit with operating frequencies of 0.60 GHz, 2.28 GHz and 3.47 GHz. The simulated S-Parameter at these frequencies comply with Riblet & Hansson theory. Meanwhile, the measured S-Parameters through FPR at these frequencies have good agreement with simulated S-Parameter and has been validated with the VNA measurement. The relationship of water content (*wc*) or sucrose content (*sc*) with $|\Gamma|$ and $-\varphi$ were established in mathematical models. The mathematical correlation among *wc* or *sc* in pure and adulterated honeys with $|\Gamma|$ and $-\varphi$ were investigated through coefficient of determination, R^2. This work is only based on a single variable (water or sucrose content). These two substances are commonly found in the market and impose a huge impact on the honey industry. Hence, this work was limited to single variable (either water content or sucrose content). The multivariable regression analysis is conducted in future work.

In overall, high R^2 indicates a good agreement between the calculation (mathematical model) and measurement in term of reflection coefficient. In addition, *wc* and *sc* can be predicted accurately through $|\Gamma|$ and $-\varphi$ using these developed models. The developed FPR can provides an accurate water and sucrose content prediction for both honeys. The FPR is able to identify pure and adulterated honey through the investigation of water and sucrose content. A similar approach can be extended for other sample of interest which has similar characteristics to Honey Gold and Trigona Honey.

ACKNOWLEDGMENT

The author would like to acknowledge the support from the UniPRIMA under a grant number of 9001-00710 & 9002-00146 from the Ministry of Higher Education Malaysia.

REFERENCES

[1] E. Anklam, "A review of the analytical methods to determine geographical and botanical origin of honey," *Food Chem.*, vol. 63, no. 4, pp. 549-562, 1998.

[2] L. Vandamme, A. Heyneman, H. Hoeksema, J. Verbelen, and S. Monstrey, "Honey in modern wound care: A systematic review," *Burns*, vol. 39, no. 8, pp. 1514-1525, 2013.

[3] M. Moniruzzaman, S. A. Sulaiman, I. Khalil, and S. H. Gan, "Evaluation of physiochemical and antioxidant properties of sourwood and other Malaysian honeys: A comparison with Manuka honey," *Chem. Cent. J.*, vol. 7, no. 1, pp. 1-12, 2013.

[4] E. Diacu and E. F. "Tantaveanu, determination of moisture content and its correlation with other parameters in honey quality control," *Revista de Chimie*, vol. 58, no. 12, pp. 1311-1312, 2007.

[5] A. I. Ruiz-Matute, M. Brokl, A. C. Soria, and I. Martínez-Castro, "Gas chromatographic-mass spectrometric characterization of tri- and tetrasaccharidesin honey," *Food Chem*., vol. 120, no. 2, pp. 637-642, 2010.

[6] M. Tahsin, N. Berna, O. Said, S. Karaman, E. Dertli, O. Sagdic, and M. Arici, "Steady, dynamic and creep rheological analysis as a novel approach to detect honey adulteration by fructose and saccharose syrups: Correlations with HPLC-RID results," *Food Res. Int*., vol. 64, pp. 634-646, 2014.

[7] A. I. Cabañero, J. L. Recio, and M. Rupérez, "Liquid chromatography coupled to isotope ratio mass spectrometry: A new perspective on honey adulteration detection," *J. Agric. Food Chem*., vol. 54, no. 26, pp. 9719-9727, 2006.

[8] C. Y. Lee, K. Y. You, T. S. Tan, Y. L. Then, Y. S. Lee, L. Zahid, W. L. Lim, and C. H. Lee, "Enhanced five-port ring circuit reflectometer for synthetic breast tissue dielectric determination," *Prog. Electromagn. Res. C*, vol. 69, pp. 83-95, 2016.

[9] J. Ahmed, S. T. Prabhu, G. S. V. Raghavan, and M. Ngadi, "Physico-chemical, rheological, calorimetric and dielectric behaviour of selected Indian honey," *J. Food Eng*., vol. 79, no. 4, pp. 1207-1213, 2007.

[10] F. Içier and T. Baysal, "Dielectrical properties of food materials-1: Factors affecting and industrial uses," *Crit. Rev Food Sci. Nutr.*, vol. 44, no. 6, pp. 465-471, 2004.

[11] H. Cong, F. Liu, Z. Tang, and C. Xue, "Dielectric properties of sea cucumbers (Stichopus japonicus) and model foods at 915 MHz," *J. Food Eng.*, vol. 109, no. 3, pp. 635-639, 2012.

[12] N. Bansal, A. S. Dhaliwal, and K. S. Mann, "Dielectric properties of corn flour from 0.2 to 10 GHz," *J. Food Eng.*, vol. 166, pp. 255-262, 2015.

[13] S. Zhang, L. Zhou, B. Ling, and S. Wang, "Dielectric properties of peanut kernels associated with microwave and radio frequency drying," *Biosyst. Eng.*, vol. 145, pp. 108-117, 2016.

[14] E. M. Cheng, Z. Abbas, M. F. AbdulMalek, K. Y. Lee, K. Y. You, S. F. Khor. J. Hassan, and H. Zainuddin, "Finite difference analysis of an open-ended, coaxial sensor made of semi-rigid coaxial cable for determination of moisture in *Tenera* oil palm fruit," *Applied Computational Electromagnetics Society (ACES) Journal*, vol. 31, no. 10, pp. 1181-1192, 2016.

[15] E. M. Cheng, Z. Abbas, M. F. AbdulMalek, K. Y. You, K. Y. Lee, S. F. Khor, N. F. Mohd Nasir, M. S. Abdul Majid, and S. F. Khor, "Effect of aspect ratio and frequency of an open-ended, coaxial line on admittance for determination of moisture in *Tenera* oil palm fruit using finite difference method," *Applied Computational Electromagnetics Society (ACES) Journal*, vol. 33, no. 11, pp. 1308-1318, 2018.

[16] P. Ferrazzoli, L. Guerriero, and D. Solimini, "Numerical model of microwave backscattering and emission from terrain covered with vegetation," *Applied Computational Electromagnetics Society (ACES) Journal*, vol. 6, no. 1, pp. 175-191, 1991.

[17] D. T. Le and B. Bisceglia, "Specific absorption rate for agri-food materials from multiple antenna exposure," *Applied Computational Electromagnetics Society (ACES) Journal,* vol. 1, no. 2, pp. 68-71, 2016.

[18] S. A. Galema, "Microwave chemistry," *Chem. Soc. Rev.*, vol. 26, no. 3, pp. 233-238, 1997.

[19] G. F. Engen, "An improved circuit for implementing the six-port technique of microwave measurement," *IEEE Trans. Microw. Theory Tech.*, vol. 25, no. 12, pp. 1080-1083, 1977.

[20] G. P. Riblet and E. R. B. Hansson, "An ideal six-port network consisting of a matched reciprocal lossless five-port and a perfect directional coupler," *IEEE Trans. Microw. Theory Tech.*, vol. 83, no. 3, pp. 284-288, 1983.

[21] K. Y. Lee, B. K. Chung, K. Y. You, E. M. Cheng, and Z. Abbas, "Development of a symmetric ring junction as four-port reflectometer for complex reflection coefficient measurements," *Radioengineering*, vol. 24, no. 4, pp. 906-911, 2015.

[22] Q. Zhan, Y. Wang, Y. Fang, Q. Ren, S. Yang, W. Yin, and Q. H. Liu, "An adaptive high-order transient algorithm to solve large-scale anisotropic Maxwell's equations," *IEEE Trans. Antennas Propagat.*, vol. 70, no. 3, pp. 2082-2092, 2021.

[23] Q. Zhan, Y. Fang, M. Zhuang, M. Yuan, and Q. H. Liu, "Stabilized DG-PSTD method with nonconformal meshes for electromagnetic waves," *IEEE Trans. Antennas Propagat.*, vol. 68, no. 6, pp. 4714-4726, 2020.

[24] J. Y. Ahn, D. Y. Kil, C. Kong, and B. Kim, "Comparison of oven-drying methods for determination of moisture content in feed ingredients," *Asian Australasian J. Animal Sci.*, vol. 27, no. 11, pp. 1615-1622, 2014.

[25] W. Guo, X. Zhu, Y. Liu, and H. Zhuang, "Sugar and water contents of honey with dielectric property sensing," *J. Food Eng.*, vol. 97, no. 2, pp. 275-281, 2010.

[26] W. Guo, Y. Liu, X. Zhu, and S. Wang, "Dielectric properties of honey adulterated with sucrose syrup," *J. Food Eng.*, vol. 107, no. 1, pp. 1-7, 2011.

[27] S. Aishah, "Development of pure and adulterated honey measurement system using multiple frequencies six-port reflectometer (SPR)," *MSc dissertation, Sch. Mechatron. Eng. Univ. Malaysia Perlis*, Perlis, Malaysia, 2017.

[28] S. P. Kek, N. L. Chin, S. W. Tan, and Y. A. Yusof, "Classification of honey from its bee origin via chemical profiles and mineral content," *Food Anal. Methods*, vol. 10, pp. 19-30, 2017.

[29] S. Ueno, *Biological Effects of Magnetic and Electromagnetic Fields*. Springer, New York, NY, 1996.

[30] G. Jose, A. Carolina, and D. Erik, "Acute effect of meal glycemic index and glycemix load on blood glucose and insulin responses in humans," *Nutr. J.*, vol. 22, no. 5, pp. 1-7, 2006.

[31] M. Kumar and R. Gupta, *Diamagnetic Susceptibility of Organic Compounds, Oils, Paraffins and Polyethylenes*. Berlin Heidelberg: Springer-Verlag, 2008.

Lee Kim Yee was born in 1978. He received his BSc Physics, Master and PhD degree from the Universiti Putra Malaysia (stocktickerUPM) in the year 2002, 2004 and 2008 respectively. He joined the Lee Kong Chian Faculty of Engineering and Science, Universiti Tunku Abdul Rahman (UTAR) in 2007. He is currently an associate professor under Department of Electrical and Electronic Engineering. His research interests include microwave measurement technique, microwave circuit and instrumentation, dielectric measurement, and RFID.

Shahriman Abu Bakar is an Assoc Prof in Faculty of Mechanical Engineering Technology In Universiti Malaysia Perlis. He is currently the head of Centre of Excellence in Automotive and Motorsport. He obtained his degree in Mechanical engineering in 1997, Master in Mechanical Engineering in 2006 and Phd in System Design in 2010 all from Mie University Japan. He holds 2 patents and filed for 6 patents in transportation systems. His research interest is in automotive systems for vehicles, mobility as a service, next generation vehicles and agriculture industries. He published more than 240 articles and conference proceedings. He is a professional engineer (Board of engineer Malaysia) and professional technologist (MBOT Malaysia).

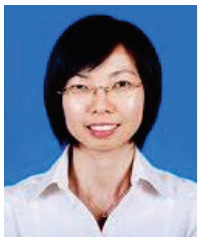

Shing Fhan Khor was born in 1982. She obtained her B.Sc. with Edu. (Honours) - Physics in Universiti Putra Malaysia in 2007. She pursued her Ph.D. in Materials Science at the Faculty of Science in 2011 at Universiti Putra Malaysia. Recently, she is an associate professor at Faculty of Electrical Engineering Technology, Universiti Malaysia Perlis (UniMAP). Her main personal research interest is in the glass science and focusing on dielectric, optical, mechanical and thermal properties.

Cheng Ee Meng was born in 1980. He obtained his B.Sc (Honours) - Instrumentation Science in Universiti Putra Malaysia in 2004. He pursued his M.Sc. in Wave Propagation at the Institute for Mathematical Research on 2005 in Universiti Putra Malaysia and his Ph.D. in Microwave at the Faculty of Science, Universiti Putra Malaysia in 2007. Recently, he is an associate professor in Faculty of Electronic Engineering Technology, Universiti Malaysia Perlis. His main personnel research interest is in the computational electromagnetic

modeling, microwave dielectric spectroscopy, wave propagation in RF & microwave and microwave sensors development for food and agricultural applications. On the other hand, he is also a Chartered Engineer (Engineering Council, UK) and Professional Technologist (MBOT, Malaysia). He also published more than 100 journals and conference proceedings (ISI/Scopus).

Nashrul Fazli Mohd Nasir received his Bachelor Degree in Biomedical Engineering from Universiti Malaya and later pursued his M.Sc. in Biomedical Engineering at Keele University (UK). He later received his Ph.D. in Electrical Engineering and Computer Engineering from Royal Melbourne Institution of Technology (RMIT) University, Australia. His research interests are in Biomaterials, Biosensors and Material Characterization in Biomedical Engineering. Currently, he is the associate professor in Faculty of Electronic Engineering Technology, Universiti Malaysia Perlis.

Siti Aishah Baharuddin is a full time PhD student in Faculty of Engineering, Universiti Putra Malaysia (UPM) in Food Engineering field. Her doctoral research is to develop functional food from medicinal plants for Colorectal Cancer (CRC) prevention. Her research is conducted under collaboration with Osaka University of Pharmaceutical Sciences, Japan. On top of this, her research work has given her in-depth understanding and knowledge in food processing, food powder technology, and physicochemical properties of food.

Che Wan Sharifah Robiah Mohamad was born in 1978. He obtained his B.Sc. (Honours) - Microbiology in Universiti Sains Malaysia in 2001. She pursued her M.Sc. in Microbiology (Bacteriology) at School of Biological Sciences on 2006 in Universiti Sains Malaysia and his Ph.D. in Biotechnology Microbe in 2006 in Universiti Sains Malaysia. Recently, she is a senior lecturer in Faculty of Electronic Engineering Technology, Universiti Malaysia Perlis. Her main personnel research interest is in the antimicrobial study, biomaterial and tissue engineering for medical and pharmaceutical applications. On the other hand, she is also a Professional Technologist (MBOT, Malaysia).

Emma Ziezie Mohd Tarmizi received her Bsc (Hons) (Material Science), MSc (Dielectric Physics) and PhD (Material Science) from the Universiti Putra Malaysia. She took a keen interest in education and currently serving as a Senior lecturer and Coordinator for Physics (foundation) at the Centre of Foundation Studies For Agricultural Science, Universiti Putra Malaysia. Emma's research focuses on the various electrical, thermal and optical properties of materials including glasses, polymers and conducting polymers for diverse of applications including laser, fuel cell and solar cell. She currently aims at studying the fundamental aspects of broad range of advanced materials, designing and synthesizing functional materials for biomedical and biological applications which may crosses many disciplines including physics, chemistry, biological, medical and engineering technology.

Novel Parallelization of Discontinuous Galerkin Method for Transient Electromagnetics Simulation Based on Sunway Supercomputers

Minxuan Li, Qingkai Wu, Zhongchao Lin, Yu Zhang, and Xunwang Zhao

School of Electronic Engineering
Xidian University, Xi'an, 710071, China
lwdldj@163.com, zclin@xidian.edu.cn

***Abstract* –** A novel parallelization of discontinuous Galerkin time-domain (DGTD) method hybrid with the local time step (LTS) method on Sunway supercomputers for electromagnetic simulation is proposed. The proposed method includes a minimum number of roundtrip (MNR) strategy for processor-level parallelism and a double buffer strategy based on the remote memory access (RMA) of the Sunway processor. The MNR strategy optimizes the communication topology between nodes by recursively establishing the minimum spanning tree and the double buffer strategy is designed to make communication overlapped computation when RMA transmission. Combining the two methods, the proposed method achieves an unprecedented massively parallelism of the DGTD method. Several examples of radiation and scattering are used as cases to study the accuracy and validity of the proposed method. The numerical results show that the proposed method can effectively support 16,000 nodes (1,040,000 cores) parallelism on the Sunway supercomputer, which enables the DGTD method to solve the transient electromagnetic field in a very short time.

***Index Terms* –** discontinuous Galerkin method, electromagnetic analysis, memory access optimization, sunway TaihuLight.

I. INTRODUCTION

As one of the most accurate time-domain electromagnetic field calculation methods, the discontinuous Galerkin time-domain (DGTD) method has higher numerical accuracy and modeling flexibility than traditional time-domain methods, such as the finite difference time-domain (FDTD) method and the finite volume time-domain (FVTD) method [1–3]. Thus, it is widely used in the simulation of broadband characteristics in ultra-wideband (UWB) communication, pulse radar, time-domain measurement, and electromagnetic compatibility, etc [4, 5]. In the industrial application of the DGTD method [1–3, 8, 9], the important key technologies are multi-scale techniques and the massively parallelism techniques [10–12]. The common multiscale technique of the DGTD method is local time stepping (LTS). At present, some research on the thread-level parallelism of LTS-DGTD [13, 20, 21], which makes the implementation of the distributed parallelism of LTS-DGTD is feasible, has been performed. However, LTS-DGTD does not scale well on the multi-node parallelism between nodes [13, 14]. The multi-node parallelism is very common in distributed platforms, such as supercomputers. With the advancement of computer technology, supercomputers have reached tens of thousands of nodes so far [13, 15–17], and the maximum parallel size of the DGTD method has stopped at hundreds of nodes [14, 18–20], which makes the DGTD method unsuitable for electrically large problems on modern supercomputers with ever increasing nodes.. Therefore, the massively node-level parallelism for the LTS-DGTD method urgentiv.In addition, at the current situation of chip supply shortage and prohibition, it is necessary to study the parallelism of China's domestic processors, such as SW26010, which composes the Sunway TaihuLight, the most powerful supercomputer in China [21–26]. Based on SW26010, a new Sunway CPU has been developed [27]. The new Sunway CPU expands the computing processing element (CPE)'s local data memory (LDM) from 64KB to 256 KB and improves the bandwidth of the LDM controller. At the same time, the remote memory access (RMA) technology, which is one of the most attractive technological advances of the new Sunway CPU is introduced for the communication between CPEs. The new Sunway supercomputer composed of the new Sunway CPU, will be possible achieves 1000 PFlops [28]. However, there is no research on the DGTD method with the new Sunway CPU.

To solve these problems, this paper proposes a novel parallelism of the LTS-DGTD method for Sunway supercomputers. The proposed method has a minimum roundtrip strategy to improve the scalability of node-level parallelism of the LTS-DGTD method, and a double-buffer parallelism with RMA of LTS-DGTD method for the new Sunway supercomputer. The

Submitted On: June 23, 2022
Accepted On: September 24, 2022

https://doi.org/10.13052/2022.ACES.J.370706

double-buffer strategy is efficient for reducing the computing time in-cores and improves the communication efficiency of the LTS-DGTD in CPEs. These two proposed strategies enable the LTS-DGTD method to be implemented on the new Sunway supercomputer successfully and efficiently.

II. THE FORMULATION OF DISCONTINUOUS GALERKIN TIME-DOMAIN

The Maxwell's equation in 3D space [4] is:

$$\begin{cases} \nabla \times \boldsymbol{H} = \varepsilon \dfrac{\partial \boldsymbol{E}}{\partial t} + \boldsymbol{J} \\ \nabla \times \boldsymbol{E} = -\mu \dfrac{\partial \boldsymbol{H}}{\partial t} \\ \nabla \cdot \boldsymbol{D} = \rho \\ \nabla \cdot \boldsymbol{B} = 0, \end{cases} \tag{1}$$

in which $\boldsymbol{E}$, $\boldsymbol{H}$, $\boldsymbol{D}$ and $\boldsymbol{B}$ are the electric field intensity, magnetic field intensity, electric flux density, and magnetic flux density, respectively; ε is permittivity and μ is permeability, and $\boldsymbol{J}$ is the electric current density; ρ is the electric charge density. $\boldsymbol{E}$ and $\boldsymbol{H}$ are approximated as:

$$\begin{aligned} \boldsymbol{E} &= \sum_{i}^{n_p} E_i(t) \boldsymbol{N}_i \\ \boldsymbol{H} &= \sum_{i}^{n_p} H_i(t) \boldsymbol{N}_i, \end{aligned} \tag{2}$$

where $\boldsymbol{N}_i$ denotes the basis function, $E_i(t)$ and $H_i(t)$ are the time depent coefficients of basis function $\boldsymbol{N}_i$, n_p is the number of basis functions. In this study, the 0.5, 1 and 2 order hierarchical basis functions of [6] are used.

Following the Galerkin finite elements approach [1] to the curl operators of equation (1) without $\boldsymbol{J}$, it can be written as:

$$\begin{cases} \displaystyle\int_\Omega \nabla \times \boldsymbol{H} \cdot \boldsymbol{N}_i d\nu = \int_\Omega \varepsilon \frac{\partial \boldsymbol{E}}{\partial t} \cdot \boldsymbol{N}_i d\nu \\ \displaystyle\int_\Omega \nabla \times \boldsymbol{E} \cdot \boldsymbol{N}_i d\nu = -\int_\Omega \mu \frac{\partial \boldsymbol{H}}{\partial t} \cdot \boldsymbol{N}_i d\nu, \end{cases} \tag{3}$$

where Ω is the calculation domain divided into tetrahedrons. According to [1], with integration by parts, the weak forms of equation (3) are:

$$\begin{cases} \displaystyle\int_\Omega \varepsilon \frac{\partial \boldsymbol{E}}{\partial t} \cdot \boldsymbol{N}_i d\nu - \int_\Omega \nabla \times \boldsymbol{N}_i \cdot \boldsymbol{H} d\nu = \\ \qquad \displaystyle\int_\Gamma (\hat{\boldsymbol{n}} \times \boldsymbol{H}) \cdot \boldsymbol{N}_i ds \\ \displaystyle\int_\Omega \mu \frac{\partial \boldsymbol{H}}{\partial t} \cdot \boldsymbol{N}_i d\nu + \int_\Omega \nabla \times \boldsymbol{N}_i \cdot \boldsymbol{E} d\nu = \\ \qquad \displaystyle -\int_\Gamma (\hat{\boldsymbol{n}} \times \boldsymbol{E}) \cdot \boldsymbol{N}_i ds, \end{cases} \tag{4}$$

where Γ is the boundary of Ω, and $\hat{\boldsymbol{n}}$ is the normal vector located on Γ. The DGTD method introduces numerical fluxes to substitute for the right-terms, i.e., integration over the tetrahedron interfaces.We fthe procedure set out in [7] to deal with the right-terms of equation (4): solving the Riemann problem under the Rankine-Hugoniot condition yields an expression for the upwind flux:

$$\begin{aligned} \hat{\boldsymbol{n}} \times \boldsymbol{H}_i &= \hat{\boldsymbol{n}} \times \frac{Z_i \boldsymbol{H}_i + Z_j \boldsymbol{H}_j}{Z_i + Z_j} + \hat{\boldsymbol{n}} \times \hat{\boldsymbol{n}} \times \frac{\boldsymbol{E}_i - \boldsymbol{E}_j}{Z_i + Z_j} \\ \hat{\boldsymbol{n}} \times \boldsymbol{E}_i &= \hat{\boldsymbol{n}} \times \frac{Y_i \boldsymbol{E}_i + Y_j \boldsymbol{E}_j}{Y_i + Y_j} - \hat{\boldsymbol{n}} \times \hat{\boldsymbol{n}} \times \frac{\boldsymbol{E}_i - \boldsymbol{E}_j}{Y_i + Y_j}, \end{aligned} \tag{5}$$

where j is the adjacent tetrahedron of tetrahedron i, the wave impedances of i and j are $Z_i = \dfrac{1}{Y_i} = \sqrt{\dfrac{\mu_i}{\varepsilon_i}}$ and $Z_j = \dfrac{1}{Y_j} = \sqrt{\dfrac{\mu_j}{\varepsilon_j}}$, respectively. For anisotropic Maxwell equations, it is necessary to deal with the tensor matrices of permitivity and permeability, which has been well solved in [4] and [5]. The isotropy semi-discrete form with upwind flux is shown as:

$$\begin{aligned} &\int_\Omega \varepsilon \frac{\partial \boldsymbol{E}_i}{\partial t} \cdot \boldsymbol{N}_i d\nu - \int_\Omega \nabla \times \boldsymbol{H}_i \cdot \boldsymbol{N}_i d\nu = \\ &\int_\Gamma \left(\hat{\boldsymbol{n}} \times \frac{Z_j (\boldsymbol{H}_j - \boldsymbol{H}_i)}{Z_i + Z_j} - \hat{\boldsymbol{n}} \times \hat{\boldsymbol{n}} \times \frac{\boldsymbol{E}_i - \boldsymbol{E}_j}{Z_i + Z_j} \right) \cdot \boldsymbol{N}_i ds \\ &\int_\Omega \mu \frac{\partial \boldsymbol{H}_i}{\partial t} \cdot \boldsymbol{N}_i d\nu + \int_\Omega \nabla \times \boldsymbol{E}_i \cdot \boldsymbol{N}_i d\nu = \\ &-\int_\Gamma \left(\hat{\boldsymbol{n}} \times \frac{Y_j (\boldsymbol{E}_j - \boldsymbol{E}_i)}{Y_i + Y_j} + \hat{\boldsymbol{n}} \times \hat{\boldsymbol{n}} \times \frac{\boldsymbol{H}_i - \boldsymbol{H}_j}{Y_i + Y_j} \right) \cdot \boldsymbol{N}_i ds, \end{aligned} \tag{6}$$

which can be written as matrix forms as:

$$\begin{aligned} \varepsilon \mathbf{M} \frac{\partial \tilde{\boldsymbol{E}}_i}{\partial t} &= \mathbf{S} \tilde{\boldsymbol{H}}_i + \\ \sum_{f=1}^{4} \left(k_h \mathbf{F}_{\Gamma_f} (\tilde{\boldsymbol{H}}_j - \tilde{\boldsymbol{H}}_i) - v_e \mathbf{G}_{\Gamma_f} (\tilde{\boldsymbol{E}}_j - \tilde{\boldsymbol{E}}_i) \right) & \\ \mu \mathbf{M} \frac{\partial \tilde{\boldsymbol{H}}_i}{\partial t} &= -\mathbf{S} \tilde{\boldsymbol{E}}_i - \\ \sum_{f=1}^{4} \left(k_e \mathbf{F}_{\Gamma_f} (\tilde{\boldsymbol{E}}_j - \tilde{\boldsymbol{E}}_i) + v_h \mathbf{G}_{\Gamma_f} (\tilde{\boldsymbol{H}}_j - \tilde{\boldsymbol{H}}_i) \right), & \end{aligned} \tag{7}$$

where $\tilde{\boldsymbol{E}}$ and $\tilde{\boldsymbol{H}}$ denote vectors composed by E_i and H_i in the integral domain, respectively, the flux coefficients are $k_h = \dfrac{Z_j}{Z_i + Z_j}$, $k_e = \dfrac{Y_j}{Y_i + Y_j}$, $v_e = \dfrac{1}{Z_i + Z_j}$ and $v_h = \dfrac{1}{Y_i + Y_j}$, $\mathbf{M}$ is the mass matrix, $\mathbf{S}$ is the stiffness matrix,$\mathbf{F}$ and $\mathbf{G}$ are the flux matrices. Those matrices can be summarized:

$$\begin{aligned}\mathbf{M} &= \int_{\Omega} \boldsymbol{N}_i \cdot \boldsymbol{N}_i dv \\ \mathbf{S} &= \int_{\Omega} \nabla \times \boldsymbol{N}_i \cdot \boldsymbol{N}_i dv \\ \mathbf{F} &= \int_{\Gamma} \hat{\boldsymbol{n}} \times \boldsymbol{N}_k \cdot \boldsymbol{N}_i ds,\ (k = i||j) \\ \mathbf{G} &= \int_{\Gamma} \hat{\boldsymbol{n}} \times \hat{\boldsymbol{n}} \times \boldsymbol{N}_k \cdot \boldsymbol{N}_i ds, (k = i||j)\,.\end{aligned} \tag{8}$$

Those linear equations defined in one tetrahedron or a subdomain of Ω avoid composing a large sparse matrix.

Applying the explicit leapfrog (LF) scheme [10] to deal with the time derivative of equation (7), we have:

$$\begin{aligned}&\mu\mathbf{M}\frac{\tilde{\boldsymbol{H}}_i^{n+\frac{1}{2}} - \tilde{\boldsymbol{H}}_i^{n-\frac{1}{2}}}{\Delta t} = -\mathbf{S}\tilde{\boldsymbol{E}}_i^n - \\ &\sum_{f=1}^{4}\left(k_e\mathbf{F}_{\Gamma_f}(\tilde{\boldsymbol{E}}_j^n - \tilde{\boldsymbol{E}}_i^n) + v_h\mathbf{G}_{\Gamma_f}(\tilde{\boldsymbol{H}}_j^{n-\frac{1}{2}} - \tilde{\boldsymbol{H}}_i^{n-\frac{1}{2}})\right) \\ &\varepsilon\mathbf{M}\frac{\tilde{\boldsymbol{E}}_i^{n+1} - \tilde{\boldsymbol{E}}_i^n}{\Delta t} = \mathbf{S}\tilde{\boldsymbol{H}}_i^{n+\frac{1}{2}} + \\ &\sum_{f=1}^{4}\left(k_h\mathbf{F}_{\Gamma_f}(\tilde{\boldsymbol{H}}_j^{n+\frac{1}{2}} - \tilde{\boldsymbol{H}}_i^{n+\frac{1}{2}}) - v_e\mathbf{G}_{\Gamma_f}(\tilde{\boldsymbol{E}}_j^n - \tilde{\boldsymbol{E}}_i^n)\right),\end{aligned} \tag{9}$$

where Δt is the size of time step, $\tilde{\boldsymbol{E}}$ and $\tilde{\boldsymbol{H}}$ differ by half a time step. Following the CFL condition, the maximum time step size is limited by the smallest element.

The size of the smallest and biggest element is always large in practice, so that the time step size is too short for most elements which leads to a huge number of time steps. The LTS-DGTD method in [2] is:

$$\begin{aligned}&\mu\mathbf{M}\frac{\tilde{\boldsymbol{H}}_i^{n+\frac{1}{2p}} - \tilde{\boldsymbol{H}}_i^{n-\frac{1}{2p}}}{\Delta t/_p} = -\mathbf{S}\tilde{\boldsymbol{E}}_i^n - \\ &\sum_{f=1}^{4}\left(k_e\mathbf{F}_{\Gamma_f}(\tilde{\boldsymbol{E}}_j^n - \tilde{\boldsymbol{E}}_i^n) + v_h\mathbf{G}_{\Gamma_f}(\tilde{\boldsymbol{H}}_j^{n-\frac{1}{2}} - \tilde{\boldsymbol{H}}_i^{n-\frac{1}{2}})\right) \\ &\varepsilon\mathbf{M}\frac{\tilde{\boldsymbol{E}}_i^{n+\frac{1}{p}} - \tilde{\boldsymbol{E}}_i^n}{\Delta t/_p} = \mathbf{S}\tilde{\boldsymbol{H}}_i^{n+\frac{1}{2p}} + \\ &\sum_{f=1}^{4}\left(k_h\mathbf{F}_{\Gamma_f}(\tilde{\boldsymbol{H}}_j^{n+\frac{1}{2p}} - \tilde{\boldsymbol{H}}_i^{n+\frac{1}{2p}}) - v_e\mathbf{G}_{\Gamma_f}(\tilde{\boldsymbol{E}}_j^n - \tilde{\boldsymbol{E}}_i^n)\right),\end{aligned} \tag{10}$$

in which $p = 3^{M-N}$, M is the number of levels and N is the level of i. The minimum element size between levels varies by three times and the time step size is three times either. This greatly reduces the total amount of calculation. However, this scheme has a higher error in 3D space than in 2D space, so that the interpolation method is used on the different time step fields between adjacent elements of different levels to obtain pseudo time steps. This paper uses an interpolation method as follows:

$$\boldsymbol{u}_i^{n+T_j} = \frac{\Delta t_j}{\Delta t_i}(\boldsymbol{u}_i^n - \boldsymbol{u}_i^{n-T_i}), \tag{11}$$

where u is field and T_j is the time step size of element j, T_i is the time step size of element i. The computation work is shown in Fig. 1. The ratio of time step sizes of level1, level2 and level3 is 1:3:9. Pseudo time steps of higher level are obtained by equation (11) and provided to lower level, the stability of this scheme is proven in [1]. Obviously, the acceleration of LTS is determined by M and the number of elements in different levels.

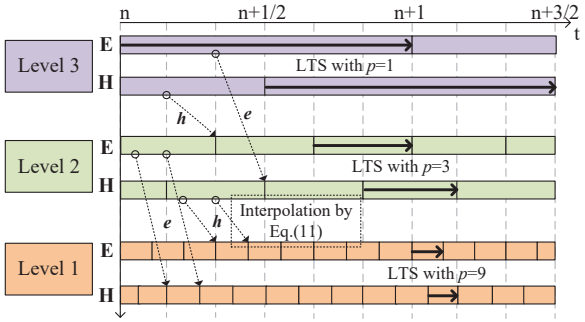

Fig. 1. Computation work of LTS-DGTD with interpolation, $\boldsymbol{E}$ and $\boldsymbol{H}$ are pseudo electric and magnetic field obtained by equation (11), respectively.

III. THE MINIMUM ROUNDTRIP STRATEGY FOR LTS-DGTD

Thread-level LTS-DGTD parallelism is very easy to implement due to the independence of the element in equation (10). When updating the electric and magnetic fields, it only depends on the fields of i and j in the previous time step. As for processor-level parallelism, equation (10) can be written as:

$$\begin{aligned}&\mu\mathbf{M}\frac{\tilde{\boldsymbol{H}}_i^{n+\frac{1}{2p}} - \tilde{\boldsymbol{H}}_i^{n-\frac{1}{2p}}}{\Delta t/_p} = -\mathbf{S}\tilde{\boldsymbol{E}}_i^n - \\ &\sum_{f=1}^{x}\left(k_e\mathbf{F}_{\Gamma_f}(\tilde{\boldsymbol{E}}_j^n - \tilde{\boldsymbol{E}}_i^n) + v_h\mathbf{G}_{\Gamma_f}(\tilde{\boldsymbol{H}}_j^{n-\frac{1}{2p}} - \tilde{\boldsymbol{J}}_i^{n-\frac{1}{2p}})\right) - \\ &\sum_{g=1}^{y}\left(k_e\mathbf{F}_{\Gamma_g}(\tilde{\boldsymbol{E}}_j^n - \tilde{\boldsymbol{E}}_i^n) + v_h\mathbf{G}_{\Gamma_g}(\tilde{\boldsymbol{H}}_j^{n-\frac{1}{2p}} - \tilde{\boldsymbol{H}}_i^{n-\frac{1}{2p}})\right) \\ &\varepsilon\mathbf{M}\frac{\tilde{\boldsymbol{E}}_i^{n+\frac{1}{p}} - \tilde{\boldsymbol{E}}_i^n}{\Delta t/_p} = \mathbf{S}\tilde{\boldsymbol{H}}_i^{n+\frac{1}{2p}} + \\ &\sum_{f=1}^{x}\left(k_h\mathbf{F}_{\Gamma_f}(\tilde{\boldsymbol{H}}_j^{n+\frac{1}{2p}} - \tilde{\boldsymbol{H}}_i^{n+\frac{1}{2p}}) - v_e\mathbf{G}_{\Gamma_f}(\tilde{\boldsymbol{E}}_j^n - \tilde{\boldsymbol{E}}_i^n)\right) + \\ &\sum_{g=1}^{y}\left(k_h\mathbf{F}_{\Gamma_g}(\tilde{\boldsymbol{H}}_j^{n+\frac{1}{2p}} - \tilde{\boldsymbol{H}}_i^{n+\frac{1}{2p}}) - v_e\mathbf{G}_{\Gamma_g}(\tilde{\boldsymbol{E}}_j^n - \tilde{\boldsymbol{E}}_i^n)\right)\end{aligned} \tag{12}$$

where x is the number of elements belong to the local processor and y is the number of elements belong to adjacent processors. Γ_g is the boundary adjacent with another processor.

When the LTS-DGTD method executing on a distributed platform, the communication is performed between the adjacent processors which always are defined on a host core of nodes. In this paper, the message passing interface (MPI) is used to support the communication between nodes. The logP [24] model is the most popular topology of distributed platforms, and its structure is shown in Fig. 2.

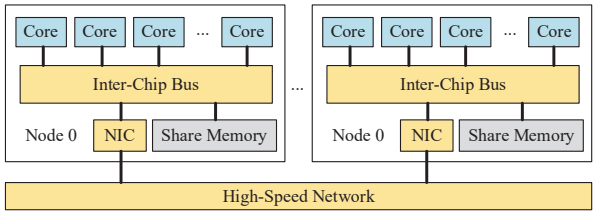

Fig. 2. The structure of massively distributed platform. Processor is defined on cores, and NIC is the network interface controller.

The running time of the logP model is:

$$T = T_c + T_m, \tag{13}$$

where T_c is the time of calculation, T_m is the time of communication. The computational time complexity of LTS-DGTD in each iteration step is determined by the number of elements of LTS levels. Communication time complexity T_m can be expressed as

$$T_m = \sum_{n=1}^{R} \frac{P_n}{S_n}, \tag{14}$$

where S_n is the network bandwidth, R is the number of roundtrips between nodes and P_n is the amount of data transmission per roundtrip. S_n can be considered a constant when data transmitting continuously between nodes. The memory of each node is accessed locally for the storage structure of the logP model, non-dependent processors do not influence each other while communicating, thus they can communicate at the same time. We should select nodes that communicating at the same time to reduce the number of roundtrips, so a minimum number of roundtrip (MNR) strategy is proposed to solve this problem.

As the global graph shown in Fig. 3, the number in a node represents the rank of a processor, the edge indicates the communication between two processes. Obviously, simple graph sorting cannot obtain the MNR. Referring to the Kruskal algorithm [29], only each independent subtree is saved in the process while finding the minimum spanning tree (MST), the number of independent subtrees is the MNR. This algorithm for finding MNR of the LTS method is MNR-LTS algorithm which has four steps as follows.

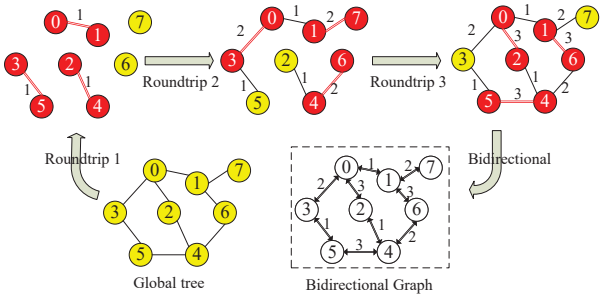

Fig. 3. The minimum number of roundtrips strategy and the graph of communication. The weight of edge is its roundtrip among the communication, the red circles indicate that the processor communicates in this roundtrip and the yellow circles indicate that the processor does not communicate.

Step 1 Mark the weights of edges in the graph as 0, set the current roundtrip as 1.

Step 2 Pick all unconnected edges in the graph, remark the weight of those edges as current roundtrip.

Step 3 Remove the picked edges of the previous step and create a new graph, add one to current roundtrip.

Step 4 Repeat steps 2 and 3 until all edges are remarked. These four steps are performed in every LTS levels, sum of all LTS levels roundtrip is the final number of roundtrips. The weight of an edge is the roundtrip of the communication between the processors connected by this edge. Since this graph is a bipartite graph above send and receive, the MNR should be twice the current roundtrip. Because the graph topology of nodes exists naturally, this method can be used on most distributed computers, such as distributed computing systems and supercomputers.

IV. PARALLELISM ON SUNWAY SUPERCOMPUTERS

The most classic Sunway many-core CPU is SW26010, which is based on the Alpha framework and composed of four core groups (CG). Each CG contains a management processing (MPE) and an 8 × 8 CPE cluster. Each CG has 8G of share memory space and can be accessed by the primary and secondary cores, while each CPE core has a separate LDM sized 64KB. The CPE core reads the LDM quickly, but because the local memory space is too small, it needs to communicate with the host memory using the direct memory access (DMA).

The task division of inner-chip is important for Sunway manycore CPU. The structure of Sunway CPU is

shown in Fig. 4, MPE broadcast the tetrahedrons and matrices to CPEs, and LDM receives them. However, the bandwidth of the interface is not optimal thus the communication between MPE and CPEs is slow. The conventional method to solve this problem is using DMA to transmit data. On the new general Sunway supercomputer, there is a better method to improve the communication efficiency of MPE to CPEs.

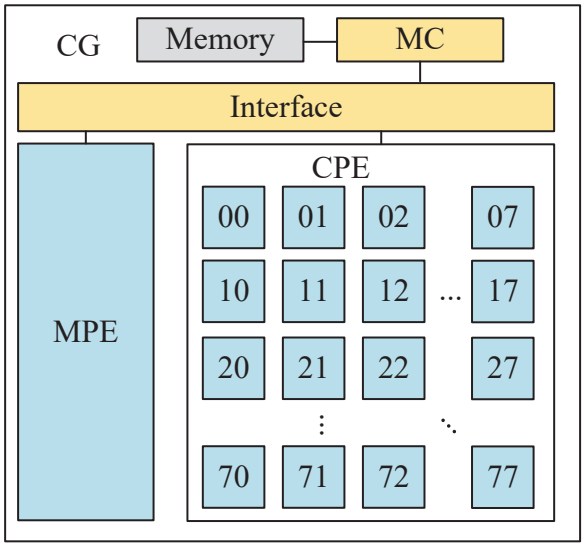

Fig. 4. Structure of SW26010 and new general Sunway CPU.

When LDM transmits data, MPE uses DMA channel to transfer data from main memory to local memory, which is suspended from the core processor and allows access to parts of local memory that are not data transferred for operation. At the RMA double-buffer (RMA-DB) strategy, the received CPE memory buffers are divided into two parts when transferring data from one core to another through CPE inter-communication on CPEs. The two buffers are used to transfer and calculate data alternately to achieve the effect of communication masking, which hides the transmit time behind the computation time as Fig. 5 shows. At the same time, the application of MNR strategy to control process-level data exchange between the core groups improves the parallel efficiency and is suitable for large-scale parallel computing.

It should be noted that although the RMA-DB strategy can hide the communication time behind the calculation time, the MPE to LDM still consumes a lot of time, which is caused by the Sunway CPU architecture.

V. NUMERICAL RESULTS AND ANALYSIS

Firstly, a radiation problem is considered to test the LTS-DGTD method with RMA-DB strategy. Patch

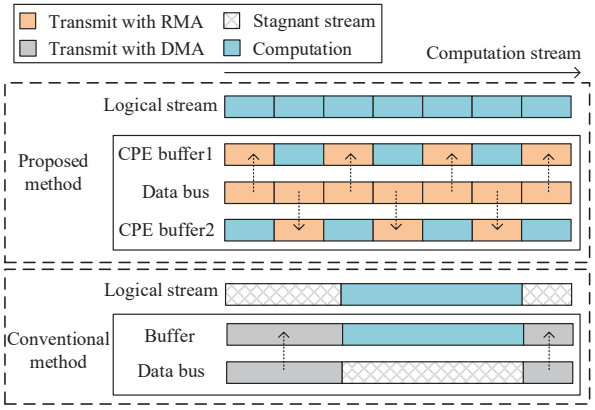

Fig. 5. Transmit data by RMA and DMA. In proposed method, buffer 1 and buffer 2 transfer data using RMA alternately. The stagnant stream denotes there is nothing to do at that moment.

Table 1: Running time of the proposed method

Kernel	LTS level	MPE time(s)	CPEs Cluster time(s)	RMA-DB time(s)
Update E	Level1	263.1	148.2	81.4
	Level2	295.5	156.3	85.2
	Level3	1845.6	945.8	443.7
Update H	Level1	262.5	147.8	80.9
	Level2	296.0	155.2	86.8
	Level3	1845.2	946.1	443.3

antennas are widely used in mobile communication and miniaturized radars, so in this paper a rectangular patch antenna is used to demonstrate the accuracy and efficiency of the proposed method. The rectangular patch is 22.7091 mm $\times$ 30.1615 mm, treated as perfect electric conductor (PEC), the size of the dielectric substrate is 34.92 mm $\times$ 38.65 mm $\times$ 3 mm and its relative permittivity is 4.5. A modulated Gaussian pulse in 2GHz to 6 GHz excites the coaxial wave port at the bottom of the antenna, inner and outer radius of the coaxial line are 0.44 mm and 1.5 mm, respectively. The coaxial line makes the antenna mesh has multi-scale size, there is no sparse matrix solver that can use RMA-DB strategy on the new sunway supercomputer for the time being, thus, the LTS-DGTD method is suitable for this problem. According to the wavelength of 4 GHz, 52,755 tetrahedrons were obtained through meshes discretisation, which is partitioned into 3 LTS levels in LTS-DGTD, the time step sizes are from 0.0602 ps to 0.5418 ps. The geometry and mesh of the patch antenna are shown in Fig. 6.

The S-parameter of the LTS-DGTD method on CPU and Sunway processor are exhibited in Fig. 7, the result

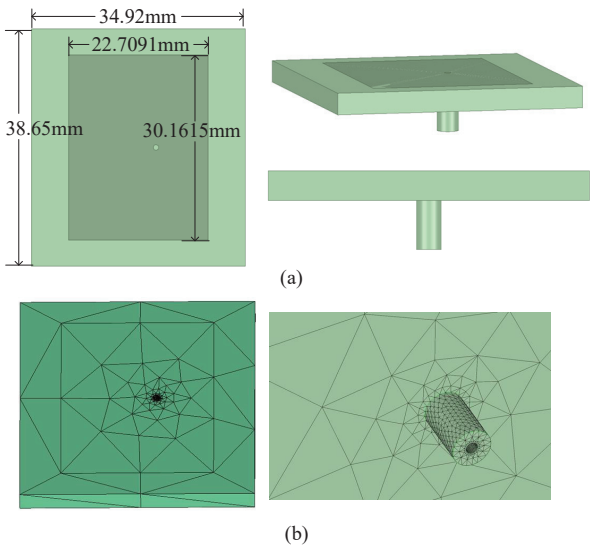

Fig. 6. The model and mesh of patch antenna. (a) Front, top, and side views of the model; (b) Top and bottom meshes.

of commercial software Ansys-HFSS is also proposed in Fig. 7. Its obviously that the accuracy of the proposed method on CPU is similar to that on Sunway. To show the efficiency of the RMA-DB strategy, the running time of different parts of the proposed method is summarized in Table 1, the update E is the first stage of Eq. (12) and the update H is the second stage of Eq. (12). With the RMA-DB strategy, CPEs has 4.15 acceleration than MPE, that demonstrates the efficiency of the RMA-DB strategy.

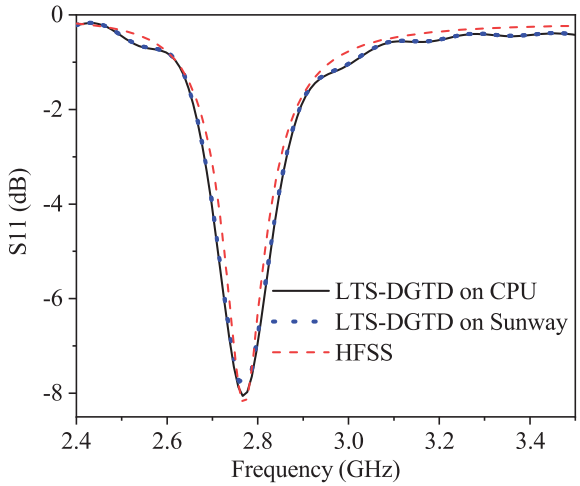

Fig. 7. Transmit data by RMA and DMA. In proposed method, buffer 1 and buffer 2 transfer data using RMA alternately. The stagnant stream denotes there is nothing to do at that moment.

Secondly, a slot antenna is used to demonstrate the performance of MNR strategy on homogeneous distributed computers. The geometry of the antenna is shown in Fig. 8. This antenna is excited by a coaxial wave port with the modulated Gaussian pulse in 15 GHz to 17 GHz. The antenna model is discretized into 1101096 tetrahedrons and is simulated by the DGTD-LTS method with MNR strategy on a homogeneous distributed computer. The homogeneous computer has 16 nodes, each node has 72 cores (Intel Xeon Gold 6140 @ 2.30GHz). The 120, 360, 720 and 936 cores cases employ 2, 6, 12 and 13 nodes, respectively. Cores are executed as threads by OpenMP. The Fig. 9 shows the gain obtained by the MNR strategy and the FDTD method. The calculation details of the original method and MNR strategy are given in Table 2. Compared with the original method, the MNR strategy significantly improves computational efficiency, and as the number of nodes increases, the acceleration becomes more obvious.

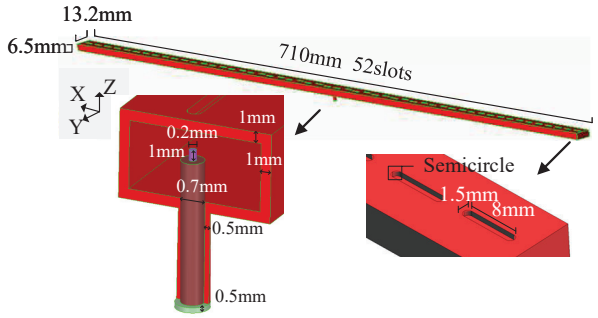

Fig. 8. Geometry of the slot antenna.

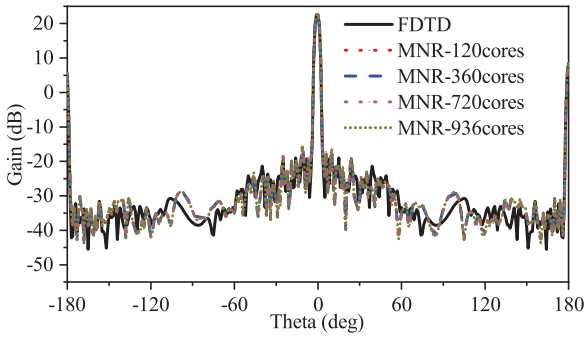

Fig. 9. Gain of the slot antenna obtained by the MNR strategy and FDTD method.

To show the performance of MNR strategy on supercomputers, a scatter analysis of an automobile is considered. The analysis of radar scattering can be regarded as a typical case of the electrically large-scale target simulation, similar analysis can be aimed at aircrafts, ships

Table 2: Computational Performance of the slot antenna

Number of cores	Time of original (min)	Time of MNR (min)	Speedup
120	143.07	136.55	1.05
360	56.95	47.44	1.20
720	34.10	24.75	1.38
936	29.07	19.67	1.48

Table 3: Computational Performance of automobile

Method	Number of Roundtrips	Time (s)	Speedup
Original	7590	8895.6	1
MNR	341	354.1	25.1

and other targets. The size of the automobile is 5.20 m × 1.82 m × 1.55 m, for the convenience of calculation, the shell of the car is regarded as PEC, the interior of the car is vacuum, and the tire is non-conductive rubber, which is regarded as microwave absorbing material. The plane wave with frequency of 800 MHz to 1200 MHz illuminates the car from front to back. Waves with this frequency band can attenuate slowly and propagate to distant place. To prove the efficiency of MNR strategy in the case of multiple nodes, this example is simulated by the Sunway TaihuLight supercomputer. The Sunway TaihuLight supercomputer has 4 SW26010 CPU per node and the SW26010 CPU has 65 cores [26].

The model is divided into 3,188,485 tetrahedrons and the LTS-DGTD method simulates this model with 1600 nodes (6400 processors) on the Sunway Taihulight supercomputer. To confirm the accuracy of the proposed method, the results of using and not using MNR strategy are compared and shown in Fig. 10. The normalized electric fields of the automobile from 3 ns to 14 ns obtained by the proposed method are shown in Fig. 11. In order to analyze the performance of MNR strategy, the calculation details are given in Table 3. Its obviously that the MNR strategy reduces the number of roundtrips by 22.3 times and improves the speed of data transmission by 25.1 times, and this result verifies the effectiveness of MNR strategy.

Slot antenna array always have high working frequency and strongly resonance, its transient characteristic is hard to be simulated by classical numerical method. There a slot antenna array to highlight the validity of the two proposed methods is shown. The array size is 0.34115 m × 0.018477 m × 0.35456 m and its working frequency band is 15.9 GHz–17.9 GHz, the curved slots make the model have multi-scale characteristics. Absorb boundary condition (ABC) is used to terminate the air box. A modulated Gaussian pulse from 14 GHz

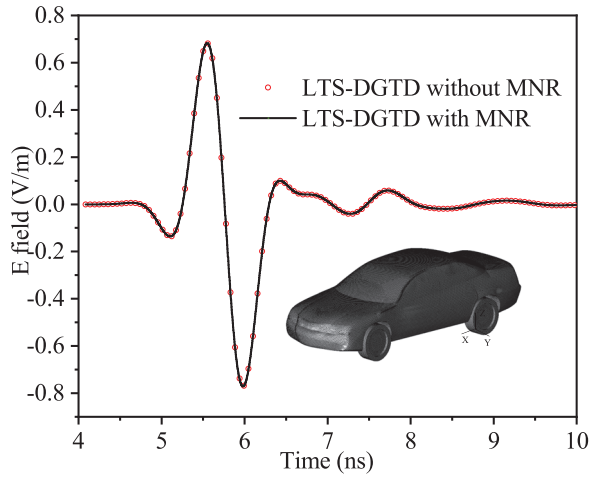

Fig. 10. Comparisons of electric field between the LTS-DGTD method with and without the MNR strategy.

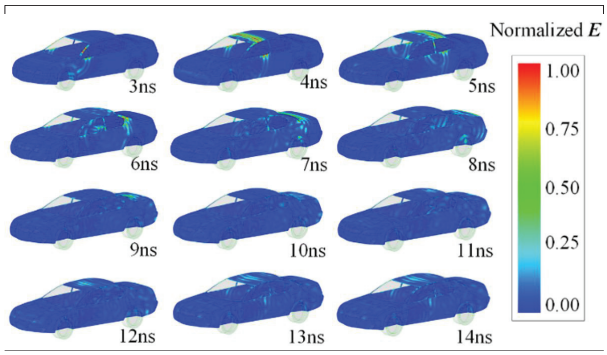

Fig. 11. Normalized electric field of the automobile from 3 ns to 14 ns proposed by the LTS-DGTD method with MNR strategy.

to 19 GHz is applied into a coaxial port which loaded at the bottom of the array. The model is divided into 19,320,201 tetrahedrons, whose number of unknowns is 386,404,020. The proposed method partitions the mesh into 5 LTS levels and the time steps are from 0.0243 ps to 1.9683 ps.

The proposed method is excuted with 4000 nodes (4 processors per node) on the new Sunway supercomputer, Fig. 12 shows the normalized directivity of 16GHz provided by measurement and the proposed method in plane yoz, and Fig. 13 shows the 3D directivity of the array and its transient electric fields at 1.5ns, 2ns and 3ns, which is helpful for us to analyze the excitation mode and design of slot antennas. The iteration time and strong scalability efficiency are presented in Table 4. The results show that the proposed method can achieve 73.8% parallel efficiency [24] when extended to 1040000 cores of 16000 processes, which expands the scale of the LTS-DGTD

Table 4: Computational Performance of automobile

Number of procs	Number of cores	Time of update (s)	Efficiency
1600	104,000	809.5	100.0
3200	208,000	409.8	98.7
6400	416,000	225.1	89.9
16000	1,040,000	109.6	73.8

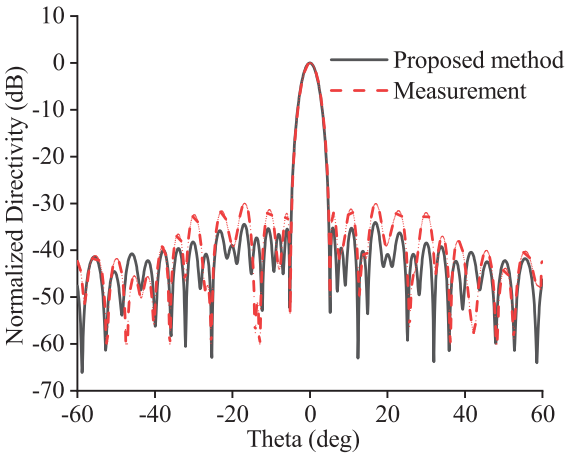

Fig. 12. Normalized directivity of slot antenna array in plane yoz.

method from hundreds of nodes to tens of thousands of nodes, and can effectively support its operation on modern supercomputers.

VI. CONCLUSION

In this paper, a high-performance parallelism of the LTS-DGTD method on China's homegrown Sunway supercomputers is proposed for the transient electromagnetic analysis. The MNR strategy is applied to reduce the communication roundtrip between multi-nodes system for the LTS-DGTD method, and a newly double-buffer strategy is employed to make the communication overlapped computation in CPEs with RMA transmission. Several numerical examples are used to demonstrate the performance and efficiency of the proposed method, which include the transient simulation of automobile, antenna and antenna array with analyzed on the Sunway TaihuLight and the new Sunway supercomputer. Numerical results show the parallel efficiency of the proposed method is 73.8% from 1600 nodes to 16000 nodes, which can be quite important for the application of the LTS-DGTD method in industrial simulation. At the same time, the MNR strategy in the proposed method can also be used on multi-node supercomputers other than Sunway supercomputer.

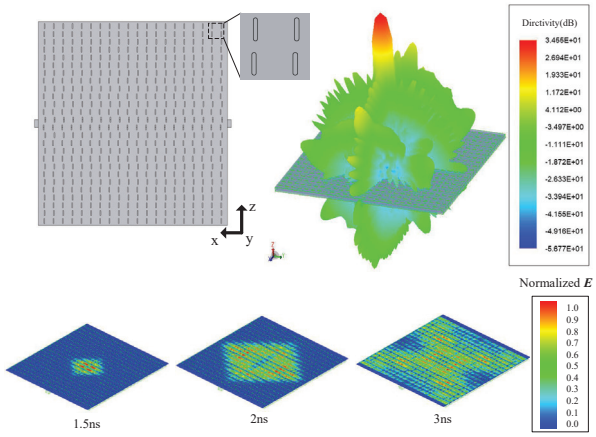

Fig. 13. Normalized directivity of slot antenna array in plane yoz.

ACKNOWLEDGMENT

The authors would like to thank Dr. Shugang Jiang from Xidian University for his valuable suggestions for this article. They would also like to appreciate constructive and professional comments from Editors and anonymous reviewers. This work was supported by the National Science Foundation of China (Grant No. 61901323), the Key Research and Development Program of Shaanxi (2021GXLH-02, 2022ZDLGY02-02) and the Fundamental Research Funds for the Central Universities (QTZX22155).

REFERENCES

[1] J. S. Hesthaven and T. Warburton, *Nodal Discontinuous Galerkin Methods: Algorithms, Analysis, and Applications*, Springer, New York, NY, USA, 2022.

[2] E. Montseny, S. Pernet, X. Ferrières, and G. Cohen, "Dissipative terms and local time-stepping improvements in a spatial high order Discontinuous Galerkin scheme for the time-domain Maxwell's equations," *J Comput. Phys*, vol. 227, no. 14, pp. 6795-6820, 2008.

[3] D. Sármány, M. A. Botchev, and J. J. M. Vegt, "Time-integration methods for finite element discretisations of the second-order Maxwell equation," *Computers and Mathematics with Applications*, vol. 65 no. 3, pp. 528-543, 2013. https://doi.org/10.1016/j.camwa.2012.05.023.

[4] Q. Zhan, Y. Fang, M. Zhuang, M. Yuan, and Q. H. Liu, "Stabilized DG-PSTD method With nonconformal meshes for electromagnetic waves," *IEEE*

Transactions on Antennas and Propagation, vol. 68, no. 6, pp. 4714-4726, Jun. 2020. https://doi.org/10.1109/TAP.2020.2970036.

[5] Q. Zhan, Y. Wang, Y. Fang, Q. Ren, S. Yang, and W.-Y. Yin, "An adaptive high-order transient algorithm to solve large-scale anisotropic Maxwell's equations," *IEEE Transactions on Antennas and Propagation*, vol. 70, no. 3, pp. 2082-2092, Mar. 2022. https://doi.org/10.1109/TAP.2021.3111639.

[6] J. P. Webb and B. Forgahani, "Hierarchal scalar and vector tetrahedra," *IEEE Transactions on Magnetics*, vol. 29, no. 2, pp. 1495-1498, Mar. 1993. https://doi.org/10.1109/20.250686.

[7] P. Li, Y. Shi, L. J. Jiang, and H. Bağcı, "A hybrid time-domain discontinuous Galerkin-boundary integral method for electromagnetic scattering analysis," *IEEE Transactions on Antennas and Propagation*, vol. 62, no. 5, pp. 2841-2846, May 2014. https://doi.org/10.1109/TAP.2014.2307294.

[8] H. X. Qi, Y. H. Wang, J. Zhang, X. H. Wang, and J. G. Wang, "Explicit high-order exponential time integrator for discontinuous Galerkin solution of Maxwell's equations," *Computer Physics Communications*, vol. 267, 2021. https://doi.org/10.1016/j.cpc.2021.108080.

[9] X. Li, L. Xu, H. Wang, Z. H. Yang, and B. Li, "A new implicit hybridizable discontinuous Galerkin time-domain method for solving the 3-D electromagnetic problems," *Applied Mathematics Letters*, vol. 93, 2019. https://doi.org/10.1016/j.aml.2019.02.004.

[10] J. F. Chen and Q. H. Liu, "Discontinuous Galerkin time-domain methods for multiscale electromagnetic simulations: A review," *Proc. IEEE*, vol. 101, no. 2, pp. 242-254, Feb. 2013.

[11] J. M. Jin, *Theory and Computation of Electromagnetic Fields*, Wiley-IEEE Press, USA, 2010.

[12] L. Raphaël, V. Jonathan, D. Clément, S. Claire, and L. Stéphane, "A parallel non-conforming multielement DGTD method for the simulation of electromagnetic wave interaction with metallic nanoparticles," *Journal of Computational and Applied Mathematics*, vol. 270, pp. 330-342, 2014. https://doi.org/10.1016/j.cam.2013.12.042.

[13] S. Dosopoulos, J. D. Gardiner, and J. F. Lee, "An MPI/GPU parallelization of an interior penalty discontinuous Galerkin time domain method for Maxwell's equations," *Radio Science*, 2011.

[14] H. H. Zhang, P. P. Wang, L. J. Jiang, W. Sha, M. S. Tong, Y. Liu, W. Wu, and G. Shi, "Parallel higher order DGTD and FETD for transient electromagnetic-circuital-thermal co-simulation," *IEEE Transactions on Microwave Theory and Techniques*, vol. 70, no. 6, pp. 1, 2022. https://doi.org/10.1109/TMTT.2022.3164703.

[15] P. Li, D. R. Chakrabarti, C. Ding, and L. Yuan, "Adaptive software caching for efcient NVRAM data persistence," *2017 IEEE International Parallel and Distributed Processing Symposium (IPDPS)*, pp. 112-122, 2017.

[16] K. Zhang, "The research and application of memory access optimization on heterogeneous multi-core platforms (in Chinese)," Dissertation, University of Science and Technology, Beijing, 2018.

[17] H. Bai, C. Hu, X. He, B. Zhang, and J. Wang, "Crystal MD: Molecular dynamic simulation software for metal with BCC structure," *Big Data Technology and Applications*, Springer, Singapore, pp. 247-258, 2017.

[18] D. Feng, S. Liu, X. Wang, X. Y. Wang, and G. Li, "High-order GPU-DGTD method based on unstructured grids for GPR simulation," *Journal of Applied Geophysics*, vol. 202, 2022. https://doi.org/10.1016/j.jappgeo.2022.104666.

[19] Z. G. Ban, Y. Shi, and P. Wang, "Advanced parallelism of DGTD method with local time stepping based on novel MPI + MPI unified parallel algorithm," *IEEE Transactions on Antennas and Propagation*, vol. 70, no. 5, pp. 3916-3921, 2022. https://doi.org/10.1109/TAP.2021.3137455.

[20] H. T. Mengand and J. M. Jin, "Acceleration of the dual-field domain decomposition algorithm using MPI–CUDA on large-scale computing systems," *IEEE Transactions on Antennas and Propagation*, vol. 62, no. 9, pp. 4706-4715, 2014. https://doi.org/10.1109/TAP.2014.2330608.

[21] G. Chen G, L. Zhao, and W. H. Yu, "A novel acceleration method for DGTD algorithm on sunway TaihuLight," *2018 IEEE Asia-Pacific Conference on Antennas and Propagation (APCAP)*, Auckland, New Zealand, 2018. https://doi.org/0.1109/APCAP.2018.8538209.

[22] J. Dongarra, "Sunway TaihuLight supercomputer makes its appearance," *Natl Sci Rev*., vol. 3, no. 3, pp. 265-266, 2019.

[23] Z. Xu, J. Lin, and S. Matsuoka, "Benchmarking SW26010 many-core processor," *IEEE International Parallel and Distributed Processing Symposium Workshops*, 2017.

[24] Z. Xu, J. Lin, and S. Matsuoka, "The compiling system user guide of Sunway TighthuLight," *National Super-computing Wuxi Center*, Wuxi, 2016.

[25] Y. Yu, H. An, J. Chen, W. Liang, Q. Xu, and Y. Chen, "Pipelining computation and opti-

mization strategies for scaling gromacs on the Sunway many-core processor," *Algorithms and Architectures for Parallel Processing*, vol. 10393, pp. 18-32, 2017.

[26] D. X. Chen and X. Liu, "Parallel programming andoptimization of Sunway Taihulight supercomputer (in Chinese)," *National Super-computing Wuxi Center*, Wuxi, 2017.

[27] J. Gu, J. W. Feng, X. Y. Hao, T. Fang, C. Zhao, H. An, J. Chen, M. Xu, J. Li, W. Han, C. Yang, F. Li, and D. Chen, "Establishing a non-hydrostatic global atmospheric modeling system at 3-km horizontal resolution with aerosol feedbacks on the Sunway supercomputer of China," *Science Bulletin*, vol. 67, no. 11, pp. 1170-1181, 2022. https://doi.org/10.1016/j.scib.2022.03.009.

[28] M. Dun, Y. C. Li, Q. X. Sun, H. L. Yang, W. Li, Z. Luan, L. Gan, G. Yang, and D. Qian, "Towards efficient canonical polyadic decomposition on sunway many-core processor," *Information Sciences*, vol. 549, pp. 221-248, 2021. https://doi.org/10.1016/j.ins.2020.11.013.

[29] R. Berger, S. Dubuisson, and C. Gonzales, "Fast multiple histogram computation using Kruskal's algorithm," *2012 19th IEEE International Conference on Image Processing*, 2012. https://doi.org/10.1109/ICIP.2012.6467374.

Minxuan Li was born in Changzhi, Shanxi, China, in 1994. He received the B.S. degree in electronic information engineering from Harbin Institute of Technology, Weihai, China in 2016. He is currently pursuing the Ph.D. degree with Xidian University, Xi'an, China. His current research interests include parallel computation and transient electromagnetic analysis.

Qingkai Wu was born in Yangzhou, Zhejiang, China, in 1997. He received the B.S. degree in electronic science and technology from Xidian University, Xi'an, China in 2020. He is currently pursuing the Ph.D. degree with Xidian University, Xi'an, China. His current research interests include transient electromagnetic analysis.

Zhongchao Lin was born in Hubei, China, in 1988. He received the B.S. and Ph.D. degrees from Xidian University, Xi'an, China, in 2011 and 2016, respectively. He joined Xidian University, in 2016, as a Post Doctoral Fellow, where he was lately promoted as an Associate Professor. His research interests include large-scale computational electromagnetic, scattering, and radiation electromagnetic analysis.

Yu Zhang received the B.S., M.S., and Ph.D. degrees from Xidian University, Xi'an, China, in 1999, 2002, and 2004, respectively. In 2004, he joined Xidian University as a Faculty Member. He was a Visiting Scholar and an Adjunct Professor with Syracuse University, from 2006 to 2009. As a Principal Investigator, he works on projects, including the Project of NSFC. He has authored four books Parallel Computation in Electromagnetics (Xidian University Press, 2006), Parallel Solution of Integral Equation-Based EM Problems in the Frequency Domain (Wiley IEEE, 2009), Time and Frequency Domain Solutions of EM Problems Using Integral Equations and a Hybrid Methodology (Wiley, 2010), and Higher Order Basis Based Integral Equation Solver (Wiley, 2012), as well as more than 100 journal articles and 40 conference papers.

Xunwang Zhao was born in Shanxi, China, in 1983. He received the B.S. and Ph.D. degrees from Xidian University, Xi'an, China, in 2004 and 2008, respectively. He joined Xidian University, in 2008, as a Faculty Member, where he was lately promoted as a Full Professor. He was a Visiting Scholar with Syracuse University, Syracuse, NY, USA, from December 2008 to April 2009. As a Principal Inves tigator, he works on several projects, including the project of NSFC. His research interests include computational electromagnetic and electromagnetic scattering analysis.

Convolutional Neural Network for Coupling Matrix Extraction of Microwave Filters

Tarek Sallam[1,2] and Ahmed M. Attiya[3]

[1]School of Applied Technology
Qujing Normal University, Qujing, Yunnan, PR China 655011

[2]Faculty of Engineering at Shoubra, Benha University, Cairo, Egypt
tarek.sallam@feng.bu.edu.eg

[3]Microwave Engineering Dept., Electronics Research Institute (ERI), Cairo, Egypt
attiya@eri.sci.eg

***Abstract* –** Tuning a microwave filter is a challenging problem due to its complexity. Extracting coupling matrix from given *S*-parameters is essential for ?lter tuning and design. In this paper, a deep-learning-based neural network namely, a convolutional neural network (CNN) is proposed to extract coupling matrix from *S*-parameters of microwave filters. The training of the proposed CNN is based on a circuit model. In order to exhibit the robustness of the new technique, it is applied on 5- and 8-pole filters and compared with a shallow neural network namely, radial basis function neural network (RBFNN). The results reveal that the CNN can extract the coupling matrix of target *S*-parameters with high accuracy and speed.

***Index Terms* –** convolutional neural network, coupling matrix, deep learning, microwave filters, parameters extraction.

I. INTRODUCTION

Microwave filters are widely used in all types of electronic systems [1, 2]. Tuning of microwave filter is an inevitable process in the design procedure of microwave filters. For the case of coupled resonator filter, extracting of the coupling matrix from the required *S*-parameters can be viewed as an inverse problem for microwave filters.

Therefore, accurate solution of the inverse problem (extraction of coupling matrix) is crucial. However, it is extremely difficult to solve this inverse problem directly [3, 4]. Traditionally, the coupling matrix of the microwave filter is extracted by adopting the Cauchy method [5] or vector fitting [6]. However, these methods need to be repeated for many iterations in different conditions. Consequently, the process of filter design suffers from the time-consuming and complicated parameters extraction.

Neural network (NN) has been recognized as a powerful tool in microwave modeling and design [7–10]. Some conventional (shallow) NN techniques have been developed to extract the coupling matrix [11–13]. However, these techniques are not suitable for high-dimensional (many input variables) problems because data generation and model training become too complicated. A deep NN is applied to the parameter extraction of microwave filter [14]. However, there are too many layers in the deep NN, which make the training process complicated.

On the other hand, convolutional neural network (CNN) is a variant of deep network framework and achieves remarkable success on image and face recognition [15, 16]. Recently, it has gained much attention in the microwave field [17, 18]. It has unique capabilities of extracting underlying nonlinear features of input data. Two main advantages, sparse connectivity and shared weights, enable CNNs to have small numbers of parameters during learning and, hence, high training speed. Motivated by the inherent advantages of the CNN, it has been incorporated into coupling matrix extraction [19, 20].

In all the above NN methods, the training data is generated using full-wave electromagnetic (EM) model through simulation or measurement which becomes impractical when large training data is needed. Furthermore, the cost of training data generation increases exponentially with the number of input variables. Therefore, collection of training data using EM-based model to cover the interested input parameter range over a frequency band can be an overwhelmingly time-consuming task. Different from EM models, circuit models are used for all kinds of electronic designs. They are usually straightforward to build, and fast to evaluate.

In this paper, a CNN is used to extract the coupling matrix of ideal (target) *S*-parameters based on a

Submitted On: March 6, 2022
Accepted On: April 3, 2022

https://doi.org/10.13052/2022.ACES.J.370707

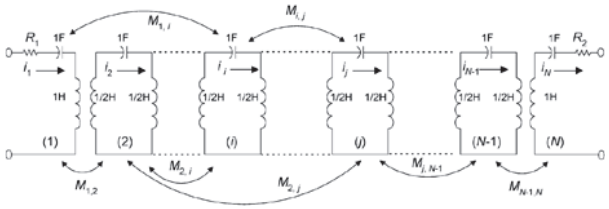

Fig. 1. Equivalent circuit of an N-coupled resonator filter [24].

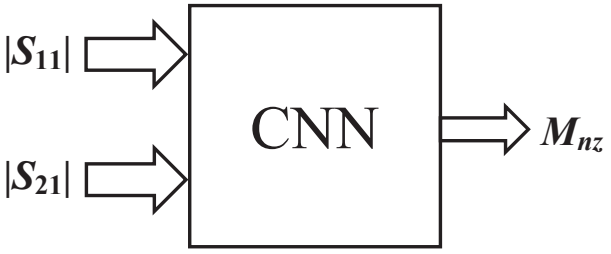

Fig. 2. The circuit model-based CNN for coupling matrix extraction.

circuit model. The CNN first extracts the features of S-parameters by using convolution layers and pooling layers, which are then mapped to the coupling matrix by full connection and output layers. To validate the effectiveness of the proposed CNN, it is applied on 5- and 8-pole microwave filters. The proposed CNN model is able to extract the coupling matrix of the ideal S-parameters with high accuracy and speed compared with a radial basis function neural network (RBFNN) [21–23] which is shallow (non-deep) NN.

II. CNN FOR CIRCUIT MODEL-BASED COUPLING MATRIX EXTRACTION

The circuit model-based equation that relates the coupling matrix $\mathbf{M}$ and filter S-parameters is given by [24]

$$S_{11} = 1 + 2jR_1[\gamma \mathrm{I} - j\mathrm{R} + \mathrm{M}]^{-1}_{11}$$
$$S_{21} = -2j\sqrt{R_1 R_2}[\gamma \mathrm{I} - j\mathrm{R} + \mathrm{M}]^{-1}_{N1}, \quad (1)$$

where $\gamma = (f_0/\mathrm{BW})((f/f_0) - (f_0/f))$, f, f_0, and BW are the frequency, filter center frequency, and filter bandwidth, respectively, N is the filter order, $\mathbf{I}$ is $N \times N$ identity matrix, $\mathbf{M}$ is the $N \times N$ symmetric coupling matrix, $\mathbf{R}$ is an $N \times N$ matrix with all entries being zero except $[\mathbf{R}]_{11} = R_1$ and $[\mathbf{R}]_{NN} = R_2$, and R_1 and R_2 are the filter's input and output coupling parameters, respectively, as shown in Fig. 1.

Figure 2 shows the CNN model for extracting the coupling matrix. The input to the CNN is the required vectors $|\boldsymbol{S}_{11}|$ and $|\boldsymbol{S}_{21}|$, representing the scalar magnitudes of the two S-parameters at $\mathscr{R}$ frequency points in the required frequency range. Therefore, the total number of inputs is $2\mathscr{R}$. In the present case, the number of the frequency points $\mathscr{R} = 2001$. The output of the CNN is the vector of *nonzero* coupling parameters $\boldsymbol{M}_{nz}$.

In order to generate the training and validation data of CNN, we assume a tolerance of ± 0.5 for every ideal nonzero coupling parameter. We then use 12,500 (10,000 for training and 2500 for validation) uniformly distributed random samples in this range for coupling parameters. For each sample of coupling parameters, eqn (1) is used to obtain the corresponding S-parameters. By swapping the data of coupling parameters and S-parameters, we can get the training and validation data for the coupling parameters extraction model. In the same way, the trained CNN is tested by the ideal set of S-parameters (corresponding to the ideal $\boldsymbol{M}_{nz}$ that is never used in the training), then the extracted $\boldsymbol{M}_{nz}$ is compared to the ideal one.

III. THE PROPOSED CNN STRUCTURE

CNNs have one or more convolutional and pooling layers to learn the discriminative features from the input data. After all the convolutional and pooling layers, these learned features are then aggregated to the vectors by the fully connected (FC) layers for the regression task [25].

After many simulation trials, it is found that the CNN structure that provides the best accuracy is detailed in Table 1. First, the total 4002 inputs are reshaped into a $2 \times 3 \times 667$ input image. Then, there are three convolutional (Conv) layers and three maximum pooling (MaxPool) layers. Each convolutional layer is followed by a pooling layer to reduce the dimension of network parameters. The first convolutional layer comprises eight feature maps. The number of feature maps at each convolutional layer is twice the previous layer, i.e., there are 16 and 32 feature maps in the second and third layers, respectively. The size of the feature map in each convolutional layer is fixed at 2×2. All convolutional layers have a stride of 1 and "same" padding. All pooling layers have a size of 2×2, stride 2, and "same" padding. After the sequence of convolutional and pooling layers, there is a single FC layer with 50 nodes followed by the output layer with a number of nodes equal to the number of nonzero coupling parameters. In order to avoid overfitting during training, a dropout operation with a rate of 50% is used at the end of the convolutional and pooling layers. The activation functions used in the convolutional layers and the FC layer are rectified linear unit (ReLU) and exponential linear unit (ELU), respectively. Since this is a regression problem instead of a classification problem, no activation is used at the output layer (linear activation).

Table 1: The proposed CNN structure

Layer	Size	Nodes	Stride	Padding	Activation
Input (image)	–	(2×3×667) = 4002	–	–	–
Conv1	2×2	8	1	Same	ReLU
MaxPool1		–	2		–
Conv2		16	1		ReLU
MaxPool2		–	2		–
Conv3		32	1		ReLU
MaxPool3		–	2		–
50% Dropout					
FC	–	50	–	–	ELU
Output	–	Length$\{\boldsymbol{M}_{nz}\}$	–	–	Linear

IV. EXAMPLES

To verify the performance of the CNN-based coupling matrix extraction, it is applied on 5- and 8-pole microwave filters. The Adam (adaptive momentum) optimization algorithm [26] is used to update the network weights and the loss function used for this network is the mean squared error. The initial value of the learning rate is 0.001. During the training, the learning rate is decreased by a rate of 0.1 each 40% of number of epochs. The batch size is 40 and number of epochs is 10. To further verify the performance of the CNN, it is compared to that of the RBFNN. Both NNs have the same number of inputs (4002) and outputs (Length$\{\boldsymbol{M}_{nz}\}$) as well as the same size of training and validation datasets (10,000 and 2500, respectively). In all examples, the filter's input and output coupling parameters are assumed to be equal, i.e., $R_1 = R_2$.

A. 5-Pole filter

In this example, we use the proposed CNN to develop a parameter-extraction model for a 5-pole dielectric resonator filter with a 3.4-GHz center frequency and a 54-MHz bandwidth [24]. The nonzero coupling parameters are $\boldsymbol{M}_{nz} = [R_1\ M_{12}\ M_{14}\ M_{23}\ M_{34}\ M_{45}]^T$ with their ideal values shown in Table 2. Table 2 also shows the extracted coupling values by RBFNN and CNN. It can be seen that the values of CNN are much closer to the ideal ones than those of RBFNN. The used shallow RBFNN has only one hidden layer with 300 neurons and cannot represent this high-dimensional input–output relationship effectively. Our proposed CNN modeling technique is suitable for this high-dimensional modeling problem.

Figure 3 shows the S-parameters corresponding to the coupling values in Table 2. As can be seen, there is a perfect agreement between the responses from the ideal and extracted coupling matrix of CNN compared with RBFNN, that is, owing to the capability of CNN to extract the hidden features in the input data, S-parameters, automatically. On the other hand, because the RBFNN is shallow, it cannot strengthen the network training process by reconstructing the input S-parameters.

Table 2: The ideal and extracted coupling values by RBFNN and CNN for a 5-pole filter

$\boldsymbol{M}_{nz}$	RBFNN	CNN	Ideal
R_1	1.1098	1.1345	1.1330
M_{12}	0.8138	0.8659	0.8660
M_{14}	−0.1450	−0.2525	−0.2520
M_{23}	0.7389	0.7942	0.7920
M_{34}	0.5287	0.5946	0.5950
M_{45}	0.8594	0.9006	0.9010

Table 3: The ideal and extracted coupling values by RBFNN and CNN for 8-pole filter

$\boldsymbol{M}_{nz}$	RBFNN	CNN	Ideal
R_1	1.2206	1.2415	1.2420
M_{12}	0.8977	0.9387	0.9380
M_{23}	0.5882	0.6300	0.6310
M_{27}	−0.0110	−0.0172	−0.0180
M_{34}	0.5313	0.5729	0.5760
M_{36}	0.0034	0.0637	0.0660
M_{45}	0.4549	0.5193	0.5190

B. 8-Pole filter

The second example involves the parameter-extraction of an 8-pole elliptic-function filter with 30-MHz bandwidth centered at 3 GHz [27]. The nonzero couplings are R_1, M_{12}, M_{23}, M_{27}, M_{34}, M_{36}, M_{45}, M_{56}, M_{67}, and M_{78}. However, the coupling matrix of this filter is dual-symmetrical meaning that it is symmetrical w.r.t. its anti-diagonal as well as its diagonal [28]. Therefore, $M_{12} = M_{78}$, $M_{23} = M_{67}$, and $M_{34} = M_{56}$. Consequently, the output of NNs is $\boldsymbol{M}_{nz} = [R_1\ M_{12}\ M_{23}\ M_{27}\ M_{34}\ M_{36}\ M_{45}]^T$. Table 3 shows the ideal as well as the extracted coupling values by both NNs with their corresponding S-parameters shown in Fig. 4.

According to Table 3 and Fig. 4, a very good match between the ideal and extracted coupling parameters by CNN along with an excellent agreement between the responses from the ideal and extracted coupling matrix by CNN have been achieved, compared to RBFNN. This again proves that the CNN is much more accurate than the RBFNN for coupling matrix extraction.

Table 4 shows the training time as well as the percentage root mean square error (RMSE) between ideal and extracted couplings by NNs for 5- and 8-pole filters. It can be seen that the CNN modeling for the extraction of coupling matrix is with much higher accuracy and shorter training time than the RBFNN modeling.

Table 4: Percentage RMSE and training time of RBFNN and CNN for 5- and 8-pole filters

NN	5-Pole filter		8-Pole filter	
	Training Time	*RMSE (%)*	*Training Time*	*RMSE (%)*
CNN	39 s	0.1413	38 s	0.2260
RBFNN	19.6 min	7.7997	17.7 min	6.3894

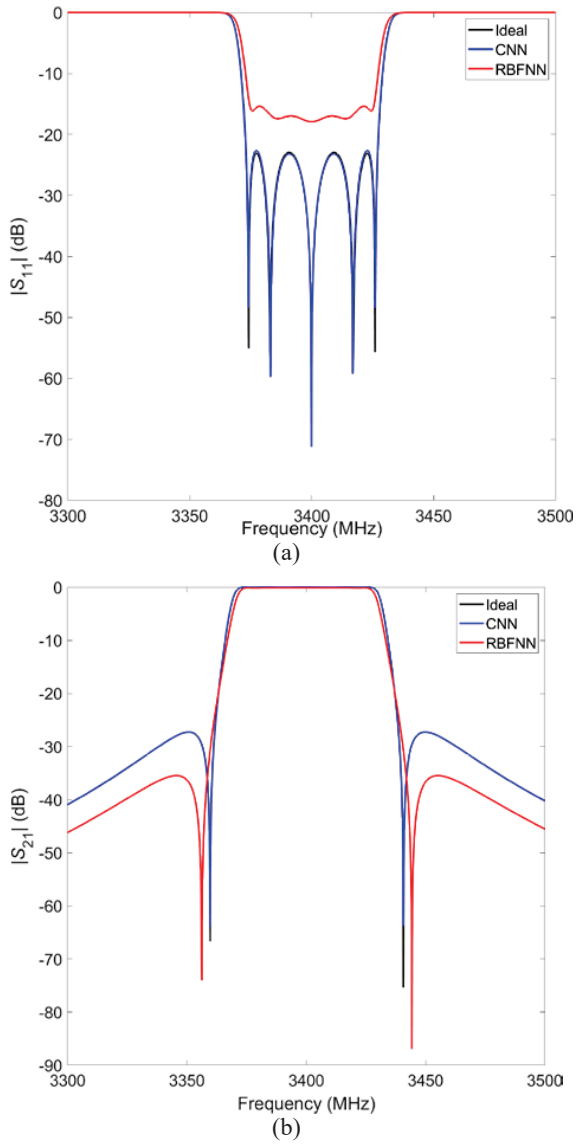

Fig. 3. The responses calculated by the coupling values in Table 2: (a) Return loss and (b) insertion loss.

Moreover, our proposed circuit model-based CNN can provide parameter-extraction solutions instantly, while the full-wave EM model-based methods can take hours to extract the solutions by repetitively simulating/measuring the filter during optimization iterations.

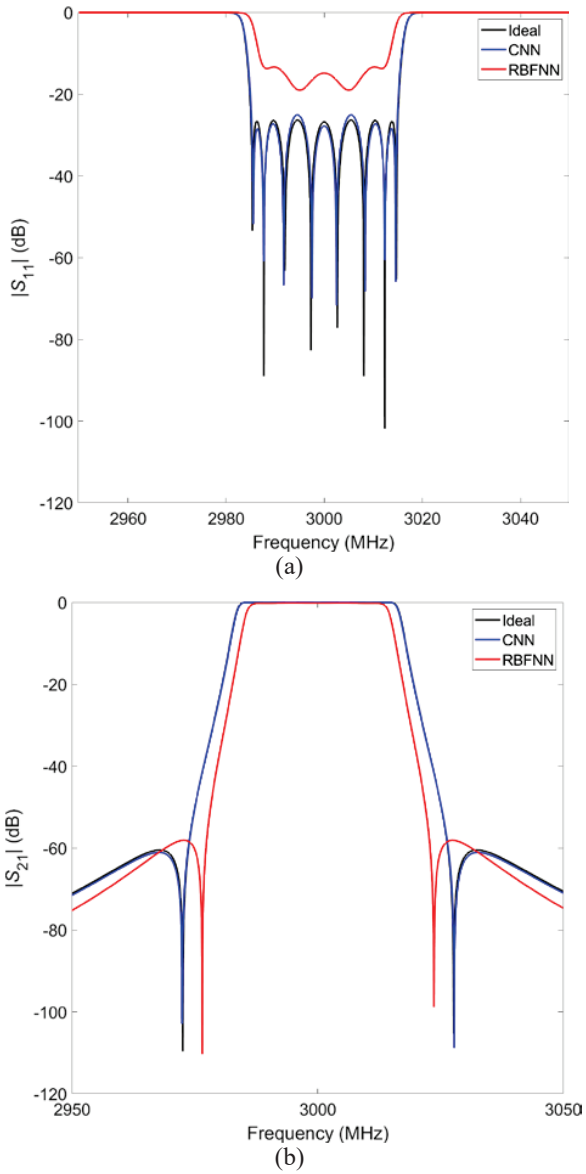

Fig. 4. The responses calculated by the coupling values in Table 3: (a) Return loss and (b) insertion loss.

V. CONCLUSION

A circuit model-based CNN is proposed to extract coupling matrix from *S*-parameters. The results show that the proposed CNN method can be used reliably to perform the parameter extraction for microwave filters. Compared to the shallow NN, the deep-learning-based CNN is much more accurate and faster in extracting the coupling parameters. Unlike the full-wave EM model-based methods, our proposed CNN model does not need to simulate and/or measure the filter iteratively. Once the CNN model is developed, it can be used to quickly extract the coupling parameters of microwave filters.

REFERENCES

[1] R. J. Cameron, C. M. Kudsia, and R. T. Mansour, *Microwave Filters for Systems: Fundamentals, Design and Applications*. Hoboken, NJ, USA, Wiley, 2018.

[2] S. Saleh, W. Ismail, I. S. Z. Abidin, and M. H. Jamaluddin, "Compact 5G Hairpin bandpass filter using non-uniform transmission lines theory," *Applied Computational Electromagnetic Society (ACES) Journal*, vol. 36, no. 2, pp. 126-131, Feb. 2021.

[3] L. Accatino, "Computer-aided tuning of microwave filters," in *IEEE MTT-S Int. Microw. Symp. Dig*., pp. 249-252, Jun. 1986.

[4] M. Yu and W. C. Tang, "A fully automated filter tuning robots *for* wireless base station diplexers," in *Proc. Workshop, Comput. Aided Filter Tuning, IEEE Int. Microw. Symp*., Philadelphia, PA, USA, pp. 8-13, Jun. 2003.

[5] G. Macchiarella and D. Traina, "A formulation of the Cauchy method *suitable* for the synthesis of lossless circuit models of microwave filters from Lossy measurements," *IEEE Microw. Wireless Compon. Lett*., vol. 16, no. 5, pp. 243-245, May 2006.

[6] C.-K. Liao, C.-Y. Chang, and J. Lin, "A vector-fitting formulation for parameter extraction of lossy microwave filters," *IEEE Microw. Wireless Compon. Lett*., vol. 17, no. 4, pp. 277-279, Apr. 2007.

[7] Q.-J. Zhang, K. C. Gupta, and V. K. Devabhaktuni, "Artificial neural *networks* for RF and microwave design-From theory to practice," *IEEE Trans. Microw. Theory Techn*., vol. 51, no. 4, pp. 1339-1350, Apr. 2003.

[8] H. Kabir, L. Zhang, M. Yu, P. H. Aaen, J. Wood, and Q.-J. Zhang, "*Smart* modeling of microwave devices," *IEEE Microw. Mag*., vol. 11, no. 3, pp. 105-118, May 2010.

[9] Z. S. Tabatabaeian and M. H. Neshati, "Design investigation of an X-band SIW H-plane band pass filter with improved stop band using neural network optimization," *Applied Computational Electromagnetic Society (ACES) Journal*, vol. 30, no. 10, pp. 1083-1088, Aug. 2021.

[10] Z. S. Tabatabaeian and M. H. Neshati, "Development of a low profile and wideband backward-wave directional coupler using neural network," *Applied Computational Electromagnetic Society (ACES) Journal*, vol. 31, no. 12, pp. 1404-1409, Aug. 2021.

[11] H. Kabir, Y. Wang, M. Yu, and Q. J. Zhang, "High dimensional neural network techniques and applications to microwave filter modeling," *IEEE Trans. Microwave Theory Tech*., vol. 58, no. 1, pp. 145-156, Jan. 2010.

[12] C. Zhang, J. Jin, W. Na, Q. -J. Zhang, and M. Yu, "Multivalued neural network inverse modeling and applications to microwave filters," *IEEE Trans. Microwave Theory Tech*., vol. 66, no. 8, pp. 3781-3797, Aug. 2018.

[13] J. -J. Sun, X. Yu, and S. Sun, "Coupling matrix extraction for microwave filter design using neural networks," *2018 IEEE International Conference on Computational Electromagnetics (ICCEM)*, pp. 1-2, 2018.

[14] J. Jin, F. Feng, W. Zhang, J. Zhang, Z. Zhao, and Q. -J. Zhang, "Recent advances in deep neural network technique for high-dimensional microwave modeling," *2020 IEEE MTT-S International Conference on Numerical Electromagnetic and Multiphysics Modeling and Optimization (NEMO)*, pp. 1-3, 2020.

[15] J. Fu, H. Zheng, and T. Mei, "Look closer to see better: recurrent attention convolutional neural network for fine-grained image recognition," *IEEE Conference on Computer Vision and Pattern Recognition (CVPR)*, Honolulu, HI, USA, pp. 4476-4484, Jul. 2017.

[16] T. H. Kim, C. Yu, and S. W. Lee, "Facial expression recognition using feature additive pooling and progressive fine-tuning of CNN," *Electron. Lett*., vol. 54, no. 23, pp. 1326-1327, 2018.

[17] Y. Wang, Z. Zhang, Y. Yi, and Y. Zhang, "Accurate microwave filter design based on particle swarm optimization and one-dimensional convolution autoencoders," *Int J RF Microw Comput Aided Eng.*, vol. 32, no. 4, 2022.

[18] H. Arab, I. Ghaffari, L. Chioukh, S. O. Tatu, and S. Dufour, "A Convolutional neural network for human motion recognition and classification using a millimeter-wave doppler radar," *IEEE Sensors Journal*, vol. 22, no. 5, pp. 4494-4502, Mar. 2022.

[19] J. J. Sun, S. Sun, X. Yu, Y. P. Chen, and J. Hu, "A deep neural network based tuning technique of lossy microwave coupled resonator filters," *Microw. Opt. Technol. Lett*., vol. 61, no. 9, pp. 2169-2173, 2019.

[20] Y. Zhang, Y. Wang, Y. Yi, J. Wang, J. Liu, and Z. Chen, "Coupling matrix extraction of microwave filters by using one-dimensional convolutional autoencoders," *Front. Phys*., vol. 9, Nov. 2021.

[21] T. Sallam, A. B. Abdel-Rahman, M. Alghoniemy, Z. Kawasaki, and T. Ushio, "A Neural-network-based beamformer for phased array weather radar," *IEEE Transactions on Geoscience and Remote Sensing*, vol. 54, no. 9, pp. 5095-5104, Sept. 2016.

[22] T. Sallam, A. B. Abdel-Rahman, M. Alghoniemy, and Z. Kawasaki, "A novel approach to the recovery of aperture distribution of phased arrays with single RF channel using neural networks," *2014 Asia-Pacific Microwave Conference*, Sendai, Japan, pp. 879-881, 2014.

[23] X. Jia, Q. Ouyang, T. Zhang, and X. Zhang, "A novel adaptive tracking algorithm for the resonant

frequency of EMATs in high temperature," *Applied Computational Electromagnetic Society (ACES) Journal*, vol. 33, no. 11, pp. 1243-1249, Jul. 2021.

[24] M. A. Ismail, D. Smith, A. Panariello, Y. Wang, and M. Yu, "EM-based design of large-scale dielectric-resonator filters and multiplexers by space mapping," *IEEE Trans. Microw. Theory Tech*., vol. 52, no. 1, pp. 386-392, Jan. 2004.

[25] T. Sallam and A. M. Attiya, "Convolutional neural network for 2D adaptive beamforming of phased array antennas with robustness to array imperfections," *International Journal of Microwave and Wireless Technologies*, vol. 13, no. 10, pp. 1096-1102, Dec. 2021.

[26] D. P. Kingma and J. Ba, "Adam: a method for stochastic optimization," *Proc. of the 3rd Int. Conf. on Learning Representations (ICLR)*, San Diego, CA, USA, 2015.

[27] H.-T. Hsu, Z. Zhang, K. A. Zaki, and A. E. Ati, "Parameter extraction for symmetric coupled-resonator filters," *IEEE Trans. Microw. Theory Techn*., vol. 50, no. 12, pp. 2971-2978, Dec. 2002.

[28] J. W. Bandler, S. H. Chen, and S. Daijavad, "Exact sensitivity analysis for the optimization of coupled cavity filters," *J. Circuit Theory Applicat*., vol. 31, pp. 63-77, 1986.

Tarek Sallam was born in Cairo, Egypt, in 1982. He received the B.S. degree in electronics and telecommunications engineering and the M.S. degree in engineering mathematics from Benha University, Cairo, Egypt, in 2004 and 2011, respectively, and the Ph.D. degree in electronics and communications engineering from Egypt-Japan University of Science and Technology (E-JUST), Alexandria, Egypt, in 2015. In 2006, he joined the Faculty of Engineering at Shoubra, Benha University. In 2019, he joined the Faculty of Electronic and Information Engineering, Huaiyin Institute of Technology, Huai'an, Jiangsu, China. In 2022, he joined the School of Applied Technology, Qujing Normal University, Qujing, Yunnan, China, where he is currently an Associate Professor. He was a Visiting Researcher with the Electromagnetic Compatibility Lab, Osaka University, Osaka, Japan, from August 2014 to May 2015. His research interests include evolutionary optimization, neural networks and deep learning, phased array antennas with array signal processing and adaptive beamforming.

Ahmed M. Attiya received the M.Sc. and Ph.D. degrees in electronics and electrical communications from the Faculty of Engineering, Cairo University, Cairo, Egypt, in 1996 and 2001, respectively. He joined the Electronics Research Institute as a Researcher Assistant in 1991. In the period from 2002 to 2004, he was a Postdoc with the Bradley Department of Electrical and Computer Engineering, Virginia Tech. In the period from 2004 to 2005, he was a Visiting Scholar with Electrical Engineering Department, University of Mississippi. In the period from 2008 to 2012, he was a Visiting Teaching Member with King Saud University. He is currently a Full Professor and the Head of Microwave Engineering Department, Electronics Research Institute. He is also the Founder of Nanotechnology Lab., Electronics Research Institute.

Obtaining Feasible Minimum Side Lobe Level for Narrow Beam Width Using Convex Optimization in Linear, Planar, and Random Antenna Arrays

Rana R. Shaker and Jafar R. Mohammed

Department of Communication Engineering
College of Electronic Engineering, Ninevah University, Mosul-41002, Iraq
rana.raad2021@stu.uoninevah.edu.iq
jafar.mohammed@uoninevah.edu.iq

Abstract – In many applications, the radiating elements of the used antenna may be configured in the form of a one-dimensional linear array, or two-dimensional planar array or even random array. In such applications, a simple optimization algorithm is highly needed to optimally determine the excitation amplitudes and phases of the array elements to maximize the system's performance. This paper uses a convex optimization instead of other complex global stochastic optimizations to synthesize a linear, planar, and random array patterns under prespecified constraint conditions. These constraints could be either fixed beam width with the lowest possible sidelobe levels or fixed sidelobe level with narrower possible beam width. Two approaches for array pattern optimization have been considered. The first one deals with the problem of obtaining a feasible minimum sidelobe level for a given beam width, while the second one tries to obtain a feasible minimum beam width pattern for a given sidelobe level. Both optimization approaches were applied to the linear, planar, and random arrays. Simulation results verified the effectiveness of both optimization approaches and for all considered array configurations.

Index Terms – beam width minimization, convex optimization, linear array, planar array, random array, sidelobe level minimization.

I. INTRODUCTION

In most antenna array applications, low sidelobe levels with narrow beam width patterns (i.e., maximum directivities) are critical to minimize the undesirable effects of the interfering and noise signals that may cause false target indications and degrade the overall system performance. Generally, the radiating elements of the antenna arrays can be arranged as a one-dimensional linear array, two-dimensional planar array, or even random array configurations. In the linear and planar arrays, the inter-element spacing is usually regular and uniform, while in the random arrays they are irregular and non-uniform. Unlike the linear arrays where their radiation patterns can be scanned either on the azimuth or elevation angles, the radiation patterns of the planar arrays can be simultaneously scanned to any angle in the azimuth and elevation planes. Thus, planar arrays are most widely used in practice due to their advantages and versatility [1].

The regularly spaced and uniformly excited linear and planar arrays have many good radiation characteristics such as narrow beam width, good directivity, and simple excitation weight vector, but they suffer from high sidelobe levels (SLLs) which are about -13.2 dB. Such high SLLs may cause many problems with false target indications. Usually, the beamwidth, sidelobe level, and many other array pattern characteristics can be controlled by adjusting one or more of the following array design parameters; geometrical layout of the array elements, the excitation phases, and amplitudes of the array elements, inter-element spacing, and the elementary pattern of each element [2]. In this work, the excitation amplitudes and phases were used to design the linear and the planar arrays. Whereas in the random arrays, first the inter-element spacing is determined randomly, then, the excitation amplitudes and phases of the random elements were optimized to get the required array pattern.

In the literature, many researchers have studied these design parameters and found that the SLL can be reduced by tapering the excitation amplitudes of the array elements. Therefore, many tapers based on deterministic approaches have been suggested such as Dolph, Taylor, triangular, and raised cosine, to name just a few [2, 3]. Specifically, the Dolph-Tschebyscheff approach suggested a certain distribution for the element excitations such that the corresponding array pattern has a minimum widening factor in the beam width for a given sidelobe level. In other words, as the beam width decreases, the side lobe level increases and vice versa. Although these tapering methods successfully reduced the sidelobe levels, these good results came at the cost of widening the beam width. Thus, there was always a trade-off between the required sidelobe level and the desired beam width pattern [4].

Submitted On: April 30, 2022
Accepted On: October 6, 2022
https://doi.org/10.13052/2022.ACES.J.370708

In an attempt to maintain the beam width unchanged while reducing the sidelobe levels, several simple analytical and numerical methods were presented in [5–7] where the excitation amplitudes and phases of just two side elements in the linear array were controlled. Then, the method was further extended to the planar arrays where the excitation amplitudes and phases of the boundary elements were modified to achieve the required radiation pattern [8].

On the other hand, many optimization techniques such as genetic algorithm [9], particle swarm optimization [10], simulated annealing [11], differential evolution algorithm [12], and others [13] have been also used for array synthesis. However, the computational complexity of these globally optimized methods is high, especially when dealing with relatively large arrays.

Interestingly, the problem of the array synthesis with a feasible minimum sidelobe level for a given beam width or vice versa can be successfully solved by using convex optimization methods. First, by converting the problem into convex, then the optimal solution becomes much easier and faster than that of other global optimization methods. In fact, many array synthesis scenarios are convex in nature and they can be simply solved without recalling other complex optimization methods such as genetic algorithms [14, 15] or Modified Seagull optimization [16, 17].

In this paper, the convex optimization [18] was applied to the linear, planar, and random arrays to obtain the desired radiation patterns where the excitation amplitude and phase of the individual array elements are optimized. To proceed with the optimization process, two constraint strategies were suggested. The first one includes the finding of the feasible minimum sidelobe level for a given beam width pattern, while the other one includes the finding of the feasible minimum beam width pattern for a given sidelobe level. The effectiveness of both strategies in designing linear, planar, and random arrays was fully illustrated and verified.

II. THE CONVEX OPTIMIZED METHOD

A regularly spaced two-dimensional rectangular planar array composed of N rows and M columns of isotropic radiating elements are considered. The elements are distributed uniformly on the xy plane with separation distances $d_x = \frac{\lambda}{2}$ and $d_y = \frac{\lambda}{2}$ in the x and y directions, respectively. For uniformly spaced linear arrays, the array size will be either $N \times 1$ or $M \times 1$ according to the considered axis. In general, the array factor of two-dimensional elements can be given by:

$$AF(\theta,\phi) = \sum_{n=1}^{N}\sum_{m=1}^{M} w_{nm} \; e^{j\frac{2\pi}{\lambda}[(n-1)(d_x sin\ \theta\ cos\ \phi+\beta_x)+(m-1)(d_y sin\theta\, sin\phi+\beta_y)]}, \quad (1)$$

where λ is the wavelength at the operating frequency, θ and ϕ are the elevation and azimuth angles, respectively, and $\beta_x = -\frac{2\pi}{\lambda} d_x sin(\theta_0) cos(\phi_0)$, $\beta_y = -\frac{2\pi}{\lambda} d_y sin(\theta_0) sin(\phi_0)$ are the progressive phase shifts in the x and y directions, respectively. θ_0 and ϕ_0 are the steered angles. Finally, w_{nm} represents the amplitude and phase excitations of the (n,m) element.

For random arrays, the elements are randomly located along the x and y-axes and the inter-element spacing is irregular. Thus, (1) can be rewritten as:

$$AF(\theta,\phi) = \sum_{n=1}^{N}\sum_{m=1}^{M} w_{nm} \; e^{j\frac{2\pi}{\lambda}[(n-1)(x_{n,m} sin\ \theta\ cos\ \phi+\beta_x)+(m-1)(y_{n,m}\ sin\theta\ sin\ \phi+\beta_y)]}, \quad (2)$$

where $x_{n,m}$ and $y_{n,m}$ are the random locations of the (n,m) element. From (1) and (2), it is clear that the total number of adjustable excitation elements, w_{nm}, is $N \times M$ which is quite large, especially for large arrays. Thus, the uses of global stochastic optimizations such as genetic algorithms are associated with high complexity and slow convergence. Further, in many cases, the optimal solution may not require such a highly complex-global optimization algorithm since the searching space may be convex. Therefore, such problem can be solved efficiently by the convex optimization where the unknown array excitations, w_{nm}, constitutes a set of linear functions on a convex space.

The convex optimization problem is formulated as the determination of the excitation amplitudes and phases of the array elements such that the resulting radiation pattern satisfies one of the following two cases.

Case 1: Obtaining feasible minimum sidelobe level for a given beam width

In this case, the convex optimization minimizes the sidelobe level outside the beamwidth of the array pattern and it has unit sensitivity at the target direction to avoid any distortion in the main beam peak. These constraints are written as follows:

$$|AF(\theta,\phi)| \ \ is\ minimum, \quad (3)$$

Subject to:

$$AF\left(\beta_x,\beta_y\right) = 1, \quad (4)$$

$$|AF(\theta_i,\phi_i)| \le SLL, \ \ -90^o \le \theta_i \le -\Omega_{BW}\ and \ \ \Omega_{BW} \le \theta_i \le 90^o, \quad (5)$$

where SLL is the feasible starting value of the sidelobe level in the elevation plane for a fixed value of azimuth angle, and Ω_{BW} is the required first null to null beam width in the elevation plane. The constraint in (4) aims at preserving the unit gain in the target direction, while the constraint in (5) is for obtaining the feasible minimum sidelobe level for a given beam width pattern.

Case 2: Obtaining minimum beam width pattern for a given sidelobe level

In this case, the optimized array pattern is designed such that it has unit sensitivity at the desired target direction, satisfies the constraint on the sidelobe level outside the main beam, and minimizes the beamwidth of the array pattern. The results of applying these two cases are shown in the following section.

III. SIMULATION RESULTS

In this section, many examples are presented and investigated by means of computer simulations to assess the performance of the described optimization methods. Matlab software has been used to obtain the results. In the first example, a uniformly spaced linear array with a total number of elements equal to 36 (i.e., N=36 and M=1) spaced by $\frac{\lambda}{2}$ is considered. The required first null to null beam width (FNBW) of the optimized array pattern was chosen to be equal to that of the standard uniformly excited linear array with 36 elements which is 5°, ($\Omega_{BW} = 5^o$). Note that the FNBW of the optimized array is restricted to be as narrow as that of the standard uniformly excited linear array while solving for the feasible minimum sidelobe level. The target direction is assumed to be known and equals 0°. In this case, the excitation amplitudes and phases are optimized such that the corresponding array factor complies with the imposed constraints according to (3), (4), and (5). Figure 1 shows the radiation pattern of the optimized linear array and its element locations. For comparison purposes, the radiation pattern of the standard uniformly excited linear array is also shown in this figure. From this figure, it is found that the FNBW of the optimized array is exactly equal to that of the standard uniformly excited linear array, and the feasible minimum sidelobe level was −31.8 dB which is much lower than that of the standard uniformly excited linear array, −13.2 dB. The optimized excitation amplitudes and phases are shown in Fig. 2.

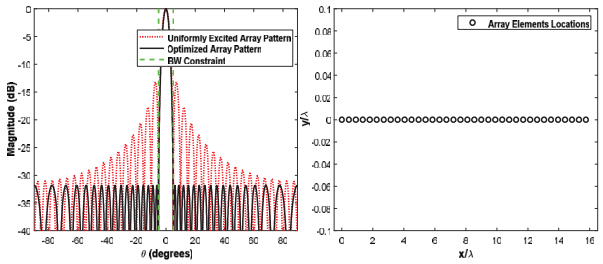

Fig. 1. Optimized pattern of the linear array with 36×1 elements for Ω_{BW}=5° (left) and its element locations (right).

In the second example, a uniformly spaced planar array with $N \times M = 6 \times 6$ elements is considered. Note

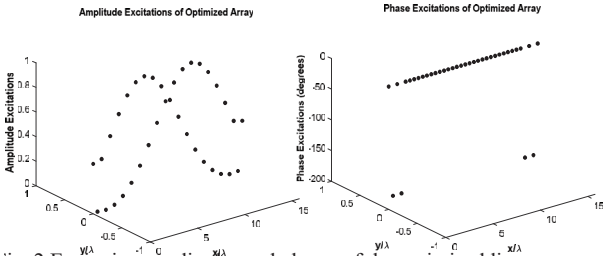

Fig. 2. Excitation amplitudes and phases of the optimized linear array whose pattern is shown in Fig. 1.

that the total number of the array elements in all array configurations (linear, planar, and random) was fixed to 36 elements. Again, the same optimization constraints as in the previous example were imposed to obtain the feasible minimum sidelobe level for a given narrow beam width, $\Omega_{BW} = 5^o$. The pattern of the optimized planar array and its element locations are shown in Fig. 3, whereas the excitation amplitudes and phases are shown in Fig. 4. In this case, the feasible minimum SLL was −8 dB which is higher than that of the standard uniformly excited linear array, −13.2 dB. Nevertheless, much lower SLL can be obtained for larger values of beam widths.

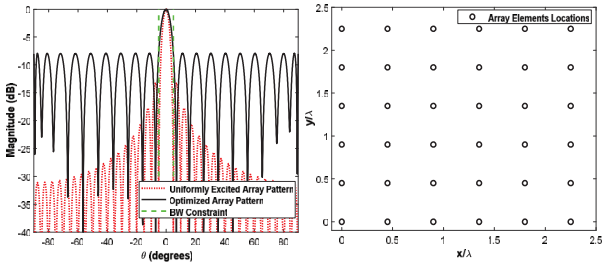

Fig. 3. Optimized pattern of the planar array with 6×6 elements for $\Omega_{BW} = 5^\circ$ (left) and its element locations (right).

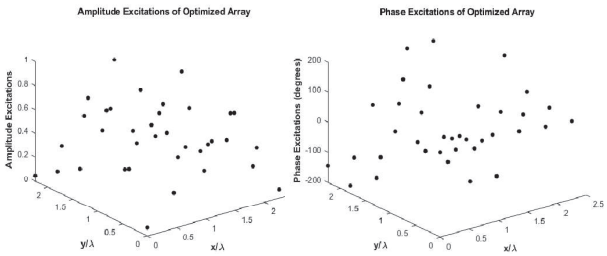

Fig. 4. Excitation amplitudes and phases of the optimized planar array whose radiation pattern is shown in Fig. 3.

In the third example, a randomly spaced planar array with $N \times M = 6 \times 6$ elements is considered. Again, the

beam width constraint was $\Omega_{BW} = 5^o$as in the previous examples. The results for the optimized random array are shown in Fig. 5. From this figure, it can be seen that the feasible minimum sidelobe level was -7.7 dB which is also higher than that of the standard uniformly excited linear array, -13.2 dB. Nevertheless, much lower SLL can be obtained for wider beam width as shown in Fig. 6 (a) where the beam width was varied from $\Omega_{BW} = 3^o$ to $\Omega_{BW} = 20^o$ and the corresponding feasible minimum SLL was recorded. For these values of beam widths, the directivities of the three array configurations were also plotted as shown in Fig. 6 (b). From these two figures, it can be seen that the linear array gives the feasible minimum SLL and higher directivity. This is mainly because the linear array configuration has wider space diversity than the planar and random arrays, thus, narrower beam width and better directivity can be achieved. Moreover, the feasible minimum SLL can be significantly reduced with an increase in the given

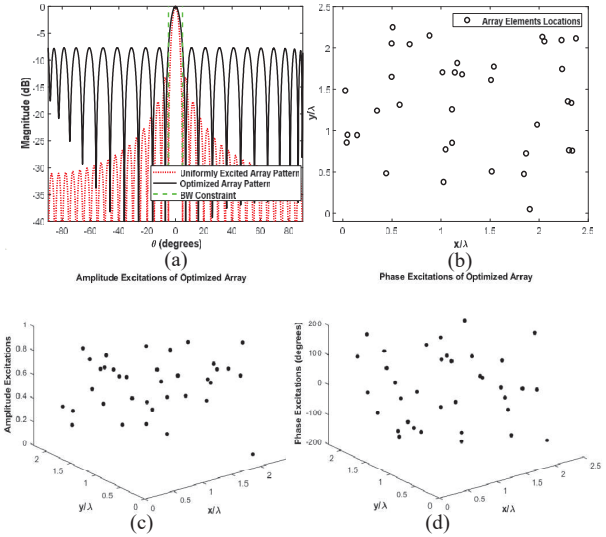

Fig. 5. (a) Optimized pattern of the random array with 6×6 elements for $\Omega_{BW} = 5°$, (b) its element locations, (c) excitation amplitudes, and (d) phases.

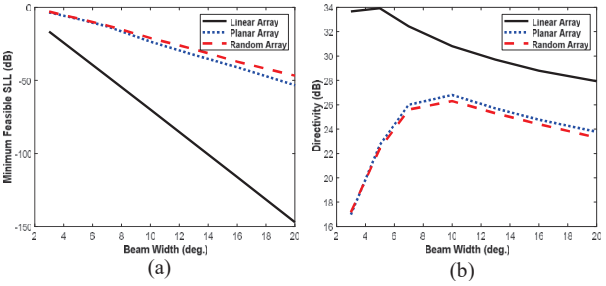

Fig. 6. (a) Variation of minimum SLL and (b) directivity.

In the next example, a feasible minimum beam width pattern for a given SLL is investigated where the SLL was fixed at -30 dB, and a feasible minimum beam width for linear, planar, and random arrays was computed as shown in Fig. 7 to Fig. 9. From these figures, it can be seen that the feasible minimum beam width for linear, planar, and random arrays was $\Omega_{BW} = 4^o$, $\Omega_{BW} = 11^o$, and $\Omega_{BW} = 11^o$ respectively for given SLL = -30 dB.

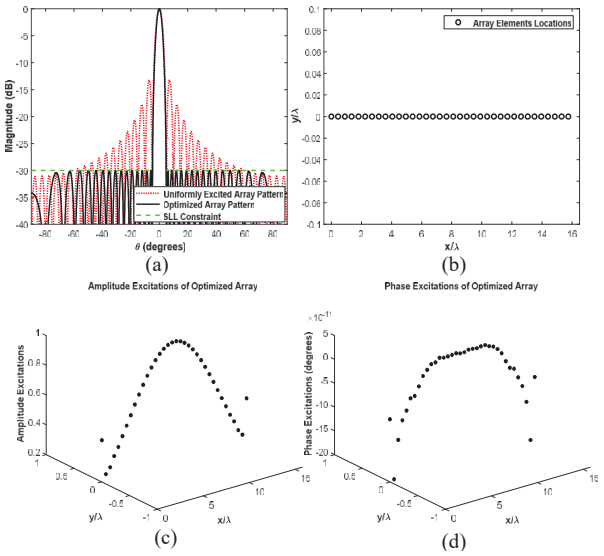

Fig. 7. (a) Optimized pattern of the linear array with 36×1 elements for SLL = -30 dB, (b) its element locations, (c) excitation amplitudes, and (d) phases.

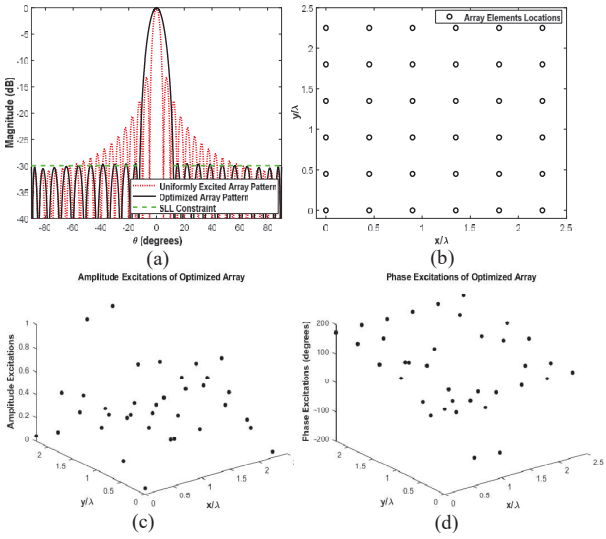

Fig. 8. (a) Optimized pattern of the linear array with 6×6 elements for SLL = -30 dB, (b) its element locations, (c) excitation amplitudes, and (d) phases.

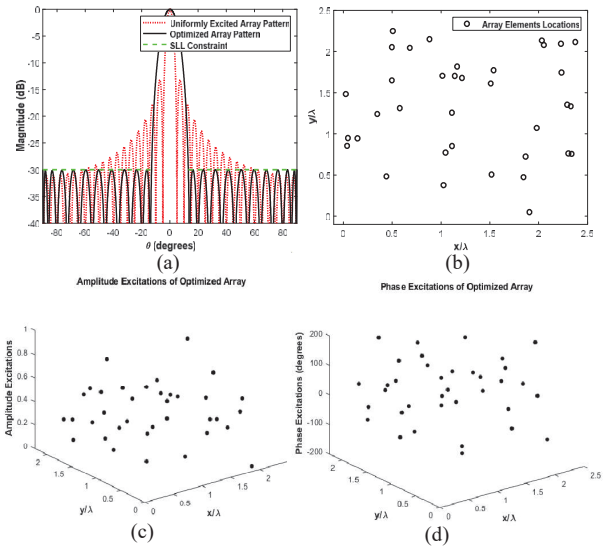

Fig. 9. (a) Optimized pattern of the random array with 6×6 elements for SLL = −30 dB, (b) its element locations, (c) excitation amplitudes, and (d) phases.

Finally, Fig. 10 shows the variations of the minimum feasible beam width and the directivities for different values of the given SLL. It can be seen that the higher SLL results in a narrower beam width. These results fully confirm the effectiveness of the convex optimization algorithm for designing linear, planar, and random arrays.

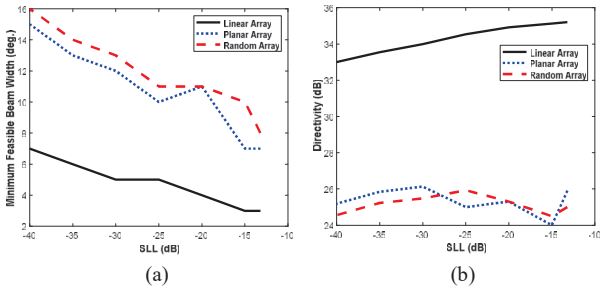

Fig. 10. (a) Variation of minimum SLL and (b) directivity.

IV. CONCLUSION

Convex optimization has been used effectively to obtain the desired radiation patterns of the linear, planar, and random arrays by optimizing the excitation amplitudes and phases of the array elements subject to either finding the minimum possible sidelobe level for a given beam width pattern or finding the minimum possible beam width for a given sidelobe level. From the results of the linear, planar, and random array configurations, it has been shown that a much lower SLL can be obtained for higher beam width values at the cost of lower directivities. Moreover, the performance of the linear arrays was found to outperform in terms of minimum feasible SLL for a given narrow beam width compared to the other two configurations. This is mainly due to the linear array has wider space diversity. On the other hand, the three array configurations perform well and provide feasible minimum beam width for relatively high SLL. These results fully confirm the capability of the suggested two optimization constraint methods.

REFERENCES

[1] J. R. Mohammed, "Performance optimization of the arbitrary arrays with randomly distributed elements for wireless sensor networks," *International Journal of Telecommunication, Electronics, and Computer Engineering*, vol. 11, no. 4, pp. 63-68, 2019.

[2] C. A. Balanis, *Antenna Theory: Analysis and Design*, 4th ed., Wiley, 2016.

[3] J. R. Mohammed and K. H. Sayidmarie, "Sensitivity of the adaptive nulling to random errors in amplitude and phase excitations in array elements," *International Journal of Telecommunication, Electronics, and Computer Engineering*, vol. 10, no. 1, pp. 51-56, 2018.

[4] P. Daniele, "On the trade-off between the main parameters of planar antenna arrays," *Electronics*, vol. 9, 2020.

[5] J. R. Mohammed and K. H. Sayidmarie, "Synthesizing asymmetric sidelobe pattern with steered nulling in non-uniformly excited linear arrays by controlling edge elements," *International Journal of Antennas and Propagation*, vol. 2017, 2017.

[6] J. R. Mohammed, "Obtaining wide steered nulls in linear array patterns by controlling the locations of two edge elements," *AEÜ International Journal of Electronics and Communications*, vol. 101, pp. 145-151, 2019.

[7] J. R. Mohammed, "Optimal null steering method in uniformly excited equally spaced linear array by optimizing two edge elements," *Electronics Letters*, vol. 53, no. 13, pp.835-837, 2017.

[8] J. R. Mohammed, "Element selection for optimized multi-wide nulls in almost uniformly excited arrays," *IEEE Antennas and Wireless Propagation Letters*, vol. 17, no. 4, pp. 629-632, 2018.

[9] J. R. Mohammed and K. H. Sayidmarie, "Sidelobe cancellation for uniformly excited planar array antennas by controlling the side elements," *IEEE Antennas and Wireless Propagation Letters*, vol. 13, pp. 987-990, 2014.

[10] L. Wen-Pin and C. Fu-Lai, "Null steering in planar array by controlling only current amplitudes

using genetic algorithms," *Microwave and Optical Technology Letters*, vol. 16, no. 2, pp. 97-103, 1997.

[11] J. Robinson and Y. Rahmat-Samii, "Particle swarm optimization in electromagnetics," *IEEE Trans. Antennas Propag.*, vol. 52, no. 2, pp. 397-407, 2004.

[12] M. Raíndo-Vázquez, A. Salas-Sánchez, J. Rodríguez-González, M. López-Martín, and F. Ares-Pena, "Optimizing radiation patterns of thinned arrays with deep nulls fixed through their representation in the schelkunoff unit circle and a simulated annealing algorithm, *Sensors*, vol. 22, 2022. https://doi.org/10.3390/s22030893.

[13] E. Aksoy and E. Afacan, "Planar antenna pattern nulling using differential evolution algorithm," *AEU Int. J. Electron. Commun.*, vol. 63, pp. 116-122, 2009.

[14] A. Akdagli, K. Guney, and D. Karaboga, "Touring ant colony optimization algorithm for shaped-beam pattern synthesis of linear antenna," *Electromagnetics*, vol. 26, no. 8, pp. 615-628, 2006.

[15] Y. Qu, G.S. Liao, S. Q. Zhu, and X.Y. Liu, "Pattern synthesis of planar antenna array via convex optimization for airborne forward looking radar," *Progress in Electromagnetics Research*, vol. 84, pp. 1-10, 2008.

[16] O. M. Bucci, M. D'Urso, and T. Isernia, "Exploiting convexity in array antenna synthesis problems," *IEEE Radar Conference*, Rome, Italy, pp. 1-6, 2008. doi: 10.1109/RADAR.2008.4720832.

[17] E. Kurt, S. Basbug, and K. Guney. "Linear antenna array synthesis by modified seagull optimization algorithm," *Applied Computational Electromagnetics Society (ACES) Journal*, vol. 36, no. 12, pp. 1552-1562, 2022.

[18] A. Z. Elsherbeni and M. J. Inman, "Antenna design and radiation pattern", *Applied Computational Electromagnetics Society (ACES) Journal*, vol. 18, no. 3, pp. 26-32, Jun. 2022.

Jafar R. Mohammed received B.Sc. and M.Sc. Degrees in Electronics and Communication Engineering in 1998 and 2001, respectively, and a Ph.D. degree in Digital Communication Engineering in Nov. 2009. He was a visiting lecturer in the faculty of Electronics and Computer Engineering at the Malaysia Technical University Melaka (UTeM), Melaka, Malaysia in 2011 and the Autonoma University of Madrid, Spain in 2013. He is currently a Professor and Vice Chancellor for Scientific Affairs at Ninevah University, Mosul, Iraq. He authored more than 70 papers in international refereed journals and conference proceedings. Also, he edited the book titled "Array Pattern Optimization" published by IntechOpen in 2019. His main research interests are in the area of Digital Signal Processing and its applications, Antenna, and Adaptive Arrays. In 2011, He is listed in Marquis, Who's Who in Science and Engineering (Edition 28). In 2018, he has been selected for the Marquis Who's Who Lifetime Achievement Award.

Rana R. Shaker received a B.Sc. degree in Communication Engineering from College of Electronic Engineering, Ninevah University. She is currently pursuing her Master's degree at the same university. Her research interests include antenna arrays and array pattern optimization.

Temperature Effects Analysis on Microwave Rectifiers by Field-Circuit Hybrid Multiphysics Simulation

Hongzheng Zeng[1], Yaqing Chen[1], Chao Zhou[1], Yuzhu Tang[2], and Xing Chen[2]

[1]Key Laboratory of Flight Techniques and Flight Safety
Civil Aviation Flight University of China, Guanghan,
Sichuan 618307, China
zeng.h.z@outlook.com, chenyaqingmail@sina.com, zhouchao@cafuc.edu.cn

[2]College of Electronics and Information Engineering
Sichuan University, Chengdu,
Sichuan 610065, China
tyznature@163.com, xingc@live.cn

***Abstract* –** This work analyzes the temperature effects on microwave circuits by employing a novel field-circuit hybrid multiphysics simulation. Firstly, the multiphysics simulation is implemented by solving the coupled governing equations including Poisson equations, semiconductor transport equations, and thermodynamic equations; then, the multiphysics simulation is incorporated into circuit analysis; finally, the circuit simulation results are integrated into the finite-difference time-domain (FDTD) simulation by equivalent sources. In this manner, a field-circuit hybrid multiphysics simulation method is presented. Taking two different microwave rectifiers operating at S- and C-band as examples, temperature effects are analyzed by the proposed approach. Simulation results are in good agreement with measured values, demonstrating the accuracy and applicability of the proposed approach. The presented method more suitably reveals the temperature effects on the rectifier.

***Index Terms* –** field-circuit hybrid simulation, multiphysics, Schottky diode rectifier, temperature effects.

I. INTRODUCTION

It is well known that temperature has a major impact on the performance of semiconductor devices and circuits. This is attributable to the fact that temperature changes the effective carrier density, electron and hole mobility, and material properties of semiconductor devices, thereby affecting the performance of the entire circuit [1].

With the development of wireless power transmission, research on microwave rectifiers has attracted considerable attention as a key component of converting space electromagnetic energy into DC. Thereby, the temperature effects caused by the injection of high-power microwave energy into the rectifier cannot be ignored. The accurate and efficient simulation of the temperature effects requires solving more challenging multiphysics problems [1–3]. Currently, multiphysics simulation of semiconductor devices has become a reality. Since multiphysics simulation can better describe the operation of semiconductor devices under various conditions and more accurately predict their physical effects, the multiphysics analysis of semiconductor devices and circuits has received increasing attention in recent years [2]. Abundant research on the electrothermal behaviors of semiconductor devices and circuits, characterized by combining multiple physical equations including electromagnetic fields, semiconductor transport, and thermodynamics, is already available [3–6]. However, the multiphysics simulation of semiconductor devices is very complicated and time-consuming. Considering the significant time and memory requirement, even for the next-generation computer systems, it is almost impossible to accomplish the temperature analysis of entire microwave circuits [7].

So far, research works on temperature effect simulation of the whole microwave circuit are very rare. In general, microwave circuits could be analyzed using either frequency- or time-domain full-wave simulation method [8]. However, in dealing with nonlinear semiconductor devices, time-domain methods enjoy the advantage of allowing for the direct analysis of field-circuit interactions without resorting to harmonic balance or port extraction methods [9]. Since FDTD method remains a popular choice for solving many electromagnetic problems, because of its versatility and ability for dealing with complex geometries, materials, and environments [10–12]. Thus, in the authors' previous work, a physical

Submitted On: February 27, 2022
Accepted On: September 23, 2022

https://doi.org/10.13052/2022.ACES.J.370709

model-based field-circuit hybrid simulation method was proposed, and a good agreement between rectifier simulation and measurements was obtained. However, the temperature effects on the microwave rectifier were not taken into account in order to simplify the simulation process [13]. Since microwave rectifiers usually work under high frequency and/or large signals, the temperature effects cannot be ignored. Therefore, the presented research extends previous work by coupling the multiphysics simulation of semiconductor devices to field-circuit hybrid simulation based on FDTD. To this end, the multiphysics simulation is implemented by solving the coupled governing equations including Poisson equations, semiconductor transport equations, and thermodynamic equations; then the multiphysics simulation is incorporated into circuit analysis; finally, the circuit simulation taking into account multiphysics is coupled to FDTD simulation by equivalent sources. In this manner, this paper presents a hybrid field-circuit multiphysics simulation approach. The presented simulation approach is applied to analyze the temperature effects of microwave rectifiers operating at S- and C-band frequencies and a series of experiments are conducted to validate the approach.

This approach not only characters the behaviors of microwave rectifiers under large signal conditions but also predicts its temperature effects. A further obvious advantage is that the hybrid solution scheme reduces the computational burden significantly, enabling system-level circuit simulation and analysis of temperature effects.

II. THE HYBRID FIELD-CIRCUIT SIMULATION APPROACH BASED ON MULTIPHYSICS

The size of semiconductor chips is on the micro- or nano-scale, while the size of device packages and microwave circuits may be on the millimeter scale or larger. Assuming the FDTD field-circuit simulation adopts the unified grid discretization, then the required calculations resources are prohibitively large to accomplish the simulation. While the field-circuit simulation based on an equivalent source can easily integrate the equivalent circuits simulation into full-wave FDTD simulation, greatly reducing the computational burden. Therefore, in order to address the temperature effect analysis problem of microwave rectifiers, this paper couple multiphysics simulation of the semiconductor device to the circuit simulation, and integrate them into the FDTD simulation by equivalent sources, presenting a more accurate and effective hybrid simulation approach. This section provides an introduction to the multiphysics simulation of semiconductor devices and their coupling with circuits, as well as the field-circuit hybrid multiphysics simulation based on equivalent sources.

A. Multiphysics analysis and simulation for semiconductor devices

The physical model of semiconductor devices is established based on the geometrical structure and manufacturing process and represented by parameters such as the device's junction width, gate length, channel thickness, etc. Semiconductor devices are often thermally sensitive, and multiphysics simulations that include temperature effects more accurately model carrier transport and characterize device behaviors.

For numerical analysis of semiconductor devices, a series of low-order approximate equations can be derived from electromagnetic field theory and semiconductor physics. Among them, the drift-diffusion model (DDM) is the most widely used semi-classical model. Up until now, DDM successfully simulate the semiconductor carrier transport phenomenon under non-isothermal conditions, thereby basic equations are Poisson Equation, current continuity equation, and drift-diffusion equation [14, 15]:

$$\varepsilon\nabla^2\varphi = q(p-n+N_t), \tag{1}$$

$$\partial n/\partial t = q^{-1}\nabla J_n + G - R, \tag{2}$$

$$\partial p/\partial t = -q^{-1}\nabla J_p + G - R, \tag{3}$$

$$J_n = \mu_n k_B(T\nabla n + n\nabla T) + q\mu_n n\nabla\varphi, \tag{4}$$

$$J_p = -\mu_p k_B(T\nabla p + p\nabla T) + q\mu_p p\nabla\varphi, \tag{5}$$

where ε, q and φ denote the material permittivity, electronic chargeand electrostaticpotential, respectively; N_t, n and p denote the doping, electron and holes density, respectively. G and R denote carriers generation rate and recombination rate, respectively. J_n and J_p denote the electron and the hole current density, respectively; T, k_B, μ_n and μ_p denote the temperature, Boltzmann constant, electron and hole mobility, respectively [1].

To analyze the temperature effects on semiconductor performance in microwave power circuits, in addition to DDM, the multiphysics simulation of semiconductor devices should contain the heat conduction equation and equations containing temperature-dependent characteristic parameters [16]:

$$\rho c\cdot\partial T/\partial t = \nabla[k(T)\nabla T] + g, \tag{6}$$

$$g = (J_n + J_p + \varepsilon\partial E/\partial t)\cdot E + RE_g, \tag{7}$$

$$n_i^2 = \mathrm{n_0 p_0} = N_c N_v \exp(E_g/k_B T), \tag{8}$$

$$\mu_{n,p}(T) = \mu_{n,p}^0 (T/T_0)^{-\alpha} \Big/ \left[1 + (E/E_c)^{\beta}\right]^{1/\beta}, \tag{9}$$

$$\tau_{n,p}(T) = \tau_{n,p}^0 (1 + N_t/N_{n,p})(\mathrm{T/T_0})^{\gamma}, \tag{10}$$

where ρ and c are the material density and the thermal conductivity, respectively; g is the heat generated per unit time and volume, E and E_g is the electric field and band-gap width of diode, respectively; N_c and N_v are

effective state densities of the conduction band bottom and valence band top, respectively; $\mu_{n,p}^0$ and $\tau_{n,p}^0$ are the effective mobility and the lifetime of electrons and holes at ambient temperature, respectively; E_c is the critical field;; α, β and γ are empirical constant [14].

The multiphysics equation system consists of Eqs. (1)–(10) and is a coupled nonlinear partial differential equation system. In fact, it is impossible to give a closed-form solution, thereby an iterative numerical method is employed to solve this system equations.

It can be seen that the main unknowns in the multiphysics equation system are: n, p, φ and T. Without loss of generality, taking one-dimensional space $x = 0 - L$ as an example, the device grid division is shown in Fig. 1.

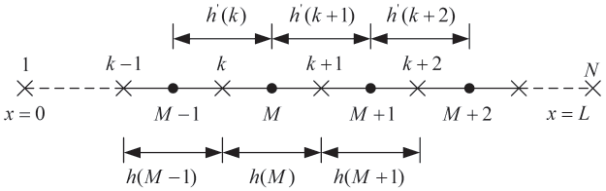

Fig. 1. The one-dimensional difference grids of semiconductor devices.

When T is a known value, The electrical characteristics Eqs. (1)–(5) are discretized by central difference and linearize [17], the whole procedure can be simplified to the solution of an increment equation [18]:

$$A\Delta y_{k-1} + B\Delta y_k + C\Delta y_{k+1} = H_k, \tag{11}$$

where 3×3 coefficient matrices; H is a 3×1 coefficient matrices. coefficient matrices value are described in [16].

When n, p and φ are known values, the heat conduction Eq. (6) may be discretized into first-order ordinary time-dependent differential equations [18]:

$$\frac{T_{k+1} - T_k}{h_{k,k+1}} - \frac{T_k - T_{k-1}}{h_{k-1,k}} + g = \frac{dC_k \cdot T_k}{dt}, \tag{12}$$

where $C_k, h_{k,k+1}$ and $h_{k-1,k}$ are the discretization coefficients. By using the Newton-Raphson iteration method,(12) can be can be rewritten as an increment equation:

$$aT_{k-1} + bT_k + cT_{k+1} = h, \tag{13}$$

where a, b, c, and h are the coefficients. Eqs. (11) and (13) can also be solved by using the chasing method, and the true values of n, p, φ, and T can be obtained after many iterations [19].

The iterative procedure for the multiphysics simulation of the semiconductor model is shown in Fig. 2. Firstly, the physical parameters of the semiconductor device are calculated by the initial electrical and temperature parameter (the carrier mobility generation and recombination rate etc.) and the semiconductor devices are solved by introduced electrical Eqs. (1)-(5). Then the heat conduction Eq. (6) and (7) are solved by the electric field, current, and other parameters to obtain the temperature, the electrical parameters are updated based on the current temperature and obtain the electrical field and temperature until it converges. Finally, the device voltage and current is calculated.

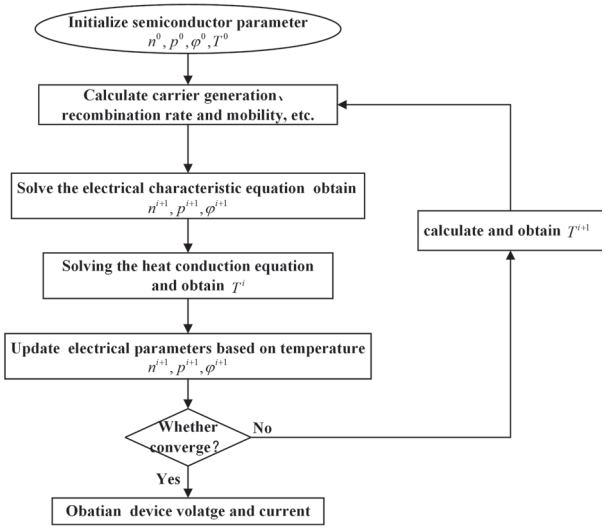

Fig. 2. Brief flow chart for multiphysics simulation of semiconductor device.

B. Integrating multiphysics simulation of semiconductor devices into circuit analysis

The circuit analysis is an indispensable part for conventional field-circuit hybrid simulation, which needs to integrate the equivalent circuit simulation into FDTD by equivalent sources. According to circuit analysis theory, circuit simulation can be rewritten as a system of equations by an improved nodal analysis method [20]:

$$\begin{cases} f_1(U_1, U_2, \ldots, U_k) = 0 \\ f_2(U_1, U_2, \ldots, U_k) = 0 \\ \cdots \\ f_k(U_1, U_2, \ldots, U_k) = 0 \end{cases}. \tag{14}$$

Here k is the index of the unknown node voltage, U is the unknown value, $f_k(U_1, U_2, \ldots, U_k)$ is the node voltage equation. The solution procedure of the nonlinear(14) is converted to the Newton-Raphson iterative equations:

$$U^{n+1} = U^n - J^{-1}(\mathrm{U}^n) f(\mathrm{U}^n), \tag{15}$$

where $U = [U_1, U_2, \ldots, U_k]^T$, $f(U) = [f(U_1), f(U_2), \ldots, f(U_k)]^T$.

J_{is} the node voltage equation:

$$J = \begin{bmatrix} \frac{\partial f_1}{\partial U_1} & \frac{\partial f_1}{\partial U_2} & \cdots & \frac{\partial f_1}{\partial U_k} \\ \frac{\partial f_2}{\partial U_1} & \frac{\partial f_2}{\partial U_2} & \cdots & \frac{\partial f_2}{\partial U_k} \\ \vdots & \vdots & \ddots & \vdots \\ \frac{\partial f_k}{\partial U_1} & \frac{\partial f_k}{\partial U_2} & \cdots & \frac{\partial f_k}{\partial U_k} \end{bmatrix} \tag{16}$$

For any semiconductor device in the circuit, assuming the device is located in the j-th branch, and two adjacent nodes are (k-1) and k, the nonlinear relationship between the branch current I_j and the terminal voltage can be expressed as [20]:

$$I_j = \psi(U_j) = \psi(U_k, U_{k-1}). \tag{17}$$

To obtain transient response of the circuit, the diode branch current Eq. (17) is obtained by the multiphysics simulation, introduced previously. while the branch currents of other linear devices are derived from the circuit simulation based on its constitutive equations. In this way, the multiphysics and the circuit simulation are integrated into a unified scheme.

C. Field-circuit hybrid multiphysics simulation based on equivalent sources

In numerical simulation of antennas and microwave circuits based on FDTD, the current through the lumped element can be regarded as an additional current term in the Maxwell's integral equations [21]:

$$\oint_C \vec{E} \cdot d\vec{l} = -u \int_S \frac{\partial \vec{H}}{\partial t} \cdot d\vec{s}. \tag{18}$$

$$\oint_C \vec{H} \cdot d\vec{l} = \varepsilon \int_S \frac{\partial \vec{E}}{\partial t} \cdot d\vec{s} + I_s, \tag{19}$$

where I_s represents the current flowing through the semiconductor device. The Eqs. (18) and (19) can be easily convert to differential forms, and discrete by FDTD Yee grid. Since physical sizes of semiconductor devices are generally much smaller than the minimum wavelength of the operating frequency, it could be modeled by one dimension, and only occupied one or several serial Yee grid under the uniform FDTD framework, as shown in Fig. 3.

Without loss of generality, in Fig. 3, assume a semiconductor device is located between nodes a and b,

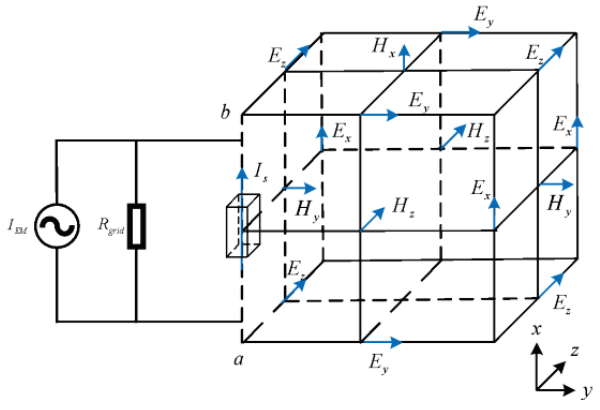

Fig. 3. Discrete form of Yee grid containing semiconductor devices.

The terminal voltage of the semiconductor device V_{ab} can easily be derived from the electric field through path integral [21]:

$$V_{ab}^n = \int_a^b \vec{E}_{ab}^n \cdot d\vec{l}. \tag{20}$$

A control equation can be derived by combining with Eqs. (18)-(20):

$$(I_x^{n+1})_{EM} = \frac{V_{ab}^{n+1}}{(R_x^{n+1})_{grid}} + I_{sx}^{n+1}. \tag{21}$$

In which [21]:

$$(I_x^{n+1})_{EM} = \frac{\sum_{\beta=(i_s,j_a,k_s)}^{\beta=(i_h,j_s,k_b)} dx \cdot \mathrm{K}_{xijk}^{n+1}}{(R_x^{n+1})_{grid}}. \tag{22}$$

$$(R_x^{n+1})_{grid} = \sum_{\beta=(i_i,ja,k_a)}^{\beta=(i_0,k_k,k_j)} \frac{\Delta t}{\varepsilon_{x(i,j,k)}} \cdot \frac{\Delta x}{\Delta y \cdot \Delta z}. \tag{23}$$

$$K_{xijk}^{n+1} = E_{x(i,j,k)}^n + \frac{dt}{\varepsilon}\left(\frac{H_{z(i,j,k)}^{n+\frac{1}{2}} - H_{z(i,j-1,k)}^{n+\frac{1}{2}}}{dy} - \frac{H_{y(i,j,k)}^{n+\frac{1}{2}} - H_{z(i,j,k-1)}^{n+\frac{1}{2}}}{dy} - J^{n+\frac{1}{2}cx(i,j,k)}\right). \tag{24}$$

According to circuit analysis, the form of Eq. (21) can be interpreted as a controlled current source in parallel with an equivalent resistance. Where I_{EM} is deduced from the electromagnetic field value of the previous time step, R_{grid} is an equivalent resistance that calculated from FDTD grid size [21]. The FDTD field-circuit scheme along the y, z direction is similar, its implicit form ensures simultaneous calculation of the electric field (deduced from voltage) and current, resulting in the simulation method having a higher stability.

Microwave circuits containing semiconductor devices are generally considered to be a hybrid system and can be simulated using a field-circuit hybrid method based on equivalent sources [22]. Generally, the equivalent sources first equate the electromagnetic field effect on the semiconductor devices as lumped circuits, and then solves the circuits formed by the connection between the equivalent source and the lumped circuit, finally converting the obtained voltage or current to the electric or magnetic field value.

In our proposed field-circuit hybrid multiphysics simulation method, the equivalent circuits of semiconductor devices are substituted by multiphysics modeling and simulation; then, the multiphysics simulation of semiconductor devices is coupled with circuit analysis, and integrate into FDTD full-wave simulation. The transient simulation of the entire circuit system is implemented by advancing synchronously and exchanging data within each FDTD time step, as shown in Fig. 4.

It is important to emphasize that the initial state of the circuit transient analysis needs to be set to the end

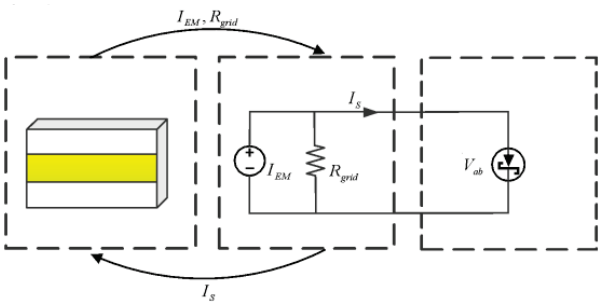

Fig. 4. The coupling relationship of multi-physics field.

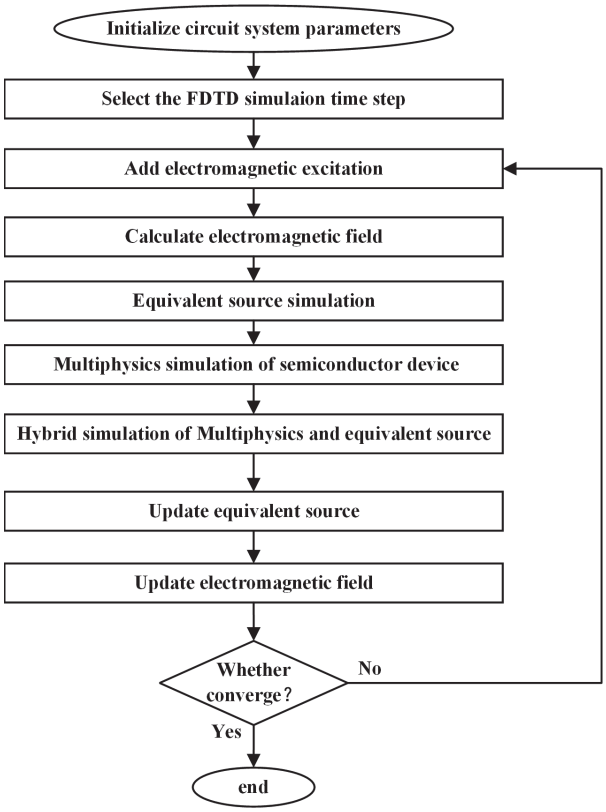

Fig. 5. The flow chart of field-circuit hybrid multiphysics Simulation.

state, especially the state of the semiconductor device (including electric field, carrier density distribution, and mobilities, temperature, etc.) at the previous time step. This is especially essential for accurate and effective analysis of the whole system. A brief flow chart is shown in Fig. 5.

III. SIMULATION AND EXPERIMENT

Silicon-based diodes of the HSMS-282x series are widely used in microwave rectifiers, featuring low costs and good RF characteristics. It is composed of thin epitaxial layers deposited on heavily doped substrates, with

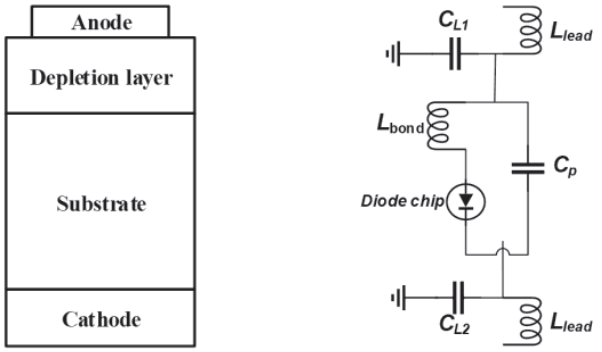

(a) (b)

Fig. 6. Physical model parameters of Schottky diodes: (a) the structure of Schottky diode, (b) the package equivalent circuit.

Schottky contacts at the anode and ohmic contacts at the cathode [13].

To reduce the simulation burden, we make a one-dimensional simplification with maintaining the diode characteristics, and its inner structure is shown in Fig. 6 (a) [23]. In this figure, Schottky barrier height and metal work function are denoted by ϕ_B and ϕ_M, respectively; the doping concentration of epitaxial layer and substrate are indicated by $N_d N_D$ and N_{sub}, respectively; the length of epitaxial layer and substrate are indicated by L_E L_{epi} and L_{sub}, respectivelyL_{sub}; the effective contact area of the diode is denoted by A_d. For microwave frequency applications, the diode package effect cannot be ignored. Schottky diodes of HSMS-282x series adopt SOT-323 package size, the package effect could be characterized by the equivalent circuit shown in Fig. 6 (b), which is suitable up to 6 GHz. In Fig. 6 (b), C_{L1} and C_{L2} are lead capacitors, respectively; C_p is the package capacitor; L_{bond} and L_{lead} are the welding inductance and lead inductance, respectively.

The physical model and package parameters of Schottky diode HSMS-282 and HSMS-286 have been extracted in the authors' previous work, they are listed in Table 1 and Table 2 respectively for easy reference [13].

The MW-to-DC power conversion efficiency (PCE) is a key indicator to measure the performance of microwave rectifiers [24]. Generally, PCE of the rectifier could be calculated by the following formula:

$$\eta = \frac{P_{DC}}{P_{MV}} \cdot 100\% = \frac{{V_{\text{out}}}^2}{P_{MV} \cdot R_{\text{load}}} \cdot 100\%, \qquad (25)$$

where P_{MV} and P_{DC} are the microwave input Power and DC output power, respectively; V_{out} and R_{load} are the output DC voltage and load, respectively [24].

To verify the accuracy and applicability of the proposed method in simulating the temperature effects of

Table 1: Physical parameters of two Schottky diodes

Parameters	HSMS-282	HSMS-286
Φ_B [V]	0.629	0.568
Φ_M [V]	4.679	4.631
N_d [m^{-3}]	5.44×10^{14}	2.91×10^{16}
N_{sub} [m^{-3}]	2×10^{18}	2×10^{18}
L_{epi} [μm]	0.97	1.327
L_{sub} [μm]	1.02	1.33
A_d [cm^2]	6×10^{-6}	5.61×10^{-6}

Table 2: Package parameters of two Schottky diodes

Parameters	HSMS-282	HSMS-286
C_p [pF]	0.16	0.2
L_{bond}[nH]	0.79	0.525
L_{lead}[nH]	0.86	0.98
C_{L1}[pF]	0.007	0.02
C_{L2}[pF]	0.002	0.08

microwave circuit, taking two different microwave rectifiers operating at S- and C-band as examples, the simulations are performed by presenting a field-circuit hybrid multiphysics approach under different ambient temperatures (25 ℃, 75 ℃). The simulation program is executed on a computer workstation with a 3.4GHz frequency Intel Core CPU, 32GB memory and 64-bit Windows operating system. Furthermore, two rectifiers are placed into a well-sealed thermostat, and the conversion efficiency is measured to validate the simulation results.

A. The temperature effects analysis on S-band microwave rectifiers

A compact S-band microwave rectifier working at a frequency of 2.45 GHz has been manufactured by utilizing the HSMS-282B diode. The type of printed circuit board (PCB) used in the rectifier is F4B-2 with a relative dielectric constant of 2.65, a loss tangent of 0.0012 and a thickness of 1 mm. The manufactured rectifier dimension is 20 mm × 16 mm; its structure and photograph are shown in Fig. 7 (a) and (b), respectively.

It is known that the rectifier performance is determined by the entire circuit structures, including input matching and output filtering. However, as a nonlinear device, the Schottky rectifier diodes always generate high-order harmonics. Although the output filters only allow DC to pass through and reflects the fundamental frequency and harmonics, there are still a few harmonics superimposed on the DC output to cause a ripple.

For the S-band rectifier, the computational domain is uniformly divided into 240×190×32 (including 5-layer air and 10-layer CPML) grids in the x, y, and z directions, the number of iterations is 55000, each iteration

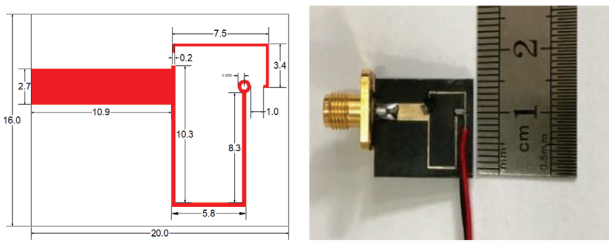

Fig. 7. (a) Schematic diagram of the 2. 45 GHz rectifier; (b) Photograph of manufactured 2. 45 GHz rectifier.

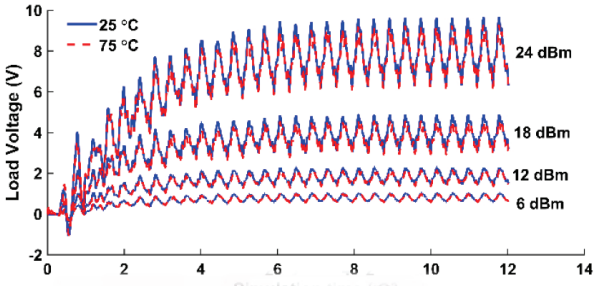

Fig. 8. Several typical output voltages of S-band rectifier at different ambient temperatures.

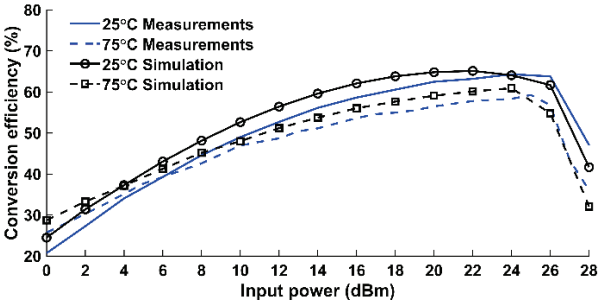

Fig. 9. PCE of S-band rectifier simulation and measurements at different ambient temperatures.

time is approximately 8.4 s, the total simulation time is about 128.3 hours. Here, several typical simulated output voltages of the rectifier at different ambient temperatures are given in Fig. 8. The simulated and measured PCE under different temperature (25 ℃, 75 ℃) are shown in Fig. 9.

B. The temperature effects analysis on C-band microwave rectifiers

A C-band rectifier was manufactured working at frequency 5.8 GHz by utilizing the HSMS-286B diode, which still adopts the same PCB as the above-mentioned S-band microwave rectifier. The manufactured rectifier dimension is 20 mm × 30 mm, its structure and photograph are shown in Fig. 10 (a) and (b), respectively.

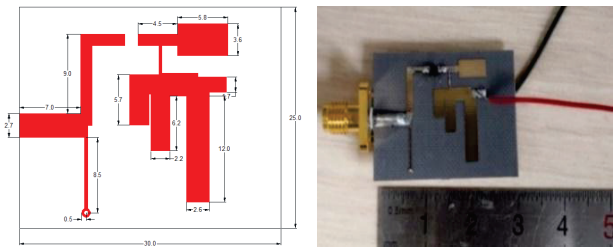

(a) (b)

Fig. 10. (a) Schematic diagram of the 5. 8 GHz rectifier; (b) Photograph of manufactured 5. 8 GHz rectifier.

For the C-band rectifier, the computational domain is uniformly divided into 280×280×22 (including 5-layer air and 10-layer CPML) grids in the x, y, and z directions, the number of iterations is 35000, each iteration step is approximately 9.6 s, the total simulation time is about 93.3 hours. The typical output voltages of C-band rectifier at different ambient temperatures (25 ℃, 75 ℃) are simulated, and shown in Fig. 11. The simulated and measured PCE under different temperature are shown in Fig. 12.

From Figs. 9 and 12, it can be clearly seen that both S-band and C-band Schottky rectifiers, the PCE have a consistent variation trend with temperature. The slight errors may attribute to the discontinuities of SMA

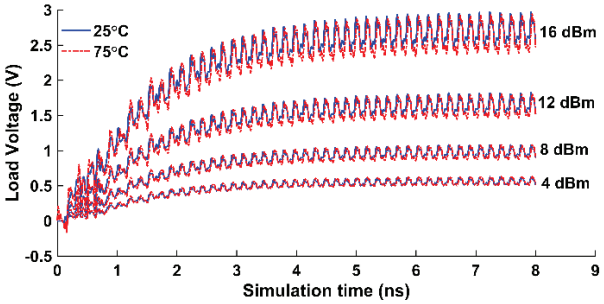

Fig. 11. Several typical output voltages of C-band rectifier at different ambient temperatures.

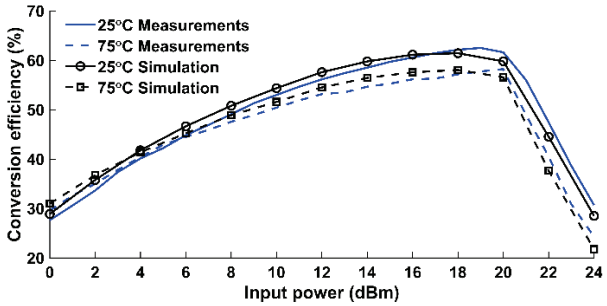

Fig. 12. PCE of C-band rectifier simulation and measurements at different ambient temperatures.

connectors and temperature effects on PCB material properties. The PCE increases slightly with temperature increase under low input power, yet decreases significantly with temperature increase under high input power. From a physical point of view, that is due to the fact that the Schottky diode is a cut-off state under low input power, carrier density of the Schottky diode increase with temperature rise, which causes diode current aggrandize and makes the PCE gradually increase. However, as the input power continually increases, the Schottky diode becomes a turn-on state, the diode impedance diminution with the temperature rise, which will lead to the input and output impedance mismatch and make the PCE decrease significantly.

The measured results are validated by the simulation results at different temperatures, which confirm the effectiveness and applicability of our proposed approach.

Furthermore, excessive input power may cause Schottky diode self-heating, resulting in power conversion efficiency decrease. Thus, power conversion efficiency of rectifiers can be optimized by carefully selecting suitable temperature conditions, especially for energy harvesting application at a low input power level.

IV. CONCULSION

The temperature effects of electronic devices and circuits are essential for microwave power application. This paper adopts a novel field-circuit hybrid multiphysics simulation to analyse the temperature effects of microwave rectifier. Firstly, multiphysics model involving semiconductor and thermal conducting is solved; then, multiphysics simulation is embedded into circuit analysis; finally, this circuit analysis was coupled into field-circuit hybrid simulation based on FDTD. Taking two different Schottky diode rectifiers operating at S- and C-band as examples, simulation results match well with the measured ones, which validate the accuracy and applicability. This method that combines the multiphysics simulation and FDTD solution can greatly improve the simulation accuracy of microwave power circuits. This approach not only has the advantage of accuracy and versatility stemming from the multiphysics simulation, but also retains simplicity and efficiency of the FDTD field-circuit hybrid simulation.

Moreover, the propose method effectively reveal the physical mechanism of rectifier temperature effects. Furthermore, the presented approach could be extended to more complex circuits without significant modifications. This method may become an attractive candidate for simulating and predicting temperature effects of microwave power circuits.

ACKNOWLEDGEMENT

This work is supported by Flight Efficiency Improvement Research Center (No. JG2022-09) of Civil

Aviation Flight University of China, Funding Program of CAFUC (No. ZX2021-03), and National Key R&D Program of China (No. 2018YFC0809500).

REFERENCES

[1] S. M. Sze, Y. Li, and K. K. Ng, *Physics of Semiconductor Devices*, John Wiley & Sons, 2021.

[2] J.-M. Jin and S. Yan, "Multiphysics modeling in electromagnetics: Technical challenges and potential solutions," *IEEE Antennas Propag. Mag.,* vol. 61, no. 2, pp. 14-26, 2019.

[3] M. Riccio, G. De Falco, P. Mirone, L. Maresca, M. Tedesco, G. Breglio, and A. Irace, "Accurate spice modeling of reverse-conducting IGBTs including self-heating effects," *IEEE Trans. Power Electron.,* vol. 32, no. 4, pp. 3088-3098, Apr. 2017.

[4] N. Lin and V. Dinavahi, "Dynamic electromagnetic-thermal modeling of MMC-based DC-DC converter for real-time simulation of MTDC grid," *IEEE Trans. Power Del.,* vol. 33, no. 3, pp. 1337-1347, Jun. 2018.

[5] T. Pan, D. Ding, H. Li, and X. Cheng, "Transient electro-thermal analysis of a common source amplifier circuit with a physics-based MOSFET model," *Appl. Comput. Electrom.,* vol. 34, no. 7, 2019.

[6] A. Tsibizov, I. Kovacevic-Badstubner, B. Kakarla, and U. Grossner, "Accurate temperature estimation of SiC power MOSFETs under extreme operating conditions," *IEEE Trans. Power Electron.,* vol. 35, no. 2, pp. 1855-1865, Feb. 2020.

[7] H. H. Zhang, P. P. Wang, S. Zhang, L. Li, P. Li, W. E. Sha, and L. J. Jiang, "Electromagnetic-circuital-thermal multiphysics simulation method: a review," *Prog. Electromagn. Res.,* vol. 169, pp. 87-101, 2020.

[8] Q. Zhan, Y. Wang, Y. Fang, Q. Ren, S. Yang, W.-Y. Yin, and Q. H. Liu, "An adaptive high-order transient algorithm to solve large-scale anisotropic Maxwell's equations," *IEEE Trans. Antennas Propag.,* vol. 70, no. 3, pp. 2082-2092, 2021.

[9] E. K. Miller, "Time-domain modeling in electromagnetics," *J. Electromagnet. Wave,* vol. 8, no. 9-10, pp. 1125-1172, 1994.

[10] G. Xu, X. Chen, Z. Zheng, and K. Huang, "A hybrid FDTD-SPICE method for the analysis of microwave circuits," *Int. J. Appl. Electrom.,* vol. 49, no. 1, pp. 79-90, 2015.

[11] X. Wang, L. Wang, J. Zhuo, X. Lu, M. Yuan, J. Zhou, and Q. H. Liu, "A hybrid CN-FDTD-SPICE solver for field-circuit analyses in low-frequency wideband problems," *IEEE Trans. Compon. Packag. Technol,* vol. 10, no. 10, pp. 1721-1728, 2020.

[12] Y. Wang, J. Wang, L. Yao, and W.-Y. Yin, "EMI analysis of multiscale transmission line network using a hybrid FDTD method," *IEEE Trans. Electromagn. Compat.,* vol. 63, no. 4, pp. 1202-1211, 2021.

[13] H. Zeng, Y. Tang, X. Duan, and X. Chen, "A physical model-based FDTD field-circuit co-simulation method for Schottky diode rectifiers," *IEEE Access,* vol. 7, pp. 87265-87272, 2019.

[14] K. Xu, X. Chen, and Q. Chen, "Non-quasi-static effects simulation of microwave circuits based on physical model of semiconductor devices," *Appl. Comput. Electrom.*, pp. 992-998, 2020.

[15] K. Xu, X. Chen, and Z. Chen, "A physics-based transient simulation and modeling method for wide-frequency electrical overstress including ESD," *Appl. Comput. Electrom.*, pp. 505-512, 2021.

[16] S. Selberherr, *Analysis and Simulation of Semi-Conductor Devices*, Springer Science & Business Media, 2012.

[17] G. Sun and C. W. Trueman, "Efficient implementations of the Crank-Nicolson scheme for the finite-difference time-domain method," *IEEE Trans. Microw. Theory Tech.,* vol. 54, no. 5, pp. 2275-2284, 2006.

[18] J. Q. Chen, X. Chen, C. J. Liu, K. Huang, and X. B. Xu, "Analysis of temperature effect on pin diode circuits by a multiphysics and circuit cosimulation algorithm," *IEEE Trans. Electron Devices*, vol. 59, no. 11, pp. 3069-3077, 2012.

[19] D. Poole, *Linear Algebra: A Modern Introduction,* Cengage Learning, 2014.

[20] X. Chen, J. Q. Chen, K. Huang, and X.-B. Xu, "A circuit simulation method based on physical approach for the analysis of Mot_bal99lt1 pin diode circuits," *IEEE Trans. Electron Devices*, vol. 58, no. 9, pp. 2862-2870, 2011.

[21] W. Sui, *Time-domain Computer Analysis of Nonlinear Hybrid Systems*, CRC Press, 2018.

[22] H. Zeng, and X. Chen, "Nonlinear analysis for microwave limiter using a field-circuit simulator based on physical models," *IEEE Microw. Wireless Compon. Lett.,* vol. 30, no. 2, pp. 129-132, 2020.

[23] H. Wang, X. Chen, G. H. Xu, and K. M. Huang, "A novel physical parameter extraction approach for Schottky diodes," *Chin. Phys. B,* vol. 24, no. 7, Jul. 2015.

[24] C. Liu, F. Tan, H. Zhang, and Q. He, "A novel single-diode microwave rectifier with a series band-stop structure," *IEEE Trans. Microw. Theory Tech.,* vol. 65, no. 2, pp. 600-606, 2016.

Hongzheng Zeng received an M.S. degree from Chongqing University of Posts and Telecommunications, China, in 2014, and a Ph.D. degree in Radio Physics at Sichuan University, China, in 2020. Presently, he is the Research Associate with Key Laboratory of Flight Techniques and Flight Safety, Civil Aviation Flight University of China. His research interests include numerical methods applied in electromagnetics, microwave circuits simulation, and electromagnetic environmental effect.

Yaqing Chen received an M.S. from Southwest Jiaotong University, China, in 2005. Presently, he is a professor and executive deputy director of the Key Laboratory of Civil Aviation Flight Technology, at Civil Aviation Flight University of China. His research interests include general aviation operations and safety, and air traffic management. Professor Chen is the member of civil aviation science and technology committee, and the academic and technical leader candidate in Sichuan province, China.

Chao Zhou received an M.S. from Southwest Jiaotong University, China, in 2002, and a Ph.D. degree from University of Electronic Science and Technology University, China, in 2013. Presently, he is a professor at Civil Aviation Flight University of China. His research interests include civil aviation electromagnetic environmental effects and unmanned aircraft systems. Professor Zhou is the visiting researcher fellow of Chengdu Computing Institute of China Commercial Aircraft, and the academic and technical leader candidate in Sichuan province, China.

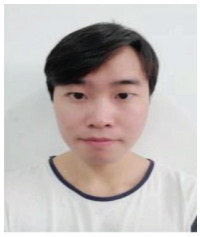

Yuzhu Tang received his B.S. in communication engineer in 2012 from University of Electronic Science and Technology and M.S. from Chengdu University of Information Engineering, China, in 2017. Currently, he is pursuing his Ph.D. in radio physics at Sichuan University. His research is mainly focused on microwave active circuits and antenna.

Xing Chen received an M.S. degree in radio physics and the Ph.D. degree in biomedical engineering from Sichuan University, Sichuan, China, in 1999 and 2004, respectively. Currently, he is a professor and radio department chair with the College of Electronics and Information Engineering, Sichuan University. His research interests include antenna, microwave imaging, global optimization, numerical methods applied in electromagnetics, and parallel computation. Professor Chen is an IEEE Senior Member, Senior Member of the Chinese Institute of Electronics, and antenna branch commissioner of the Chinese Institute of Electronics.

SDR-based Radar for Human Detection

Marcelo B. Perotoni[1], Kenedy M. G. dos Santos[2], Danilo B. Almeida[2], and Daniel Jonathas[2]

[1]UFABC, Santo Andre, SP, 09210-580, Brazil
Marcelo.perotoni@ufabc.edu.br

[2]IFBA, Vitoria da Conquista, BA, 45078-900, Brazil
kenedymarconi@gmail.com

***Abstract* –** Software-defined radios (SDRs) have been applied to several applications, taking advantage of their inherent versatility. It is reported a low-cost radar intended to detect human activity, at the frequency of 4.1 GHz, with an SDR on the receiving branch and a programmable RF synthesizer operating as a continuous-wave transmitter. Amplitude variations on the received signal indicate human activity, its operation is tested in indoor and outdoor scenarios. The interface to the SDR is performed using the open-source tool GNU Radio. It was possible to detect human movement at a maximum distance of 9 meters, in an open area. The system is versatile in terms of power and frequency, totally controlled by software in a transparent and straightforward way.

***Index Terms* –** microwave systems, radar, software-defined radio.

I. INTRODUCTION

Detection of human targets has been of interest lately for several applications, such as senior people living alone, surveillance of law-offenders, and even enforcing social isolation during pandemic restrictions. Radars for these kinds of human targets have been thoroughly reviewed in [1]. Frequency modulated continuous-wave (FMCW) radar is one of the most used techniques, with the Doppler effect applied to the received wave containing the target position and velocity; for that goal, it needs synchronous detection. The low-frequency mixing product generated encodes the speed measured, heart rate, or respiratory function. Following this principle, using the frequency of 5.7 GHz, a system detects and locates the human presence using both interferometric and FMCW modes with National Instruments PXI boards [2]. Detection of vital signals (cardiac and respiratory) are extracted after further processing of the echo signal. Modules operating at millimeter-waves have been employed to report vital signals of children inside vehicles after a Deep-Learning framework is applied to the gathered data [3]. For indoor environment mapping, a 62 GHz FMCW radar was assembled and mounted on top of a moving robot [4], using two different chirp pulses transmitted; one for long-range and another for short-range, the latter reaching higher frequencies. Using commercial millimeter-wave 77-GHz evaluation boards (TI AWR1642), vital signals are acquired and analyzed, respiratory signals within 0.1 to 0.5 Hz and heart rate in the 0.8 to 2 Hz range [5], later processed with a wavelet-based algorithm. A home-built system operating as a 24-GHz FMCW radar was used to monitor different sleep patterns encoded in the heart rate and respiration parameters [6]. vector network-analyzers (VNAs), given their synchronous detection, contain the phase information of the detected signals. Two broadband horn antennas were connected to the VNA ports, one excited by the VNA (0 dBm output power) and the other set as the receiver. The received signal around 2.5 GHz was analyzed using the cyclostationary technique [7] so that cardiac and breathing signals are extracted. The same vital signal detection is analyzed at the lower frequency of 1 GHz, using custom-made circuits for RF reception, and an Agilent RF generator operating as a transmitter (TX); the data analysis was later performed under Matlab [8]. Detection of people and respective vital signals in through-wall, non-invasive scenarios can be performed using UWB (Ultra-Wide Band) waveforms in the microwave range [9] and even Infrared (IR) [10], requiring more complex hardware and data processing to separate the signals from the clutter. In the context of vital signals, [11] presents a comparison between an Infrared UWB and a 60 GHz FMCW for this task, with observed higher SNR (Signal-to-Noise Ratio) and larger accuracy in favor of the former.

In contrast to ordinary radar, which is based on the return echo of a transmitted electromagnetic wave, radiometer applications rely on the detection of natural emissions from the human body, so they are eminently

Submitted On: May 5, 2021
Accepted On: May 18, 2022

https://doi.org/10.13052/2022.ACES.J.370710

passive, therefore eliminating the transmitter circuitry. A low-cost system based on commercial parts (LNB - Low-Noise Block Downconverter, parabolic antenna, and custom-designed low-frequency circuit) was reported [12]. It detects the temperature difference between the human body and surrounding walls, with the limitation of operation only in the near-field, due to the low-level amplitudes radiated by the body, on the 11 to 12 GHz frequency range. USRP (Universal Software Radio Peripheral) SDRs, in particular, given their available independent two-channel front-ends, offer an interesting alternative to passive radar detection, for instance, with the existing ambient WiFi signal used to detect hand movements [13]. One of the SDR RF inputs is considered as reference and the other as surveillance, each one connected to two antennas. Doppler frequency computed from both received signals mixed together enables hand-movement tracking.

This article describes a C-band (4.1 GHz) SDR-based radar which detects human presence, or life activity, based on a low-cost SDR for the receiving branch, with only one input channel. The transmitter is based on an independent I2C-controlled RF synthesizer. Its reception is non-synchronous, therefore the detection is based only on received amplitude fluctuations. Both SDR and software packages are open-source. The next sections delve into the hardware and software description, with results proving the real-world deployment in both indoor and outdoor environments.

II. HARDWARE

Figure 1 contains the block diagram of the proposed radar. Its core operates around a Hack RF One SDR. It has a single RF input, which can be set operating in half-duplex transmit or receive modes. It covers the range of 10 MHz to 6 GH with an instantaneous bandwidth of 8 MHz to 20 MHz. Its output delivers 8-bits IF (intermediate frequency) complex samples, divided into in-phase (I) and quadrature (Q) components. An internal 14-dB low-noise amplifier can be switched on and off by software. Radar range resolution, considering c as the speed of light, R the distance between the transmitter and

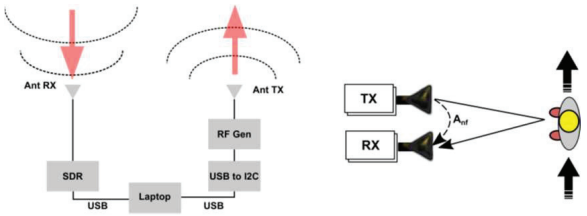

Fig. 1. Block diagram of the detector (left) and (right) main components of the received signal.

receiver, and Δt the two-way travel time, is defined as:

$$R = \frac{c\,\Delta t}{2}. \tag{1}$$

Indoor distances Rin the range of 2 m results in a round-trip time of approximately 13 ns, a period too short to be used in the SDR platform for a switching (pulsed) RF signal. For that reason, a continuous-wave mode (CW) was used. Also, given the fact that two different circuits are used for the transmit and receive branches, there is no need for a circulator, usually a narrow-band and costly device. The SDR delivers IF (Intermediate Frequency) time-domain samples to the host-PC through a USB channel. A broadband planar antenna is connected to the SMA coaxial SDR input. On the TX branch, a programmable RF synthesizer was used (ADF4351). It is programmed by writing its registers through an I2C protocol. Conversion between I2C and USB protocols is performed by an Arduino Uno with an auxiliary board, which scales down the 5V Arduino output to the 3.3V ADF4351 digital level. The RF synthesizer operates with two SMA output pins (differential mode), for this case the TX antenna was single-ended connected to one of the outputs, and the other terminal was left open. Human activity detection does not need to inform the speed, unlike Doppler radars to reduce the cost and size of the hardware. The signal s_R picked up by the receiving antenna can be written in terms of different components:

$$s_R(t) = A_{nf}cos(\omega_c t) + \sum_{n=1}^{p} A_n(t)\,cos(\omega_c t + \delta_n) + n(t). \tag{2}$$

Where ω_c is the transmitted angular frequency and $n(t)$ represents the noise. A_{nf} models the near-field coupling between the two antennas. Since both radiating elements are mechanically fixed the amplitude A_{nf} is theoretically stable in time, the time-varying component depending only on the synthesizer jitter and phase noise.

The second term contains the summation of p terms that arise due to the target movement and the multi-path, with each component modulated by a slow-varying amplitude $A_n(t)$ which contains information about the movement and the interaction with the environment. A generic phase δ represents the time delay of each reflected component arriving at the receiver. The overall system, considered as a sensor, should have maximized its sensitivity s in terms of the ratio between both amplitude parameters:

$$s = \frac{\sum_{n=1}^{p} A_n(t)}{A_{nf}}. \tag{3}$$

Lower transmitted output levels are positive from the power consumption point of view, as well as electromagnetic interference problems that may arise with nearby systems but incurs in lower signal-to-noise ratios, so the output power to be chosen is a trade-off to be

observed in the specific real-world application, depending on the environment and particular conditions. Legal constraints should be observed in accordance with local regulations (Brazil and the US reserve the chosen frequency range for satellite downlinks). Since the interest lies in human detection, proper care with non-ionizing safety levels should be taken [14].

The antennas were commercial planar units, a Log-Periodic (LPDA), nominal operation between 740 and 6000 MHz and Vivaldi (1.4 to 10.5 GHz), shown in Fig. 2 along with their measured return losses. At the used frequency of 4100 MHz, the return loss of both antennas was 14 dB. The LPDA was used as receiving, connected to the SDR whereas the Vivaldi as a transmitter.

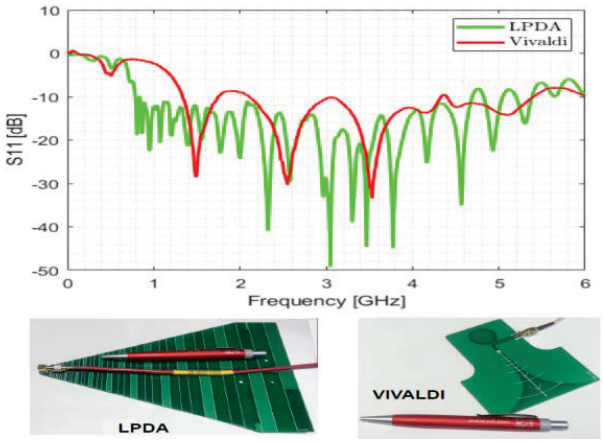

Fig. 2. Measured return loss of the two antennas (top), Vivaldi (right bottom), and LDPA (left bottom).

The antennas are separated by a distance of 40 cm, equivalent to 5.46 λ at the used frequency, this distance was chosen due to mechanical constraints. Smaller distances increase the nearfield coupling and larger separations incur in secondary maxima due to their Array Factor, which may generate stronger fluctuations in the received signal.

III. SOFTWARE

One of the most used software suites for digital processing and interface to SDRs is GNU Radio [15], an open-source platform that is similar to paid alternatives like Labview [16] and Matlab/Simulink [17]. GNU Radio uses C++ for time-critical routines and is wrapped in Python, used for the interface and communication with the user. GNU Radio Companion offers the possibility to generate a visual block-oriented flowgraph representing the data flow and processing from the SDR input all the way to its final visualization. It can generate a Python script that can be run independently of GNU Radio. It has some drawbacks, due to the constant independent development by voluntary contributors:

- Scarce documentation, help file without much details on some of the existing blocks.
- Unpredictable problems when used in Windows OS distributions, though its operation runs almost flawlessly with Linux flavors. The main reasons are due to driver conflicts and Python versions.
- Its constant cooperative evolution has turned some blocks defunct (obsolete), such as the Valve and also the WX GUI, which was replaced by the current default QT GUI.

In spite of these issues, it provides a stable and free solution to work with SDR data. Tests are quickly deployed, and a large number of signal processing blocks are available, such as FFT, FIR, and IIR filters, data visualization, file export, etc. The user can take advantage of the reconfigurability feature of SDRs by connecting blocks following an intuitive data flow concept, sometimes performing complex functions in a transparent way to the user. Fig. 3 shows the used flowgraph, in the block diagram and in the GNU Radio. It contains an osmocom source block that interfaces the HackRF SDR, setting its main parameters such as LNA/IF/Baseband gains, central frequency and bandwidth.

A DC block can be used to eliminate the zero-IF leak (which corresponds to the chosen central frequency), left

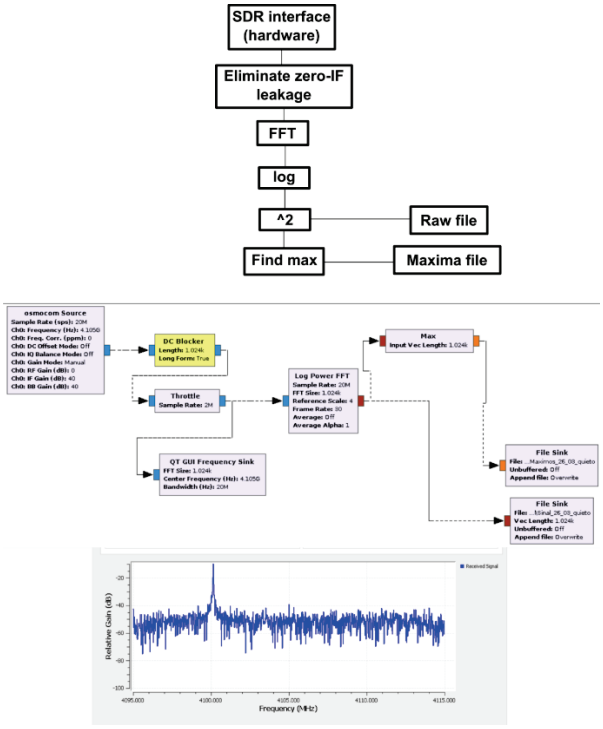

Fig. 3. GNU Radio flowgraph (top), GNU Radio main blocks shown (center), and example of the receiving CW signal(bottom).

bypassed in the final program for the sake of speed. The throttle block helps alleviate the processor overload, synchronizing the delivered samples, which otherwise flow among the blocks with its maximum allowed throughput, constrained only by the PC hardware. The stream undergoes an FFT operation and the maximum is found at every 1024 samples. The data is sent to two binary files, one containing the raw frequency domain values (real due to the log power FFT operation) and also their respective maxima, for comparison purposes. A Frequency sink block displays the instantaneous captured bandwidth in real-time, for visualization purposes and checking on the transmitted carrier. Bandpass filtering was also added to narrow down the frequency range across the transmitted CW carrier, but it resulted in a slower operation, with lost synchronization among the samples. For these matters, it was decided to keep the flowgraph as lean as possible and operate with binary files as output, to be later analyzed outside GNU Radio.

The created binary files are read out by means of Octave [18]/Matlab or Python commands, available for either complex or float values. In the present case, only float numbers are stored since the interest is in relative power.

IV. RESULTS

The first set of measurements was performed indoors in an area of approximately 4x5 m^2. Distances between the adult and radar varied from 0.5 to 4 m. Tests were performed with random movements and walking across the space using a normal gait. Figure 4 contains the plot for approximately 2 minutes. Units shown the power in dBr, relative dB used by GNU Radio, so conversion to dBm should require a calibration step against a known source. Since the interest lies in variation only, GNU Radio native dBr was kept throughout this evaluation. The maximum operation on the samples is shown against the raw signal, which contains 1024 more samples. The maxima vector is 2 kB whereas the raw signal is 1,300 kB. Output power was set to the minimum value, −4 dBm, and the SDR low-noise amplifier was switched off to avoid overloads. Oscillations seen in the still scenario vector are much less pronounced than in the samples during movement.

To evaluate the overall sensitivity, as well as outdoor operation, another set of tests was performed on a basketball court (Fig. 5), maintaining the same former power and gain settings. Ambient power spectra were recorded (20 MHz around the central frequency of 4,105 MHz) to see whether other emissions were present. The results are shown in Fig. 5. Unlike the chosen frequency of 4.1 GHz, at 4 G Hz broadband bursts were detected, which could eventually introduce errors in the measurement. It can be seen that movement cannot be visually detected from the waterfall plot, a further analysis is needed.

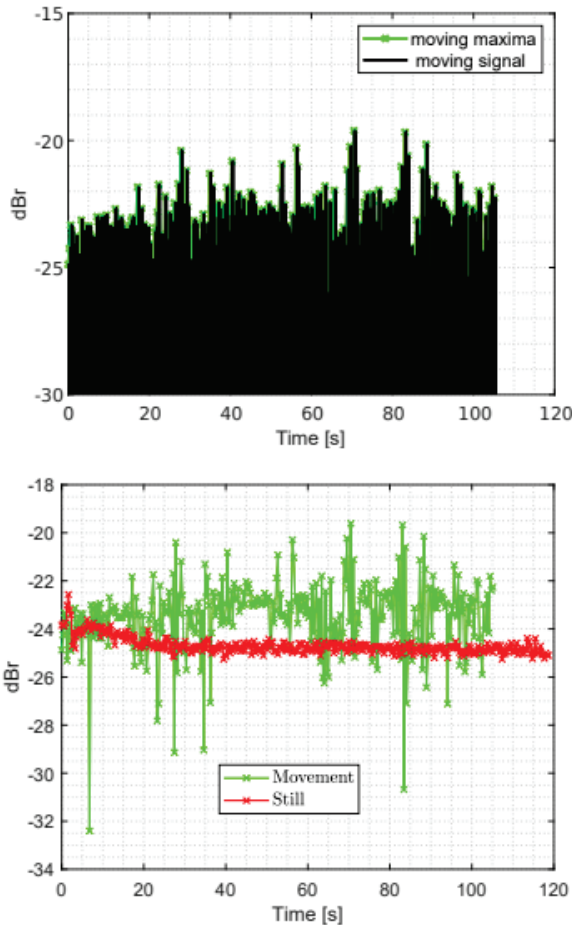

Fig. 4. Indoor test. (Top) maxima and the raw signal for a moving target scenario; (bottom) comparison of both maxima vectors.

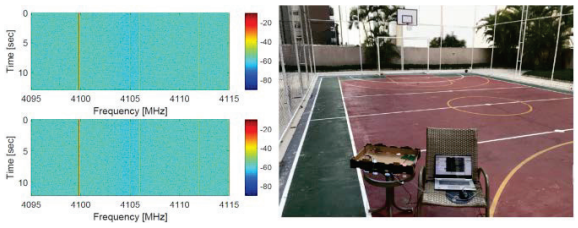

Fig. 5. Outdoor range test site (right) and 12 secs waterfall depiction of spectrum monitoring for the moving (top left) and still (bottom left) cases.

Four measurements were performed, distances of 3, 6, and 9 m, compared with the reference (still) - results are shown in Fig. 6 - each containing approximately 120 seconds. It can be seen that even at 9 m, detection is still possible, visualized on the histogram by its larger variation around the average value. Statistics regarding the four time series are presented in Table1. Higher amplitude average power at 9 m than at 6 m can be ascribed

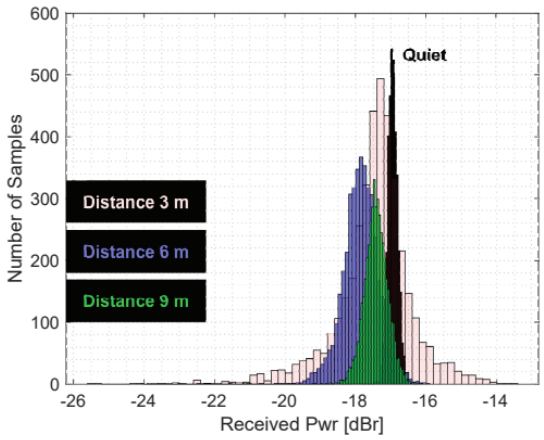

Fig. 6. Histogram for the four different scenarios.

Table 1: Statistics for the different scenarios

Scenario	Average [dBr]	Std. Dev. [dBr]
Still	−16.9	0.2
3 m	− 17.5	1.1
6 m	−17.9	0.5
9 m	−17.4	0.4

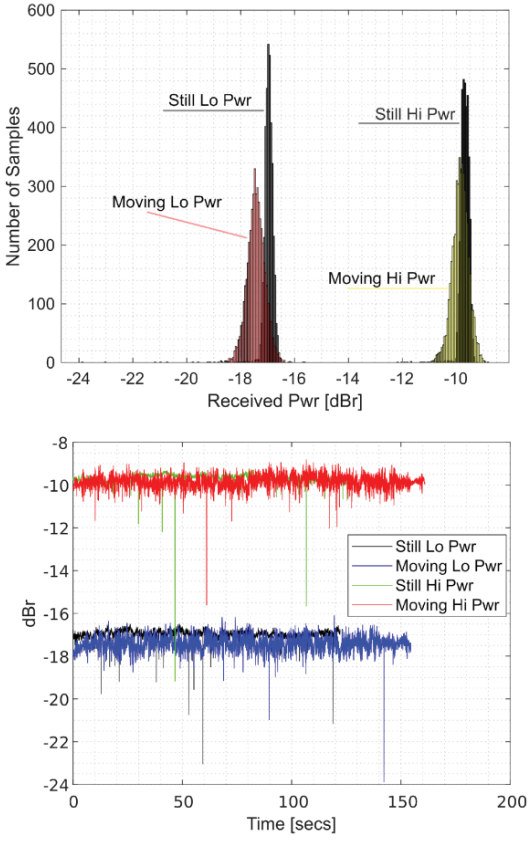

Fig. 7. *Continued.*

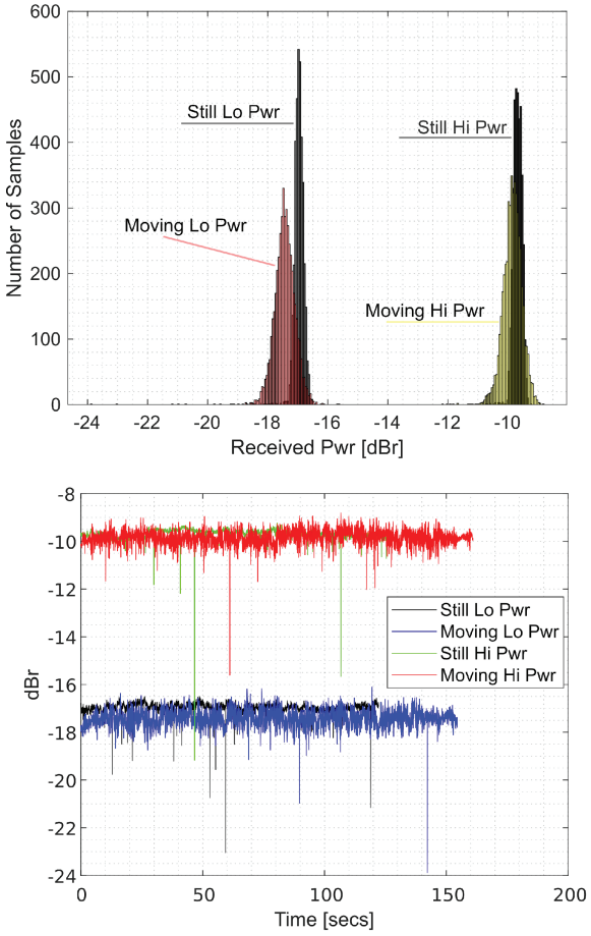

Fig. 7. Time series of the maxima at 9 m, output powers of 5 dBm ("Hi Pwr") and −4 dBm ("Lo Pwr"), bottom, and respective histogram, top.

to reflected energy by the ground, contributing in a constructive way to the receiving antenna.

A comparison was performed with the maximum and minimum synthesizer output powers (5 and −4 dBm), for the 9 m distance case. Results showing the maxima time series and the respective histogram are shown in Fig. 7. It can be seen that in spite of the lower output power the variance of the signal is larger, resulting in a higher sensitivity. Average and standard deviations are summarized in Table 2.

Table 2: Comparison of different output levels, 9 m distance

Scenario	Average [dBr]	Std. Dev. [dBr]
Still −4 dBm	−16.9	0.2
Still 5 dBm	− 9.7	0.2
9 m, −4 dBm	−17.14	0.4
9 m, 5 dBm	−9.8	0.3

V. CONCLUSION

A low-cost radar applied to human detection, based on a software-defined radio, is presented. In addition to the SDR, other off-the-shelf RF components are two broadband planar antennas and an RF synthesizer. The detection is based on amplitude variations picked up by the receiver, compared to the baseline case where there is no movement (still). The present solution adapts to hardware restraints of the HackRF One SDR, which has only one RF input, therefore unable to provide Doppler or passive approaches unless extra hardware is added. The system was tested in real-world environments, both indoor and outdoor, whose sensitivity was evaluated against different statistics regarding human presence and still patterns. Further classification based on the specific deployed environment should operate using, for instance, machine learning, to compare existing time series and decide upon the presence or not of human activity. As a contribution, this article presents an alternative to other human activity detection, with advantages coming from the software-defined hardware, where different frequencies and power levels can be modified on-the-fly. It does not employ sophisticated RF elements such as circulators and external mixers. GNU Radio functionalities enable further useful possibilities, such as remote monitoring, using TCP/IP channels connecting both client and server, and also Python integration.

REFERENCES

[1] J. A. Nanzer "A review of microwave wireless techniques for human presence detection and classification," *IEEE Trans. Microw. Theory Techn.*, vol. 65, pp. 1780-1794, 2017.

[2] G. Wang, C. Gu, T. Inoue, and C. Li, "A hybrid FMCW-interferometry radar for indoor precise positioning and versatile Life activity monitoring," *IEEE Trans. Microw. Theory Techn.*, vol. 62, pp. 2812-2822, 2014.

[3] S. Yoo, S. Ahmed, S. Kang, D. Hwang, J. Lee, J. Son, and S. H. Cho, "Radar recorded child vital sign public dataset and deep learning-based age group classification framework for vehicular application," *Sensors*, vol. 21 pp. 1-16, 2021.

[4] S. Lee, S. Y. Kwon, B. J. Kim, H. S. Lim, and J. E. Lee, "Dual-mode radar sensor for indoor environment mapping," *Sensors*, vol. 21, no. 2469, 2021.

[5] Y. Wang, W. Wang, M. Zhou, A. Ren, and Z. Tian, "Remote monitoring of human vital signs based on 77-GHz mm-wave FMCW radar," *Sensors*, vol. 20, no. 2999, 2020.

[6] E. Turppa, J. M. Kortelainen, O. Antropov, and K. T. Vital, "Sign monitoring using FMCW radar in various sleeping scenarios," *Sensors*, vol. 20, no. 6505, 2020.

[7] F. Sekak, K. Zerhouni, F. Elbahhar, M. Haddad, C. Loyez, and K. Haddadi, "Cyclostationary-based vital signs detection using microwave radar at 2.5 GHz.," *Sensors*, vol. 20, no. 3396, 2020.

[8] H. Zhao, H. Hong, L. Sun, Y. Li, C. Li, and X. Zhu, "Noncontact physiological dynamics detection using low-power Digital-IF Doppler radar," *IEEE Trans. Instrum. Meas*, vol. 66, no. 1780-1788, 2017.

[9] R. Ashikur, I. Yuta, and L. Victor, "UAV radar system for vital sign monitoring," *Applied Computational Electromagnetics Society (ACES) Journal*, 208-211, 2018.

[10] D. Yang, Z. Zhu, J. Zhang, and B. Liang, "The overview of human localization and vital sign signal measurement using handheld IR-UWB through-wall radar," *Sensors*, vol. 21, no. 402, 2021.

[11] D. Wang, S. Yoo, and S. H. Cho, "Experimental comparison of IR-UWB radar and FMCW radar for vital signs," *Sensors*, vol. 20, no. 6695, 2020.

[12] L. Amaduzzi and M. Tinti, "Low-cost components radiometer implementation for human microwave electromagnetic field emissions detection," *PIERS Letters*, vol. 23, no. 9-18, 2011.

[13] B. Tan, K. Woodbrigde, and K. Chetty, "A real-time high resolution passive wifi Doppler-radar and its applications," in *Proc. 2014 International Radar Conf.*, pp. 13-17, 2014.

[14] A. C. Green, D. Coggon, R. de Séze, P. A. Gowland, C. Marino, A. P. Peralta, P. G. Söderberg, R. Stam, M. C. Ziskin, E. van Rongen, M. Feychting, M. Asmuss, R. Croft, G. D'Inzeo, A. Hirata, S. Miller, G. Oftedal, T. Okuno, M. Röösli, Z. Sienkiewicz, and S. Watanabe, "Icnirp statement on diagnostic devices using non-ionizing radiation: Existing regulations and potential health risks," *Health Phys.*, vol. 112, no. 305-321, 2017.

[15] Gnu Radio Project. Gnu radio. URL https://www.gnuradio.org.

[16] National Instruments. Labview. URL https://www.ni.com/pt-br/shop/labview.html.

[17] Mathworks. Matlab. URL https://www.mathworks.com.

[18] Octave Forge. Octave. URL https://octave.sourceforge.io/.

Marcelo B. Perotoni Electrical Engineer (UFRGS, Porto Alegre, Brazil) received an Ms.C. and Ph.D. in Electrical Engineering from USP(Sao Paulo, Brazil). He is currently a professor at UFABC.

Kenedy M. G. Santos has a B.Sc. in Electrical Engineering (PUC MG), an M.Sc. in Electrical Engineering UFMG, and a PhD. in Electrical Engineering UFBA. Currently, he is a professor at IFBA. He has experience in EMC

Danilo B. Almeida has a B.Sc. in Electrical Engineering (2005) – UNIP – SP. He is a specialist in occupational safety and energy efficiency. Currently, he is a professor at the IFBA.

Daniel Jonathas Electrical Engineering Student from IFBA. IEEE member and the Vice President of the IEEE MTT-S IFBA VDC Chapter.